# Investigations on the decay length method for the measurement of the top quark mass at the ATLAS experiment

Dissertation
zur Erlangung des akademischen Grades
eines Doktors der Naturwissenschaften
(Dr. rer. nat.)
der Fakultät Physik
der Technischen Universität Dortmund

vorgelegt von
Dipl. Phys. Jörg Walbersloh

Lehrstuhl für Experimentelle Physik IV
Fakultät Physik
TU Dortmund

eingereicht am 21. August 2009

Erstgutachter:
Priv. Doz. Dr. Reiner Klingenberg, Technische Universität Dortmund
Zweitgutachter:
Prof. Dr. Bernhard Spaan, Technische Universität Dortmund

Datum der mündlichen Prüfung:
25. September 2009

**Abstract**

The precision of the determination of the top quark mass at particle collider experiments with methods which rely on jet energy measurements is limited due to the jet energy scale. This thesis presents a method that relies almost exclusively on tracking and thus has complementary uncertainties with respect to other methods. This so-called decay length method correlates the mean transverse decay length of $B$-Hadrons originating from top quark decays to the mass of the initial top quark. The thesis discusses the application the method for the semileptonic decay channel of $t\bar{t}$-Events at the ATLAS detector and presents an estimate for uncertainties based on MonteCarlo simulations.

# Contents

# Chapter 1

# Introduction

Investigations on fundamental constituents of matter have been an interest of mankind since ancient times. The concept of elementary and indivisible basic particles has always been the guiding idea in the search of these constituents. Today it is believed that these particles can be summarized in three groups, which are the quarks and leptons that are the building blocks of the visible matter, and the bosons which are the carriers of interactions between the particles. The up to date theory to describe both particles and their interactions is the so-called standard model of particle physics.

Among the basic particles in the standard model the top quark is the youngest with respect to its first observation. Since the discovery of the top quark in 1995 many efforts have been made to investigate its properties. The top quark provides the possibility to study the deeper insides of the standard model and at the same time stands as a cornerstone to new physics which may be beyond the standard model. Being the heaviest of the known fundamental particles, the large mass of the top quark is an important parameter in standard model calculations. A high precision knowledge of the top quark mass will allow to test the descriptions of electroweak processes and thereby implies on the mass of a possible Higgs boson, which is the yet undiscovered last particle of the standard model. Therefore, the focus of top quark studies in the past years was to determine its mass as precisely as possible.

The current world average of the top quark mass $m_t = (173.1 \pm 1.3)$ GeV has been obtained from a few thousand top quark pairs which were produced at the Tevatron $p\bar{p}$-collider where the top quark was also discovered. The upcoming $pp$-collider LHC will be a next-generation particle physics facility where approximatelly eight million top quark pairs will be produced per year. The LHC is therefore regarded as a top quark factory and provides the possibility to increase the precision on $m_t$ by far.

The ATLAS experiment is one of the two multipurpose experiments at the LHC that will investigate top quarks and measure their mass. As statistical uncertainties will be negligible at the LHC, the main goal in the preparation of the experiment was to estimate possible systematic uncertainties on $m_t$ using Monte-Carlo simulations. One of the major influences in the determination of $m_t$ is the measurement of the hadronic jet energy as jets play an important role in nearly all techniques that are used to measure the top quark mass.

This thesis presents an alternative method that has complementary systematic uncertainties with respect to other methods since it relies almost exclusively on tracking. This so-called decay length method measures the mean transverse decay length of $B$-hadrons from top quark decays which is highly correlated to the mass of the parent top quark. The decay length is obtained from the distance of primary and secondary vertices in the collision event, making this method independent of energy measurements of jets.

The aim of this thesis is to demonstrate the general applicability of the decay length method to ATLAS. An estimate on the expected mean transverse decay length is therefore presented for several generated top quark masses. This so-called mass estimator is the basis for the determination of a functional relationship of the mean transverse decay length and the top quark mass itself. This mass estimator is investigated regarding its stability with respect to changes in the event selection, the influence of non-$t\bar{t}$ background as well as method inherent effects. Furthermore, systematic uncertainties of this method will be estimated and possible options for further studies are proposed.

In detail the thesis is organized as follows: Chapter 2 introduces the ATLAS experiment and describes technical details of the detector components. A general subsumption of the experiments role regarding current particle physics issues is also presented. Additionally, the conventions on names and representations of detector variables and observables used in this thesis are introduced here. Chapter 3 gives a bief summary of the concepts of particle physics and provides an introductory overview of top quark physics. A special emphasis is placed on the mass of the top quark and its role in particle physics. An overview of techniques to measure the top quark mass is also presented here. Chapter 4 shortly describes the context of this study and introduces the MonteCarlo data, analysis framework and physics object selection that is used in this thesis. A side note will also be made on the development of analysis tools done in the course of this study. Some of these tools were integrated in the official analysis framework; a technical discussion on their functionality is therefore presented in the appendix to this thesis. Chapter 5 then presents the results on the decay length method and discusses systematic effects and uncertainties as well as possible improvements to the method. Chapter 6 summarizes this thesis and gives an outlook on the further prospects of the decay length method.

# Chapter 2

# The ATLAS experiment

The ATLAS[1] experiment is a multipurpose particle physics experiment which is currently being set up at the European Center for Nuclear Research CERN[2]. It is one of four major experiments in the course of the **L**arge **H**adron **C**ollider LHC. The LHC will provide high energy proton-proton collisions that will be investigated by the experiments. The two major aspects of the ATLAS experiment itself are the ATLAS detector, which does the actual measurement of the remnants of the *pp*-collisions, and the ATHENA analysis package, which is used to analyze these measurements.

This chapter provides a description of the experiment focussing on the detector and its connection to the LHC project. Also, the experiments context concerning current physics issues and the possibility of discoveries is discussed.

## 2.1 CERN and the LHC

The European Center for Nuclear Research CERN is located in Geneva, Switzerland, at the border to France in the region of Rhône-Alpes. It was founded in 1954 not even ten years after the second world war. At that time, it was intended as an upcoming state-of-the-art physics laboratory to establish a new european physics community. More than fifty years later, CERN has become one of the leading scientific research facilities in the field of particle physics. Over the years, CERN developed particle accelerators for ever increasing energies as well as detectors that were able to handle the technical and scientific requirements that came with the accelerators. Some of the highlights worth mentioning are the Super Proton Synchrotron (SPS) installed in 1979 where the $W^{\pm}$ and $Z^0$ bosons were discovered in 1983 or the **L**arge **E**lectron **P**ositron Collider (LEP) where high precision measurements on these particles were performed.

Right now, the next generation *pp*-collider LHC is being installed. The LHC will push the energy scale of particle physics into a new order of magnitude. The collider ring utilizes the infrastructure of the meanwhile decommissioned LEP; it is located in the same tunnel. Only a few new caverns, like the one for the ATLAS detector, had to be excavated. An overview of the LHC with its experiments and service facilities is given in Figure 2.1.

[1] **A** **T**oroidal **L**HC **A**pparatu**S**
[2] **C**onseil **E**uropéen pour la **R**echerche **N**ucléaire

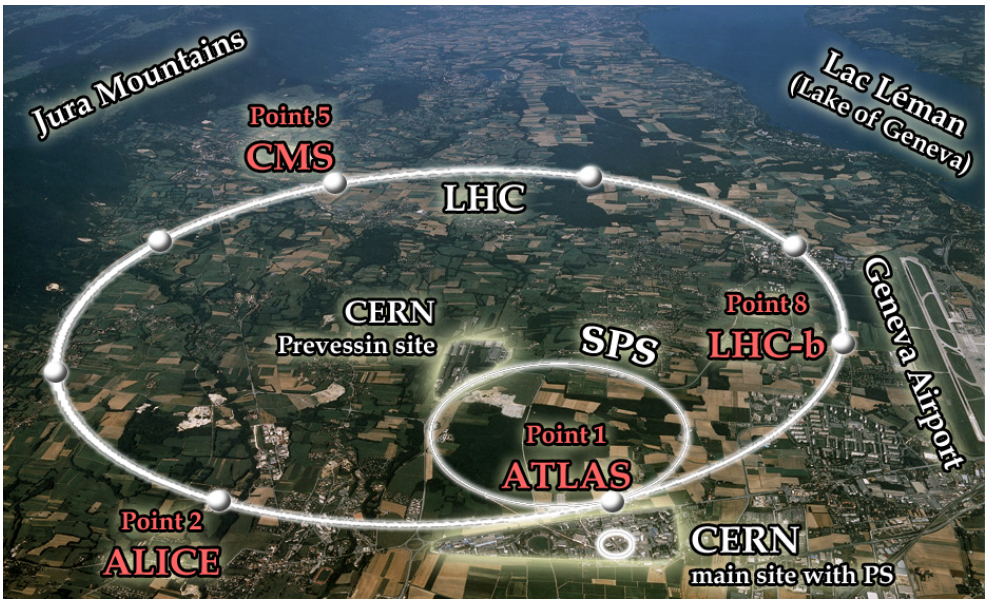


**Figure 2.1:** Arial view of the CERN and LHC region near Geneva. The locations of the tunnels, the CERN sites and experiments are marked.

When reaching its nominal operation mode, the LHC will collide protons with a center of mass energy of $\sqrt{s} = 14$ TeV with a luminosity of $10^{34}$ cm$^{-2}$s$^{-1}$ and an interaction rate of $\approx 40$ MHz. The protons will be organized in bunches containing up to $10^{11}$ protons each. To be able to bend the protons on their way in the collider, special superconducting dipole magnets with a stronger field than at LEP are required, since the proton is two thousand times heavier than electrons and positrons.

In an initial so-called "low-lumi" phase the LHC will provide a factor of ten less luminosity of $10^{33}$ cm$^{-2}$s$^{-1}$. Assuming an ideal accelerator running continuously for ten days this is equivalent to an integrated luminosity of 1 fb$^{-1}$, which is a reference value that will be used throughout this thesis.

The four major experiments can be subdivided into the two big multipurpose experiments ATLAS and CMS[3] and the two experiments LHC-B and ALICE[4] that focus on special physics. ATLAS itself is located at Entry Point 1 at approximately 100 meters depth directly below the main CERN facility ground, while CMS lies at the opposite side of the ring. Both experiments focus on general particle physics, but especially the discovery of new particles and phenomena. The LHC-B experiment is located at Point 8 near the ATLAS detector. It is designed to investigate $B$-mesons, hence the experiments name. Apart from precision measurements in the $B$-sector, the main physics goal here is to investigate CP-violation and the matter-antimatter asymmetry of the universe. Also located near ATLAS is the ALICE detector at Point 2. ALICE is optimized for the study of heavy ion collisions to investigate quark gluon plasma. For this purpose, the LHC will provide lead ion collisions with a center of mass energy of 5.5 TeV per nucleon pair.

[3] **C**entral **M**uon **S**olenoid
[4] **A** **L**arge **I**on **C**ollider **E**xperiment

## 2.2 The ATLAS Detector

The detector of the ATLAS experiment is a typical multipurpose collider detector. The interaction point is located in the center of the detector, surrounded by various layers of different subdetectors. The three basic components are a tracking system as the innermost part near the interaction point, a system of calorimeters for energy measurements of electromagnetic and hadronic particle showers and a muon spectrometer. The overall dimensions of the fully assembled detector are 25 meters in diameter and 44 meters in length, while its total mass is approximately 7000 tons. Figure 2.2 shows an exploded view of the full ATLAS layout.

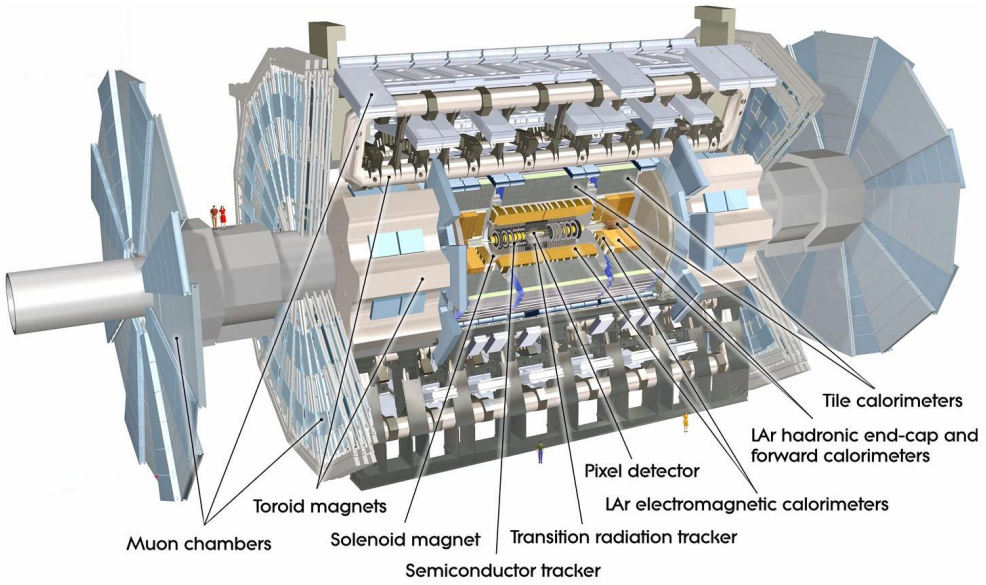


**Figure 2.2:** Overall layout of the ATLAS detector. The different subdetectors as well as the magnet systems are labeled [1].

### 2.2.1 Coordinate system and naming convention of ATLAS

To define the geometry, location and orientation of the ATLAS detector and any point within it a special coordinate system is used. It shall be briefly described here since these coordinates are widely used in this thesis. The general geometry and absolute location is described by a right-handed cartesian system whose point of origin ($x$=$y$=$z$=0) is located at the center of the detector. The orientation of the system is chosen such that the $x$-direction points to the center of the LHC ring and the $y$-direction points upwards to the surface. As a consequence, the $z$-axis goes parallel to the beam axis and its positive direction points to Point 8 where LHC-B is located. Any transverse object, like transverse momenta $p_\perp$ or missing transverse energy $\not{E}_\perp$, is therefore defined in the $x$-$y$-plane. Since the remnants of the proton-proton collisions will be distributed isotropically, a spherical system can be used as well. In this system, the object's azimuth angle in the $x$-$y$-plane is called $\varphi$ and its polar angle with respect to the beam axis is called $\theta$.

Using these definitions, any vectorial quantity like the momentum $\vec{p}$ can be separated into its transverse component

$$p_\perp = p_{xy} = |\vec{p}_x + \vec{p}_y| = |\vec{p}| \sin(\theta) \tag{2.1}$$

and its longitudinal component

$$p_L = |\vec{p}_z| = |\vec{p}| \cos(\theta)\,. \tag{2.2}$$

Both notations, cartesian as well as spherical, will be used throughout this thesis. The particular description often is chosen for technical reasons and will be explained in the respective case. A detailed list of basic detector observables and their representation in the ATLAS coordinate system is provided by Table 2.1.

**Table 2.1:** Definition of observables and detector parameters as used throughout this thesis.

| observable | notation | representation |
|---|---|---|
| space point | $\vec{r}$ | $= (x, y, z)$ |
| spatial distance/length | $L_{xyz}$ | $= \sqrt{\Delta x^2 + \Delta y^2 + \Delta z^2}$ |
| energy | $E$ | |
| four momentum | $\mathbf{p}$ | $= (E, \vec{p}) = (E, p_x, p_y, p_z)$ |
| transverse momentum | $p_\perp$ | $= \sqrt{p_x^2 + p_y^2}$ |
| mass | $m$ | $= \sqrt{E^2 - \vec{p}^2}$ |
| missing transverse energy | $\not{E}_\perp$ | |
| polar angle | $\theta$ | $= \operatorname{arccot}\left(\frac{p_z}{p_\perp}\right)$ |
| azimuth angle | $\varphi$ | $= \arctan\left(\frac{p_x}{p_y}\right)$ |
| rapidity | $Y$ | $= \frac{1}{2} \ln\left(\frac{E+p_z}{E-p_z}\right)$ |
| pseudorapidity | $\eta$ | $= \frac{1}{2} \ln\left(\frac{\lvert\vec{p}\rvert+p_z}{\lvert\vec{p}\rvert-p_z}\right) = \frac{1}{2} \ln\left(\frac{\theta}{2}\right)$ |
| distance in the $\eta$-$\varphi$-plane | $\Delta R$ | $= \sqrt{\Delta\eta^2 + \Delta\varphi^2}$ |

### 2.2.2 Physics goals and detector requirements of the ATLAS experiment

ATLAS is a dedicated discovery experiment. The physics program is led by the question whether the Higgs mechanism which generates mass on the fermions is realized in nature; therefore, the discovery of either a standard model Higgs boson $H$ or a family of MSSM[5] Higgs particles $H^0, A, H^\pm$ is expected.

[5] **M**inimal **S**upersymmetric extension of the **S**tandard **M**odel

ATLAS will also address many questions in particle physics that are usually referred to as "**b**eyond **s**tandard **m**odel" (BSM). These questions include the search for supersymmetric particles as well as e.g. heavy gauge bosons $W'$ and $Z'$ or extra dimensions.

Standard model physics will also be investigated. Especially the systems of the heaviest quarks ($b$, $t$) are of great interest since they have large production cross sections at the LHC. The $B$-sector offers the possibility to measure CP-violation, for example in the decay $B_0^d \to J/\psi K_s^0$ as well as $B\bar{B}$ mixing, while in the top-sector one can perform precision measurements and study top quark signals as background to Higgs searches. As this thesis deals with top quark physics, a more detailed discussion on the top quark and its importance in modern particle physics will be displayed in chapter 3.

### Physics requirements of the ATLAS detector

The experimental signatures of the previously described physics investigations define the benchmark for the performance of ATLAS and its subdetectors. To demonstrate the performance requirements, the search for the Higgs boson shall be taken as an example here [2, 3].

Since the mass of a possible Higgs boson can not be predicted from a priori assumptions, one has to consider a large range of masses and therefore a complex multiplicity of decay signatures.

At low Higgs masses $m_H < 2m_Z$ the predominant channel $H \to q\bar{q}$ is difficult to discriminate from low energy QCD background; promising signatures therefore include $H \to \gamma\gamma$ or the associated production $t\bar{t}H, WH$ and $ZH$ where the lepton of the decay of one of the top quarks or the vector bosons can be used for triggering and background rejection. In addition to the above signatures, the channel $H \to b\bar{b}$ benefits from the usage of $b$-tagging.

At high Higgs masses $m_H > 2m_Z$, the decay into pairs of $Z$-bosons which further decay into oppositely charged leptons $H \to ZZ \to 4\ell^{\pm}$ is a very clean signal. The analog channel via $W$-bosons $H \to WW \to 2\ell + 2\nu_\ell$ provides similar sensitivity due to the two leptons and the high missing energy of the neutrinos.

In the search for possible MSSM Higgs particles similar signatures are expected. In addition, one needs sensitivity to processes involving $\tau$'s like $A \to \tau^+\tau^-$ and $H^{\pm} \to \tau^{\pm}\nu$, where the $\tau$'s themselves may decay further as well into leptons as into hadrons.

This variety of possible signatures already demonstrates the crucial requirements for the ATLAS detector:

- high-resolution tracking in a high track-density environment to fulfill requirements of primary and secondary vertex distinction, $b$-tagging and momentum resolution,
- good electromagnetic calorimetry for electron and photon identification,
- good hadronic calorimetry for measurement of energy from hadronic jets as well as for determination of missing energy,
- high precision muon spectrometry,
- hermetic coverage in all subsystems, i.e. large acceptance in $\eta$ and (almost) full coverage in $\varphi$.

A detailed list of the desired performance of ATLAS in terms of resolution and coverage is provided by Table 2.2.

**Table 2.2:** Performance goals of the ATLAS detector. Note that the muon spectrometer performance is independent from the tracking system for high-$p_\perp$ muons [3].

| detector component | resolution | $\eta$-coverage | |
|---|---|---|---|
| | | measurement | trigger |
| tracking | $\frac{\sigma_{p\perp}}{p_\perp} = 0.05\%\ p_\perp \oplus 1\%$ | $\pm$ 2.5 | n/a |
| em. calorimeter | $\frac{\sigma_E}{E} = 10\%\ \sqrt{E/\mathrm{GeV}} \oplus 0.7\%$ | $\pm$ 3.2 | $\pm$ 2.5 |
| had. calorimeter | | | |
| - barrel/endcap | $\frac{\sigma_E}{E} = 50\%\ \sqrt{E/\mathrm{GeV}} \oplus 3\%$ | $\pm$ 3.2 | $\pm$ 3.2 |
| - forward | $\frac{\sigma_E}{E} = 100\%\ \sqrt{E/\mathrm{GeV}} \oplus 10\%$ | $\lvert\eta\rvert < 4.9$<br>$\lvert\eta\rvert > 3.1$ | $\lvert\eta\rvert < 4.9$<br>$\lvert\eta\rvert > 3.1$ |
| muon spectrometer | $\sigma_{p\perp}/p_\perp = 10.05\%$ at $p_\perp = 10$ TeV | $\pm$ 2.7 | $\pm$ 2.4 |

**Technical requirements of the ATLAS detector**

Apart from requirements resulting from the desired physics performance, ATLAS faces also technical challenges arising from the nature of LHC's proton-proton collisions. The high interaction rate and luminosity combined with the large multiplicity of daughter particles from *pp*-collisions result in high particle fluxes in the detector systems. This requires radiation hard and fast electronics and sensor elements. Additionally, a high detector granularity is required to be able to resolve high particle flux densities and reduce the influence of overlapping events. To keep the incoming amount of data from the detector systems manageable, a fast and efficient trigger is required. Furthermore, all detector components require thermal and mechanical stability to ensure constant measurement conditions. Simultaneously, it is required to use low mass detector parts to minimize multiple scattering effects.

### 2.2.3 The inner detector

The tracking system of the ATLAS detector is centered around the interaction point and is referred to as the **I**nner **D**etector (ID) [3,4]. It provides high resolution tracking which allows vertex identification as well as momentum measurement of the traversing particles. Since the track density is highest in the region near the interaction point, the inner detector is divided into three subdetectors which combine good track separation in the center region with continous tracking in the outer region. The inner detector is supplied with a 2 Tesla magnetic field by the so called Central Solenoid (CS), which surrounds the ID and separates it from the calorimeters.

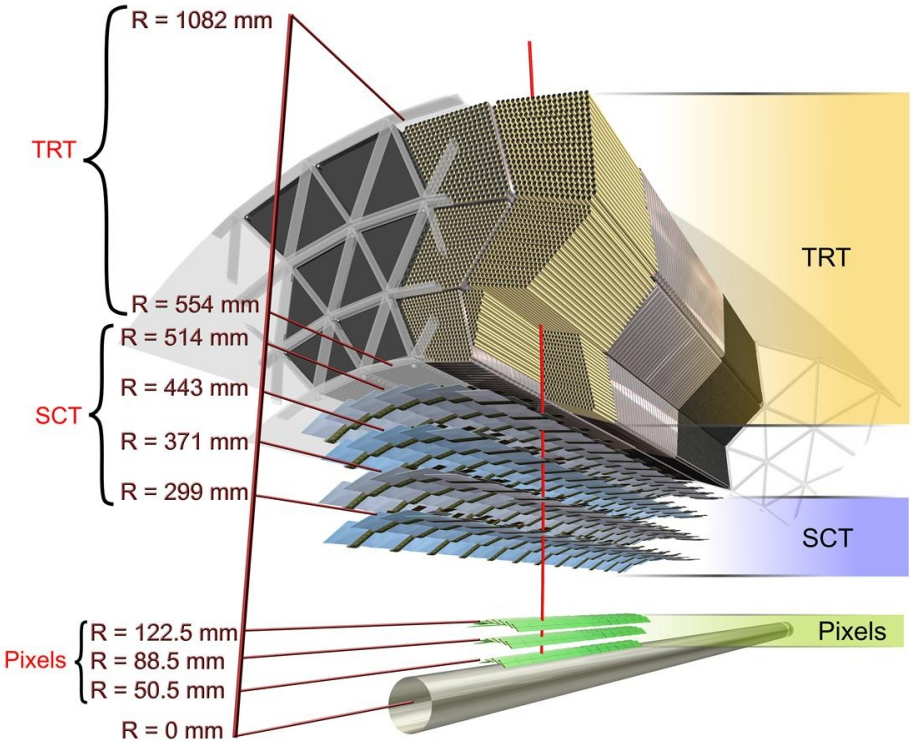


**Figure 2.3:** Segmental view of the inner detector barrel, showing the dimensions of the three individual subdetectors around the beryllium beam pipe [3].

The three subdetectors are arranged in layers around the center of the ATLAS detector as seen in Figure 2.3. The innermost subdetector is the pixel detector, which is installed directly in the center of ATLAS around the interaction point. With approximately 80.4 million readout channels in a volume of 1.4 m length and 17 cm radius it provides the highest granularity of all detectors in the ID.

1744 segmented semiconductor detector moduls of 19 mm $\times$ 63 mm size are arranged in three layers and on three end cap discs on each side. Each module has 46080 pixels which have a minimum size in ($R$-$\varphi$) $\times$ $z$ of 50 $\times$ 400 $\mu$m$^2$. This innermost layer holding 286 modules is mounted directly on the beam pipe which has a nominal radius of 29 mm $< r <$ 34.3 mm. This proximity makes the layer extremely important with respect to $b$-tagging and vertex finding, as it provides a precision measurement of track points very close to the interaction point; it is therefore referred to as the B-Layer. It is followed by Layer 1 (L1) and Layer 2 (L2) in the higher radial distances, providing up to three measured space points in total. The intrinsic accuracies are estimated to be 10 $\mu$m in ($R$-$\varphi$) and 115 $\mu$m in the $z$-direction.

To minimize multiple scattering of the traversing particles, the mechanical support structure is mostly made of carbon, which has a low mass and at the same time guarantees a good mechanical and thermal stability.

The radii of the active sensor elements are shown in Figure 2.3, and a cut-away view of the pixel detector illustrating the discs, barrel layers and modules is shown in Figure 2.4.

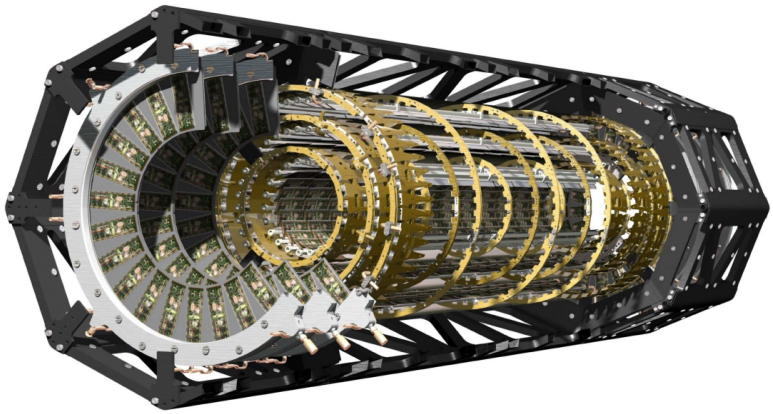

**Figure 2.4:** Cut-away view of the ATLAS pixel detector with the layers, discs support structure and individual modules visible [3].

The second subdetector of the ID is the silicon microchip tracker (SCT[6]) [3,5]. Like the pixel detector it consists of semiconductor sensor modules but has less granularity with only 6.3 million readout channels. An SCT module consists of four single sided sensors with a size of $64 \times 64$ mm$^2$. Two of these sensors are daisy-chained to form a 128 mm long strip that is glued back-to-back with the respective other strip. To enable the measurement of the $z$-coordinate of the traversing particle the two strips are rotated to each other by an angle of 40 mrad ($\approx 2°$). The intrinsic accuracies per module are 17 $\mu$m in ($R$-$\varphi$) and 580 $\mu$m in the $z$-direction. The total amount of 4088 modules is arranged in 4 (double-)layers in the barrel, counted L3 to L6 as continous from the pixel detector, and 9 (double-)layers in each end cap, providing up to 4 (9) space points for the track of a traversing charged particle.

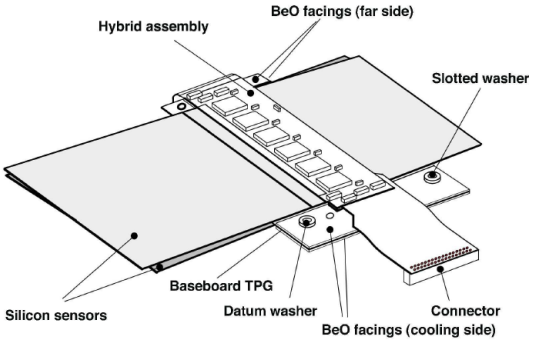


**Figure 2.5:** SCT module [3].

The third subdetector of the ID is the **T**ransition **R**adiation **T**racker (TRT). The TRT is a combination of a transition radiation detector, making it possible to identify electrons, and a drift chamber. The total number of readout channels is approximately 351,000. Similar to the other subdetectors, it consists of one barrel and three end caps on each side. The drift chamber wires run parallel to the beam axis in the barrel region and radial to the beam in the end caps. For better mechanical stability and due to better readout performance the 'straw-tube' technique is used. Each tube is a polyimide pipe with a diameter of 4 mm that contains a gold-plated tungsten wire with a thickness of 30 $\mu$m that is stabilized using carbon fibres. The filling gas is a mixture of Xe (70%), $CO_2$ (27%) and oxygene (3%) and has a total volume of 3 m$^3$. It is optimized to be a good detection gas for transition radiation photons and to guarantee a safe operation mode at the same time.

[6]The acronym SCT originally stands for **s**emi**c**onductor **t**racker.

In the barrel region, the tubes form a uniform axial array with a mean spacing of about 7 mm. The tubes are embedded in a matrix of polypropylene fibres that serve as the transition radiation material. The total array is subdivided into triangular shaped modules that are supported by a kapton casing as can be seen in Figure 2.6 (a). A traversing particle crosses at least 36 of this straw tubes in the barrel region.

The end caps are made of independent wheels of radial straw-tubes, each mounted in eight planes to form a wheel as shown in Figure 2.6 (b). The place between the tubes is filled with polypropylene fibres similar to the barrel. On each side, the outer sets of wheels contain eight wheels, the inner set contains 12 wheels.

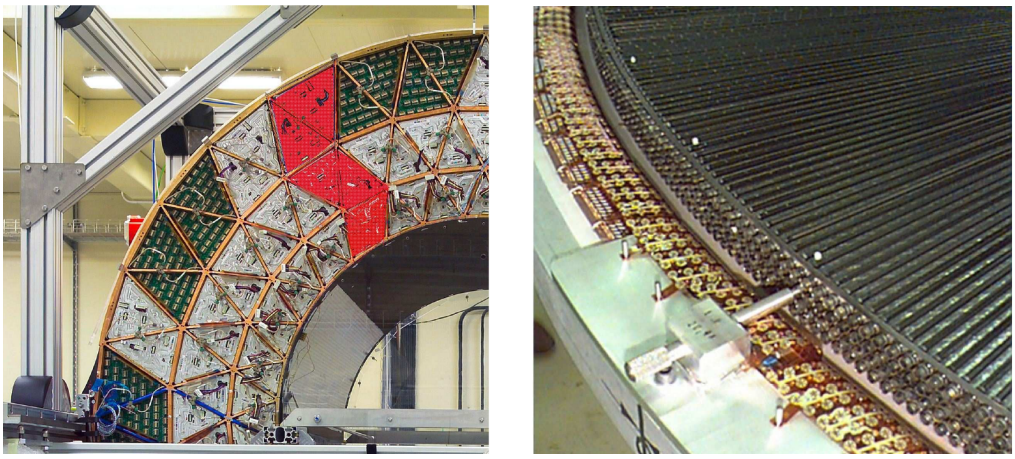

(a) (b)

**Figure 2.6:** Photography of the assembled TRT barrel- (a) and end cap (b) modules. The shapes of one outer, one middle and one inner TRT module are highlighted in red, demonstrating the number of moduls that are passed by a high-$p_\perp$ track [3].

### 2.2.4 Calorimeter

The ATLAS calorimeter system is located between the two magnet systems of ATLAS. On the inside it is bordered by the Central Solenoid which contains the inner detector and on the outside it is surrounded by the toroid magnet that supplies the muon spectrometer. The calorimeter system consists of an electromagnetic calorimeter which identifies and measures electrons and photons and of a hadronic calorimeter that measures the energy of hadrons and particle jets. Both the electromagnetic and hadronic calorimeter are subdivided into a barrel part and end caps, which are separated by so-called crack regions ($1.37 < |\eta| < 1.52$) due to the mechanical support structures. Additionally, special forward calorimeters are embedded at the inside of the electromagnetic end caps. Figure 2.7 shows a cut-away view of the calorimeter system and its subcomponents.

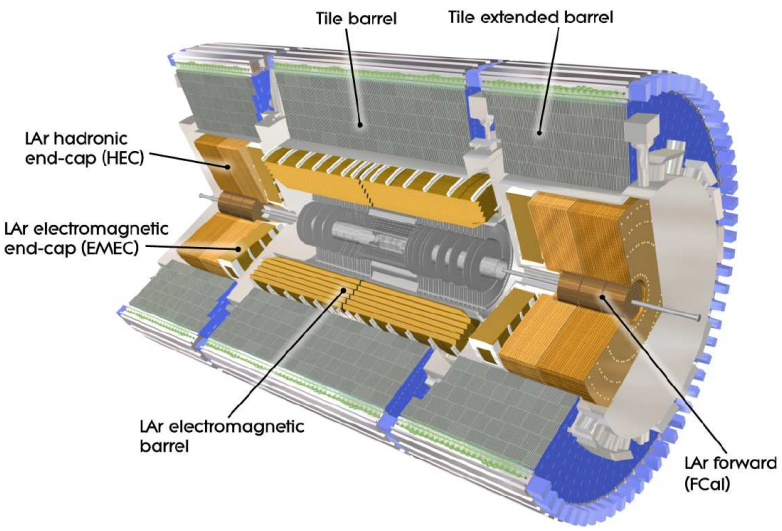


**Figure 2.7:** Cut-away view of the ATLAS calorimeter [3]. The inner detector is adumbrated at the inside. Note the two crack regions that separate the barrel and end cap regions.

### LAr electromagnetic calorimeter

The electromagnetic calorimeter (EMCAL) [3,6] is built using the sampling technique, utilizing liquid Argon (LAr) as the active detector medium and lead plates as the passive absorber material. The readout electrodes are mounted between the lead plates, each consisting of copper plates separated by insulating polyimide sheets. Both the lead- and the copper-plates are built in a accordion geometry, whereby a full azimuthal coverage as well as a uniform performance is realized. Additionally, no projective gaps are present in the calorimeter cells. The LAr-technique is used in all detector parts, i.e. in the central barrel as well as in the end caps. The calorimeter cells are subdivided into three layers with differing granularity and (partly) different geometry. Figure 2.8 shows the detailed arrangement of the cells in the central region ($\eta = 0$) of the detector. The dimensioning of each layer in both $\eta$ and $\varphi$ as well as the radial size are also shown. In addition to the radial dimensions the radiation lengths of the respective structures are quoted. For the purpose of triggering on electrons a smaller granularity is used. The combination of cells to so-called trigger towers and their dimensions are also shown in Figure 2.8.

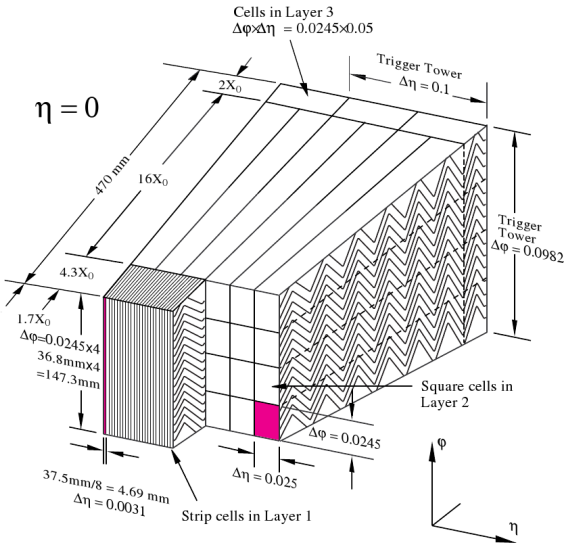


**Figure 2.8:** Cell-geometry of the electromagnetic calorimeter in the central region [3].

### Hadronic calorimeter

The hadronic calorimeter (HCAL) [3, 6] is divided into a central barrel surrounding the EMCAL barrel, two endcaps sitting on top of the electromagnetic end caps and two extended barrels surrounding the end caps of both calorimeters. In contrast to the electromagnetic calorimeter the HCAL uses different techniques in the barrel- and end cap regions. For the end caps a LAr-lead sample calorimeter similar to the electromagnetic end caps is used, with the only difference that a flat geometry is used instead of an accordion shape. The barrel region is built of scintillator modules called tiles. The complete barrel is therefore referred to as the Tile Calorimeter. Each tile is a sample of steel plates which act as the absorber and scintillators which are the active medium. One module as shown in Figure 2.9 spans 5.625 degrees in azimuth, making it possible to arrange 64 modules to one barrel in almost full coverage. The radial length of a module is 2.6 m or 7.4 interaction lengths. The readout is provided by Photomultiplier-tubes (PMT) that are mounted on top of the module near the mechanical support structure. Signals from the scintillators to the PMTs are transported in wavelength-shifting fibres, which are used because they are space-saving as well as they allow to directly transport the signal to the PMTs without the need to guide the signal in a circuitous route. Calibration is done by a laser system to test the response of the photomultipliers and by a $\gamma$-source which can be inserted in specially designed tubes running through the tile to test the cell response [6]. Similar to the electromagnetic calorimeter several adjacent modules are interconnected to low-granularity trigger towers.

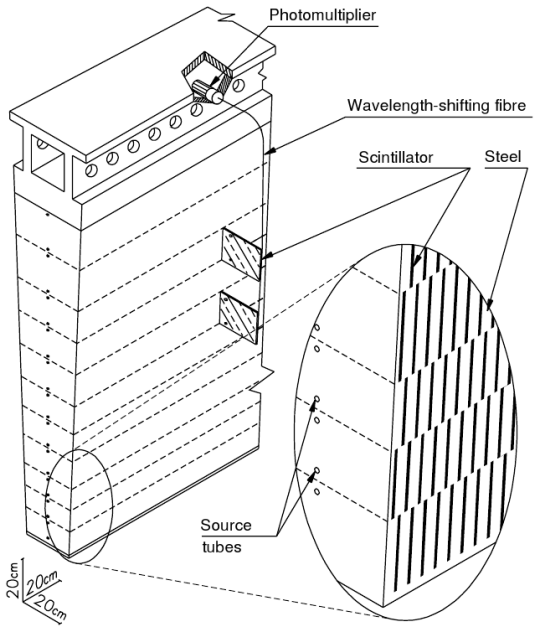


**Figure 2.9:** Schematic view of one ATLAS HCAL tile module [3]. The basic geometry, the readout system as well as the calibration source tubes are shown.

### Forward calorimeter

In the calorimeter region near the beam pipe ($3.1 < |\eta| < 4.9$) a special forward calorimeter (FCAL) [7] is installed. Its design is driven by the requirement of high radiation hardness due to the exposure of high particle fluxes in the forward region. The FCAL is divided in an electromagnetic calorimeter module, two hadronic modules and a copper block which shields the adjacent muon chambers.

Each module is built in the same LAr-sample technique as used in the hadronic end caps. The electromagnetic module has copper plates for absorption while the hadronic end caps use a high amount of tungsten instead to optimize them for high interaction lengths. To achive the required radiation hardness the gaps containing the active LAr are kept as small as possible which also optimizes the heat removal. For details on the mechanical structure refer to [3] as only a small overview shall be given here.

### 2.2.5 The muon spectrometer

Figure 2.10 shows a cut-away view of the muon spectrometer. It is designed to identify traversing muons and measure their momenta as well as to serve as an autonomic trigger.

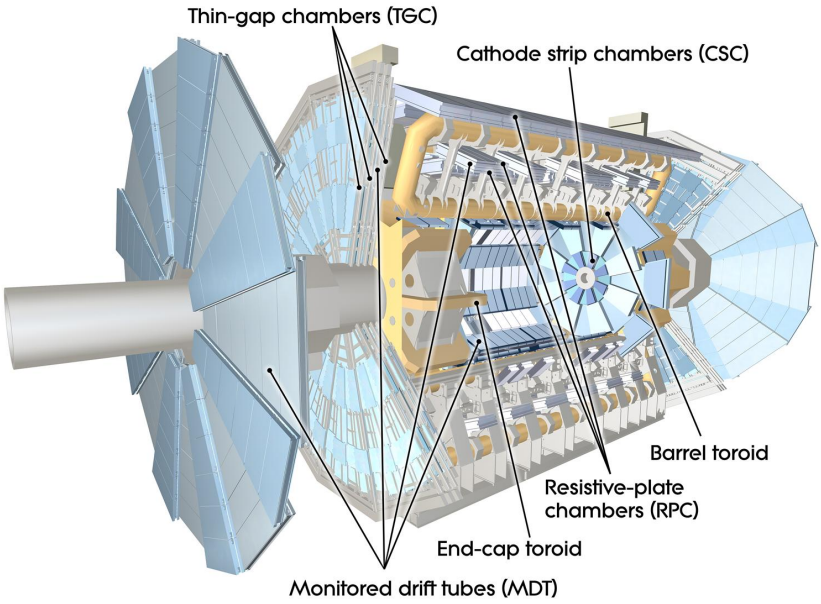


**Figure 2.10:** The muon system of the ATLAS detector [3]. The main components are the deflection magnets (orange) and the detector chambers (blue). For the sake of clarity the types of detector chambers are also labeled.

Different types of detector chambers are used in the muon system, depending on their location and purpose. For the identification and tracking the barrel region uses **M**onitored **D**rift **T**ube chambers (MDT) while the forward region uses **C**athode **S**trip **C**hambers (CSC).

Monitored drift tube chambers consist of layers of three to eight drift tubes. The operating gas is $Ar/CO_2$ pressurized to three bar. The wall of each tube is made of aluminum and the electron collecting wire is made of tungsten-rhenium (W-Re). These chambers combine simplicity in construction and predictable mechanical behavior while providing high measurement accuracy at the same time.

Cathode Strip Chambers are multiwire proportional chambers where the wires are oriented in radial direction and the cathodes are segmented into strips in the orthogonal directions. This allows the measurement of both coordinates from the induced-charge distribution. They are used instead of MDTs since they can cope with the higher counting rates which occur especially in the far forward region.

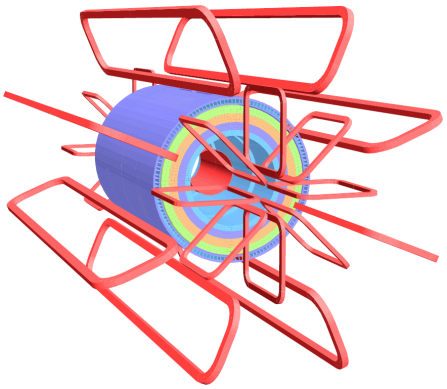

**Figure 2.11:** Arrangement of the ATLAS toroid magnet coils [3].

To be able to measure the muons momenta, a toroidal magnetic field is applied in the region between the calorimeters and the outer boundary of the muon system. The field is realized by an air-core toroid which is the characteristic feature of the ATLAS detector. Since no iron joke is used multiple scattering as well as energy loss from ionisation of the muons is reduced to a minimum. The field intensity of the toroidal magnetic field variies between 0.5 T in the central region and 1 T in the end caps. It is supplied by eight superconducting magnet coils in the barrel region with eight smaller toroids interleaved at the endcaps at each side. The arrangement of the magnet system is shown in detail in Figure 2.11. Here, the toroid coils as well as the inner solenoid are displayed in red, the barrel part of the tile calorimeter is also shown for reference.

The trigger capability of the muon system is provided by **R**esistive **P**late **C**hambers (RPC) in the barrel region and **T**hin **G**ap **C**hambers (TGC) in the end caps. These chamber types were chosen due to their ability to deliver signals with a spread $< 25$ ns, thus beeing able to tag the beam crossing.

A RPC consists of two highly resistive planes mounted parallel to form a gap of about 2 mm which is filled with gas. An electric field of about 4.9 kV/mm is applied between the plates to allow avalanches to form along the ionising tracks towards the anode. The used gas is a complex mixture of tetrafluoroethane ($C_2H_2F_4$), butane ($C_4H_{10}$) and sulfur hexafluoride ($SF_6$). It combines low cost, high safety and it provides the opportunity to use low operation voltage while providing a comfortable plateau for safe avalanche operation. This operation mode offers high rate capability as well as rate-independent time resolution, thus fulfilling the ATLAS trigger requirements as described in section 2.2.2.

The thin gap chambers in the forward regions are multiwire proportional chambers similar to the adjacent CSCs but more customized for their triggering purpose. They use a wire-to-cathode distance of 1.4 mm which is smaller than the wire-to-wire distance of 1.8 mm, thus enabling small drift times. Combined with a high operational voltage of 2.9 kV on the wires, a good time resolution is provided. A signal is expected to arrive within the time window of 25 ns, thus enabling a trigger decision proper to the LHC bunch crossing rate.

## 2.3 The ATLAS trigger system

The **T**rigger and **D**ata **Aq**uistition system (TDAQ) [3, 8, 9] of ATLAS filters the incoming data during the measurement runs to reduce the data flow from an intial 40 MHz bunch crossing rate to a final read out rate of ≈200 Hz. This is necessary to keep the amount of data manageable, since the absolute data rate of about 60 Tb/s is too big to be completely read out and stored for later offline processing. The trigger works in three levels: Level 1 (LVL1), Level 2 (LVL2) and the event filter (EF). Each level applies selection criteria to either reject it or pass the event on to the next level. The following level then refines the decision from the previous one and also applies additional selection criteria, taking benefit of the fact that less data than on the previous level has to be processed. On each level, the information of the muon system, the calorimeters and tracking system are treated in a separate branch. The data flow from these branches and intervention points for each trigger level are shown schematically in Figure 2.12.

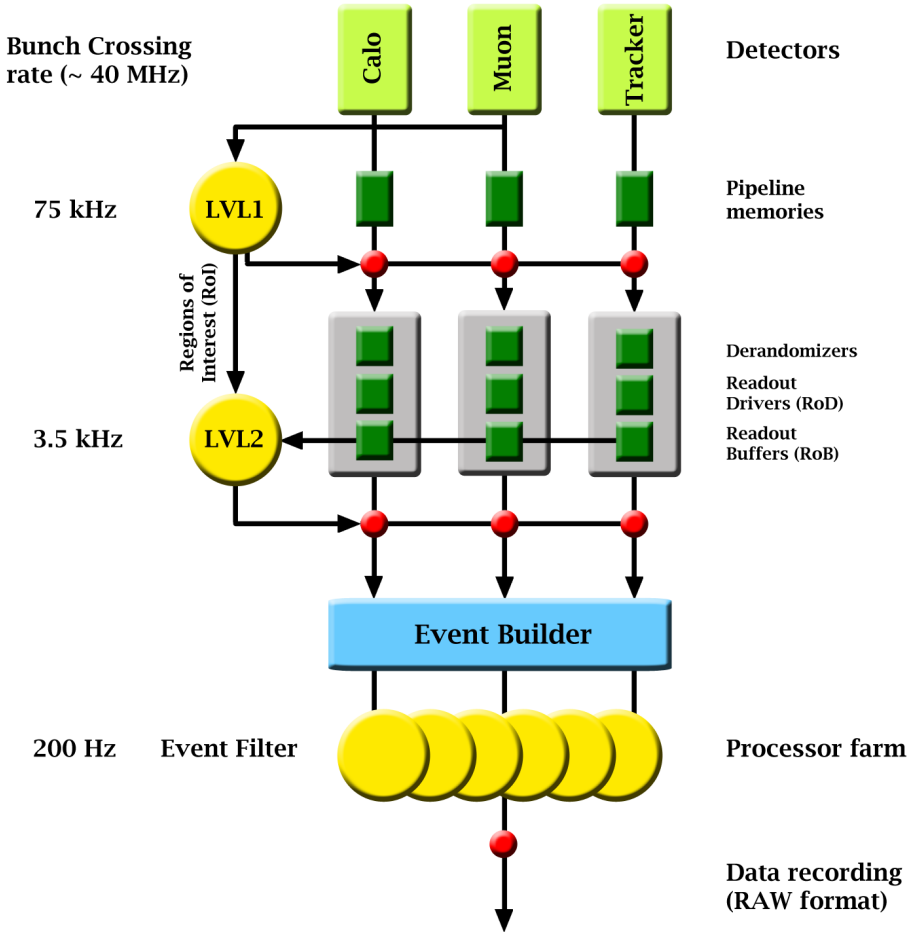


**Figure 2.12:** Schematic representation of the ATLAS trigger. The arrows indicate the data flow along the readout system (central branch) and the input to the trigger systems (left branch). The trigger intervention points are marked in red. The respective reduced output rates of the trigger levels are quoted in the left column, while the hardware descriptions are quoted in the right column.

### 2.3.1 Decision flow and rejection rates

The LVL1 trigger uses a limited amount of all incoming data to make a decision in less than 2.5 $\mu$s. The data rate is reduced from the initial rate of 40 MHz to about 75 kHz that is passed on to the LVL2 trigger. The DAQ meanwhile buffers the raw data in pipeline memories until the event is either discarded or passed. The LVL1 searches for

- high-$p_\perp$ muons in the muon spectrometer,
- high-$p_\perp$ electrons and photons in the electromagnetic calorimeter,
- jets and $\tau$-leptons with hadronic decay modes in the hadronic calorimeter.

The muons are identified by the RPCs in the barrel and the TGCs in the end caps of the muon spectrometer. All calorimeter based trigger decisions are based on low granularity information from the calorimeter's trigger towers. An estimate of missing transverse energy $\not{E}_\perp$ is also built using the calorimeter information. The LVL1 also defines so-called **R**egions **o**f **I**nterest (RoI), which are $\eta$-$\varphi$ coordinates of all detector regions where the LVL1 trigger has fired. In case the event passes the LVL1, the RoIs are also handed to the LVL2 for further processing. The LVL2 trigger uses all information from all subsystems at full granularity and precision to reprocess the data and confirm the LVL1 decision. This step takes about 40 ms to process and reduces the total rate to about 3.5 kHz. Again, the raw data is buffered until the event is either accepted or rejected. For this purpose, a complex system of so-called **R**ead**o**ut **D**rivers (RoD) and **R**ead**o**ut **B**uffers (RoB) is provided, which also takes care of the correct time allocation of the incoming data. The final event filtering step is done by a processor farm. Here, each event is assigned to one node in the farm, which allows for long processing times due to high parallelity. To each event the full offline reconstruction and analysis is applied. The data is reduced to about 1.3 MB per event and the rate is suppressed to approximately 200 Hz in this final stage.

### 2.3.2 Trigger menus

Trigger menus are tables containing specifications for selection criteria at each trigger level. These selections are chosen appropriate to the ATLAS physics requirements as described in section 2.2.2. Preparing these specifications is a complex procedure which takes into account the desired physics coverage, rejection capabilities at the various selection stages as well as the estimate on the total output bandwidth. One distincts the following types of menus:

- inclusive physics triggers,
  which are configured to cover a large fraction of the main ATLAS physics program,
- pre-scaled physics triggers,
  which are basically inclusive triggers that provide lower threshold to increase the kinematic range to be able to investigate physics background and detector performance,

- exclusive triggers,
  which will extend the ATLAS physics coverage and

- monitor and calibration triggers,
  based on physics processes that are not otherwise needed in the course of the main ATLAS program.

Each trigger menu can hold up to 256 items, each corresponding to a physics objects. The notation of the item is as follows: The central part of the notation is the name of the physics object, e.g. "e" for electron, "$\mu$" for muon, "j" for jet, "$\tau$" for hadronic taus, "E" for the objects energy and "xE" for missing energy. It is followed by an integer number representing the selection criterion, which is the $E_\perp$-threshold in units of GeV which that object must pass. For particles, the item may be prefixed by an integer number representing the desired multiplicity of that object. The suffix "i" is found on items in the trigger menu of the intitial phase of ATLAS. To give an example, the item "2e15i" corresponds to the requirement of two electrons, each with $E_\perp > 15$ GeV. An excerpt of the trigger menu for the initial running is presented in Table 2.3

**Table 2.3:** Sample of ATLAS inclusive physics trigger items as they are intendet for the initial LHC phase. [9]

| trigger item | examples of physics coverage |
|---|---|
| e25i | $W \to e\nu$, $Z \to ee$, top quark production |
| $\mu$20i | $W \to \mu\nu$, $Z \to \mu\mu$, top quark production |
| 2$\mu$10i | $Z \to \mu\mu$ |
| 2$\gamma$20i | $H \to \gamma\gamma$ |
| $\tau$60i | charged Higgs |

# Chapter 3

# An overview of top quark physics

The investigation of the top quark has been one of the most exciting parts in the field of elementary particle physics in the past decade. The top quark was the last particle to complete the group of quarks in the standard model of particle physics and at the same time it stands at the forefront to enable a glance into new physics which may be beyond the standard model. The integration of the top quark in the standard model as well as the associated interaction mechanisms will be discussed in the first section of this chapter, followed by further sections focussing on the top quark itself, its history and its basic properties.

## 3.1 The standard model of particle physics

The standard model (SM) of particle physics describes our knowledge of the constituents of matter and the interactions between them. It is believed that matter in all its complexity as we find it around us consists of only a few basic particles. These particles are assumed to be elementary, which means that they are pointlike and do not have a further substructure. In the standard model these fundamental particles are divided into two classes: the spin–$\frac{1}{2}$ fermions, which are divided into the leptons and quarks and make up the actual matter, and the spin–1 gauge bosons, which are the carriers of the forces and thus are responsible for the interactions. To each particle $P$ an antiparticle exists which is denoted $\overline{P}$. Antiparticles have the same mass but opposite signed charge quantum numbers.

### 3.1.1 Fermions and gauge bosons

As already mentioned, the fermions are subdivided into the leptons and the quarks. The leptons are the electron $e^-$, the muon $\mu^-$ and the tau $\tau^-$ and their corresponding neutrinos $\nu_{e^-}$, $\nu_{\mu^-}$ and $\nu_{\tau^-}$. The quarks are called up $u$, down $d$, charm $c$, strange $s$, bottom $b$ and top $t$.

The quarks and leptons can be grouped together in three so called families or generations. Each generation is made up of two leptons and two quarks. The leptons are a pair of a massive lepton with the charge $-1$ in units of the elementary charge and a (nearly massless) neutrino with zero charge. The quarks are arranged in pairs, with one carrying an electric charge of $+2/3$ and the other of $-1/3$ . These two types of quarks are generally called the up-type and down-type quark with respect to the names of the quarks of the first generation. In one generation, the

two leptons and quarks each form weak isospin dubletts, since the two leptons and the two quarks are identical particles with respect to the weak interaction. A detailed discussion of the interactions is found in 3.1.2 as only a brief overview shall be given here.

Looking at the physical behaviour between the particles within one family, all three families are basically the same. The main difference between the generations are the masses of the particles; they increase continuously starting with the lightest family I that contains the electron as the lightest particle with about 511 keV (not counting the neutrinos here) up to family III with the top quark as the heaviest particle ($m_t = (173.1 \pm 1.3)$ GeV [10])[1] in the standard model.

The gauge bosons are the carriers of the interactions. They come as the massless and electrically uncharged photon $\gamma$ and gluon $g$ as well as the massive and electrically charged $W^+$- and $W^-$-bosons with a mass of about 80.4 GeV each and the uncharged $Z^0$-boson with a mass of about 91.2 GeV. Apart from their widely spread mass ranges and different charges, the gauge bosons are quite different from each other also concerning their behaviour during interactions.

Figure 3.1 provides an illustration of the particles and their classification in the SM. Also, their basic properties like mass and types of interactions are summarized.

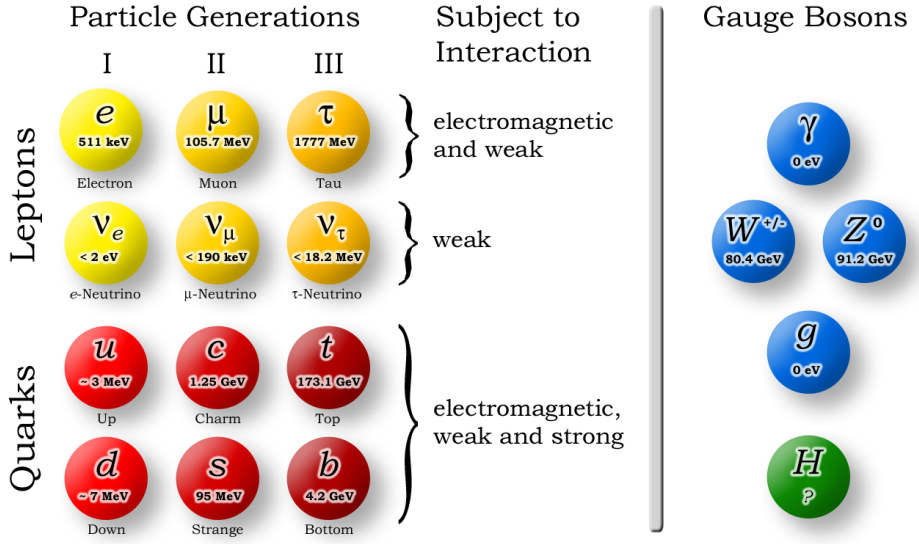


**Figure 3.1:** Illustration of the standard model of particle physics. The leptons and quarks are shown in their respective families; the gauge bosons are represented separately. The indicated Higgs boson has not yet been measured. For the sake of readability, note that only particles are shown and color freedom of the quarks and gluons is not represented. For the neutrino masses, upper limits as evaluated by the Particle Data Group are presented [11].

[1] Tevatron combined result as of March 2009

### 3.1.2 Fundamental interactions

There are four fundamental interactions on which all physics phenomena are based. The gauge bosons are the mediators of these interactions, they are exchanged between particles whenever they interact. However, not every particle is subject to every force. The particle must carry the corresponding charge that couples to the specific interaction. Therefore, the charge measures the strength of this interaction. This section provides an overview of the interactions (sorted by relative strength), their properties and their mediators. A short introduction to theoretical concepts is given. Also, the relative strengths of the interactions are compared via their charges.

#### Quantum Field Theories

Theoretical calculations are done by applying Quantum Field Theories (QFT) which provide extremely precise predictions. All QFTs require

- Lorentz invariance: the theory must hold in every reference frame,
- local gauge invariance: every symmetric gauge transformation must leave the physical field unchanged,
- renormalization: all calculations must converge. If single contributions result in ultraviolett divergencies, they must cancel with other similar contributions in the same calculus.

In QFTs the interactions are described by quantized fields where the mediator bosons are the quanta of the field. Whenever possible, the QFT of an interaction is treated perturbatively, i.e. in expansions of their so-called coupling parameters $\alpha$. Mathematically, an interactions coupling is nothing but its charge squared represented in natural units, in which it is a dimensionless quantity.

The coupling parameter depends on the energy scale at which the interaction takes place; this phenomenon is called 'running' of the coupling. Details on the runnings are discussed in the following; when comparing the strengths of the interaction, a scale of 1 GeV is chosen.

#### Strong interaction

The strong force binds quarks to hadrons which can be $q_1\overline{q}_2$ states called mesons or $q_1q_2q_3$ states called baryons. The most important baryons are the proton $|uud\rangle$ and neutron $|udd\rangle$ that make up our surrounding matter. The strong force also binds protons and neutrons together to nucleons. Quarks are the only particles that are subject to the strong interaction.

The charge of the strong interaction is called 'color' and therefore the field theory is called Quantum Chromo Dynamics QCD (gr. 'chroma' = color). The symmetry group of the fundamental representation is the $SU(3)$ group. The name 'color' has been chosen for the strong charge after the $\Omega^-$ baryon had been discovered in 1964 [12] which consists of three identical strange quarks in the configuration $s_1s_2s_3$. To fulfill Pauli's principle it was necessary to postulate a strong charge with three possible states so that the $s$-quarks within the $\Omega^-$ can be discriminated. These states have been called red (R), green (G) and blue (B), and their respective 'negative' charges are antired, antigreen and antiblue ($\overline{\text{R}}$, $\overline{\text{G}}$, $\overline{\text{B}}$).

The choice of these names reflects the fact that all bound states of quarks observed do not carry a strong charge, which means that they are color singlett and in consequence 'colorless' or 'white'. Generally speaking, the colors are confined within bound states of quarks. Possible configurations of colors to achive this are RGB or $\overline{\mathrm{RGB}}$ for baryons and R$\overline{\mathrm{R}}$+G$\overline{\mathrm{G}}$+B$\overline{\mathrm{B}}$ for mesons. In fact, color confinement states that quarks may not appear free, i.e. as stable single particles in a final state.

The mediating particle of the strong force is the gluon $g$ which carries the color charge of the strong force. Since gluons interconnect between two differently colored quarks, they always carry combinations of colors. Due to the $SU(3)$ symmetry, there are eight of these color combinations, so we factually distinguish eight different gluons. Although a gluon is a massless particle with zero electrical charge, the strong force does not have an infinite range since gluons interact with each other due to their color charge.

The running of the coupling is such that the strength of the coupling decreases with increasing energy. At high energies, this can be described in a first order calculation by the form [13, 14]

$$\alpha_{\mathrm{QCD}}(Q^2) \equiv \alpha_S = \frac{12\pi}{(33 - 2n_f) \ln\left(\frac{Q^2}{\Lambda^2_{\mathrm{QCD}}}\right)} \quad , \tag{3.1}$$

where $Q^2 = -q^2$ ist the momentum transfer of the interaction carried by the gluon and $n_f$ is the number of flavors realized by nature.

The parameter $\Lambda_{\mathrm{QCD}}$ is the energy scale of the strong interaction. In the region of $Q^2 = \Lambda^2_{\mathrm{QCD}}$ the coupling gets strong enough to arrange the quarks and gluons into bound states called hadrons as named above. The numerical value of $\Lambda_{\mathrm{QCD}}$ is therefore in the order of typical hadron masses; the value that is used throughout this thesis is $\Lambda_{\mathrm{QCD}} = 250$ MeV[2]. At large energy scales $Q^2 > \Lambda^2_{\mathrm{QCD}}$ the strength of the coupling is small and the quarks are less bound by the strong interaction, a phenomenon known as asymptotic freedom.

The strength $\alpha_S$ of the strong interaction has been measured in various experiments at different energy scales. Most commonly quoted are measurements at an energy of $m_Z = 91.2$ GeV, leading to a world average of $\alpha_S(m_Z) = 0.1176 \pm 0.002$ [11]. Measurements at other energy ranges [11, 14] allow to determine $\alpha_S$ at the scale of 1 GeV, where one finds that $\alpha_S$ is in the order of $\approx 1$.

**Electromagnetic interaction**

Electromagnetism is the best established fundamental interaction. Its theory is the Quantum Electro Dynamics (QED); its symmetry group is $U(1)$. The QED provides high precision predictions on the coupling constant $\alpha_{\mathrm{QED}}$ which is confirmed by measurement up to a precision of $10^{-11}$ [15, 16]. Common everyday physics like electricity and magnetism are based on QED. It affects all particles that have a non-zero electric charge. Its mediator is the uncharged and massless photon $\gamma$, and its range is infinite. $\alpha_{\mathrm{QED}}$ is also called the fine structure constant, since it originally was introduced by A. Sommerfeld in his discussion of fine structure splitting in Hydrogen and Helium [17]. The numerical value of $\alpha_{\mathrm{QED}}$ can be

[2] This value has been chosen to be consistent with the general ATLAS convention; usually a value of $\Lambda_{\mathrm{QCD}} = 200$ MeV is quoted.

calculated as

$$\alpha_{\mathrm{QED}} \equiv \alpha_0 = \frac{1}{4\pi\epsilon_0} \cdot \frac{e_0^2}{\hbar c} = 7.297\,352\,568(24) \cdot 10^{-3} \approx \frac{1}{137}. \tag{3.2}$$

The running of $\alpha_{\mathrm{QED}}$ at high $Q^2$ can be expressed by [13]

$$\alpha_{\mathrm{QED}}(Q^2) = \frac{\alpha(\mu^2)}{1 - \frac{\alpha(\mu^2)}{3\pi} \ln\left(\frac{Q^2}{\mu^2}\right)} \quad , \tag{3.3}$$

where $\alpha(\mu^2)$ is the reference value at a low energy renormalization momentum $\mu^2$. Although $\alpha_{\mathrm{QED}}(Q^2)$ in principle diverges, one finds that the absolute effect on $\alpha$ is extremly small by inserting reasonable numerical values for $Q^2$ and $\mu^2$. We therefore use the estimation

$$\alpha_{\mathrm{QED}}(\mu = 1\ \mathrm{GeV}) = \alpha_0 \approx \frac{1}{137} \tag{3.4}$$

and for the relative strength of the electromagnetic interaction to the strong interaction at an energy of 1 GeV

$$\frac{\alpha_{\mathrm{QED}}}{\alpha_S} \approx 10^{-2}\,. \tag{3.5}$$

**Weak interaction**

The best-known physics phenomenon based on the weak interaction on the macroscopic scale is the beta decay of the nuclei. Though it is the second weakest interaction, it plays an important role in the subatomic scale since it affects all fundamental fermions, i.e. leptons and quarks. The symmetry group of the weak interaction is $SU(2)$.

The weak interaction is described by the so called $V$-$A$ theory (**V**ector - **A**xial vector), which refers to the formal structure of the weak interactions current. This structure involves some features which are unique to the weak interaction, for example the violation of Parity, which had been described by Lee and Yang (Nobel-Price in 1957) [18] and measured by the Wu-Experiment [19]. A consequence is that the weak interaction couples only to left-handed particles and right handed antiparticles. This was demonstrated in the experiment of Goldhaber which measured the helicity of neutrinos [20]. Nowadays, the weak interaction is decribed in a unification with the electromagnetic theory by S. L. Glashow, A. Salam and S. Weinberg in the so-called electroweak or GWS-Theory, which has a $SU(2) \times U(1)$ symmetry. It is another successful unification of two forces after e.g. the unification of electricity and magnetism, which has been accomplished by James Maxwell in the $19^{\mathrm{th}}$ century.

The quantum number corresponding to the weak interaction is called flavor. The fundamental fermions are distinguished by their flavors, in other words, the flavor is simply the name of the fermion. There are 12 flavors in total, six for the leptons: $e$, $\mu$, $\tau$, $\nu_e$, $\nu_\mu$, $\nu_\tau$ and six for the quarks: $u$, $d$, $c$, $s$, $t$, $b$. In the representation of the weak interaction, each fermion is an eigenstate of the weak interactions Hamiltonian. The mass eigenstates are then created by superposition of the flavor eigenstates. This implies that a particle can change its flavor in weak interactions, with the restriction that leptons can only convert into leptons and quarks into quarks.

This so called 'mixing' is possible between two fermions of the same type (up-type to up-type and down-type to down-type) as well as from up-type to down-type or vice versa. If the type of fermion is not changed, the conversion process is called a flavor changing neutral current (FCNC), since fermions of the same type have the same electrical charge. FCNCs occur only in higher order pertubational calculations and are highly suppressed due to the GIM mechanism [21]. The charge altering processes, i.e. the transition of a fermion to that of a different type, are therefore preferred by nature.

The existence of charged as well as neutral flavor changes implies more than one mediating boson of the weak interaction. The mediators are the two massive bosons $W^+$ and $W^-$ with masses of $m_W = (80.40 \pm 0.03)$ GeV each and the neutral $Z^0$ with a mass of $m_Z = (91.188 \pm 0.002)$ GeV [11].

For the quark sector, the charged current mixing is described by the Cabibbo-Kobayashi-Maskawa (CKM) Matrix $V_{CKM}$, which is a unitary 3×3 matrix. Each matrix element squared $|V_{qq'}|^2$ is directly proportional to the propability of the transition $q \to q'$. The mixing can be described by

$$V_{CKM} \cdot \begin{pmatrix} |d\rangle \\ |s\rangle \\ |b\rangle \end{pmatrix} = \begin{pmatrix} V_{ud} & V_{us} & V_{ub} \\ V_{cd} & V_{cs} & V_{cb} \\ V_{td} & V_{ts} & V_{tb} \end{pmatrix} \begin{pmatrix} |d\rangle \\ |s\rangle \\ |b\rangle \end{pmatrix} = \begin{pmatrix} |d'\rangle \\ |s'\rangle \\ |b'\rangle \end{pmatrix} . \tag{3.6}$$

Though the values for the matrix elements $|V_{qq'}|^2$ are important parameters in the SM, they are not predicted by theory but are obtained by measurements. By global fit to the SM [11] one obtains the CKM matrix as shown in eq. (3.7). Here, only the absolute values of the matrix elements are shown.

$$|V_{CKM}| = \begin{pmatrix} |V_{ud}| & |V_{us}| & |V_{ub}| \\ |V_{cd}| & |V_{cs}| & |V_{cb}| \\ |V_{td}| & |V_{ts}| & |V_{tb}| \end{pmatrix} = \begin{pmatrix} 0.97383 & 0.2272 & 0.00396 \\ 0.2271 & 0.97296 & 0.04221 \\ 0.00814 & 0.04161 & 0.9991 \end{pmatrix} . \tag{3.7}$$

The diagonal elements show that the preferred flavor changing in the quark sector occurs always within a family ($> 97\%$ propability in each family).

An estimation of the relative strength of the weak force is heavily depending on the choice of the energy scale, since a lot of weakly interacting hadrons exist within a wide range of masses. To calculate the relative strength of the weak force at our chosen energy scale of 1 GeV we compare the decay of two particles at this mass scale. One of the decays shall be initiated by the strong interaction and one by the weak interaction. A good choice are the two baryons $\Delta^+$ with a mass of $m_{\Delta^+} \approx 1.20$ GeV and the $\Sigma^+$ with $m_{\Sigma^+} \approx 1.19$ GeV. Both particles decay into a proton $p$ and a $\pi^0$, but they are starting from different quark contents [14]:

$$\begin{aligned} \Delta^+ \to p + \pi^0 \quad &= \quad uud \to uud + \frac{u\bar{u} + d\bar{d}}{\sqrt{2}} \\ &\text{and} \\ \Sigma^+ \to p + \pi^0 \quad &= \quad uus \to uud + \frac{u\bar{u} + d\bar{d}}{\sqrt{2}} \end{aligned}$$

Since the decay of the $\Sigma^+$ involves a transition of an $s$ quark to a $u$ quark, it can only happen in a weak interaction. One finds that the lifetimes of the particles differ in orders of magnitude, although their masses are comparable. This can only be explained by the different coupling strengths, since the decay rate or inverse lifetime depends on the coupling strength squared. The $\Delta^+$ baryon undergoes a

strong decay and has a lifetime of $6 \cdot 10^{-24}$ sec, while the weakly decaying $\Sigma^+$ has a lifetime of $8 \cdot 10^{-11}$ sec [14]. From this we conclude:

$$\frac{\alpha_W}{\alpha_S} = \sqrt{\frac{\tau_{\Delta^+}}{\tau_{\Sigma^+}}} \approx 10^{-6}\,. \tag{3.8}$$

**Gravitation**

The gravitation mediates between the masses of all particles and is the weakest of all forces on the subatomic scale. Yet, it plays an important role in macroscopic physics due to its infinite range. The detection of a possible mediator, usually called 'graviton', is still pending. Gravitons are expected to be spin–2 particles with a zero mass and no electrical charge. The theory of gravitation is well described by general relativistics but, up to now, no quantization of the gravitational field has been possible. Nevertheless, the relative strength of the gravitation can be estimated by comparing the electromagnetic and gravitational attraction between an electron and a proton using classical mechanics and electrodynamics:

$$\frac{F_G}{F_{el}} = \frac{G\, m_p\, m_e}{\frac{1}{4\pi\epsilon_0} e_0^2} \approx 4 \cdot 10^{-40}\,. \tag{3.9}$$

This calculation of course depends on the masses used for comparison, as well as on the particles charges. Nevertheless, the order of magnitude demonstrates the low strength of the Gravitation, for which it is usually not mentioned in the standard model when treating subatomic scales. Therefore, it will be neglected in all further discussions.

### 3.1.3 The Higgs mechanism

In contrast to the massless gauge bosons of the electromagnetic and strong interactions, the mediators of the weak interaction are observed to be massive ($\mathcal{O} m_{W,Z} = 100$ GeV). In the standard model this is explained by the Higgs mechanism, which introduces a background field that through interaction with the particles generates mass on them [13, 22].

The field quantum of the Higgs field is called the Higgs boson $H$. Up to now it has not been observed by experiments. The possible value of the Higgs mass is mainly dominated by two parameters: the mass of the top quark $m_t$ and the mass of the $W$-boson $m_W$. The more precise each of these masses is known, the more precise the Higgs mass can be predicted. It is also possible that a scenario involving a standard model Higgs has to be discarded; in this case, the Higgs boson may be part of a possible minimal supersymmetric extension of the standard model MSSM. The relation of $m_t$, $m_W$ and $m_H$ and the possibility of a MSSM is a crucial point in the discussion whether the standard model will provide the final answer to all particle physics questions or not. Since the mass of the top quark plays an important role in this question, the matter of Higgs boson searches will be discussed in detail in section 3.3.2.

## 3.2 The top quark

### 3.2.1 Brief summary of basic top quark properties

The top quark $t$ is the heaviest discovered particle within the standard model of particle physics. It has been discovered in 1995 at the Tevatron $p\bar{p}$-collider [23,24], which is located at the Fermi National Accelerator Laboratory or Fermilab 50 km to the west of Chicago. The Tevatron is the last in a series of accelerator devices and storage rings, build to store protons and antiprotons and accelerate them to an energy of 0.98 TeV each, creating a center of mass energy of $\sqrt{s} = 1.96$ TeV. The Tevatron hosts two major multipurpose particle physics experiments called DØ [3] and CDF[4]. A detailed desciption of the detectors and their role in the discovery of the top quark is found elsewhere [23, 24].

The discovery of the top quark has long been anticipated since the bottom quark had been found with the discovery of the first $\Upsilon$-resonance in 1977 [25]. The $b$-quark indicated a third generation of quarks, which was unknown at that time. Originally called "beauty", this fifth quark was soon assumed to have a weak isospin partner, which was referred to as the "truth"-quark. Later on, these names were changed into their now common names bottom and top to reflect their down-type and up-type nature. The top quark therefore has isospin $T_z = +1/2$ and electrical charge $Q_t = 2/3\ e_0$. Although since the discovery a few thousand top quark events have been observed, most of the basic properties, especially the quantum numbers like electrical charge or spin, have not or not precisely been measured. Approaches to measure the charge and the spin of the top quark will be described in section 3.5.

The mass of the top quark is its best known property up to now. The current world average presented by the Tevatron experiments is $m_t = (173.1 \pm 1.3)$ GeV as of March 2009 [10]. As the focus of this thesis lies on the top mass measurement, further details on this topic will be given in section 3.4.

### 3.2.2 Phenomenology of hadron collisions

The Tevatron as well as the upcoming LHC are hadron colliders. While the Tevatron collides $p$ on $\bar{p}$, the LHC uses $p$ on $p$. Nevertheless, since protons and antiprotons are composed particles, the collision itself takes place between their constituents, i.e. the partons, rather than the primary particles themselves. The collision of two hadrons is therefore identical with the interaction of the quarks and gluons within the hadron, each carrying a momentum fraction $x$ of the parent hadron. Since $x$ may vary from collision to collision, it is impossible to predict the absolute energy of a single collision, which is possible in $e^+e^-$ colliders. The effective center of mass energy squared is therefore

$$\hat{s} = x_i x_j s \tag{3.10}$$

where $i$ and $j$ are the respective interacting partons of the hadron. Since $x_i$ and $x_j$ will usually be unequal and also differ from collision to collision, the absolute center of mass energy of the colliding system is unpredictable, making hadron collisions very difficult to analyze.

[3] DØ (D-Zero) is simply the name of the experiments interaction point
[4] **C**ollider **D**etector at **F**ermilab

To be able to make predictions on the cross sections of physics processes, one has to know the probability density for finding a parton $i$ with a certain momentum fraction $x_i$ at the chosen momentum transfer scale $Q$, which is called the parton distribution function (PDF) $f(x_i, Q)$. These PDFs are extracted by global QCD fits from deep inelastic scattering experiments. Various of such experiments have been carried out in the past, such as fixed target experiments at CERN, SLAC and Fermilab as well as $e^+p$ collisions at the HERA collider at DESY [26, 27]. Figure 3.2 shows example parameterisations of PDFs.

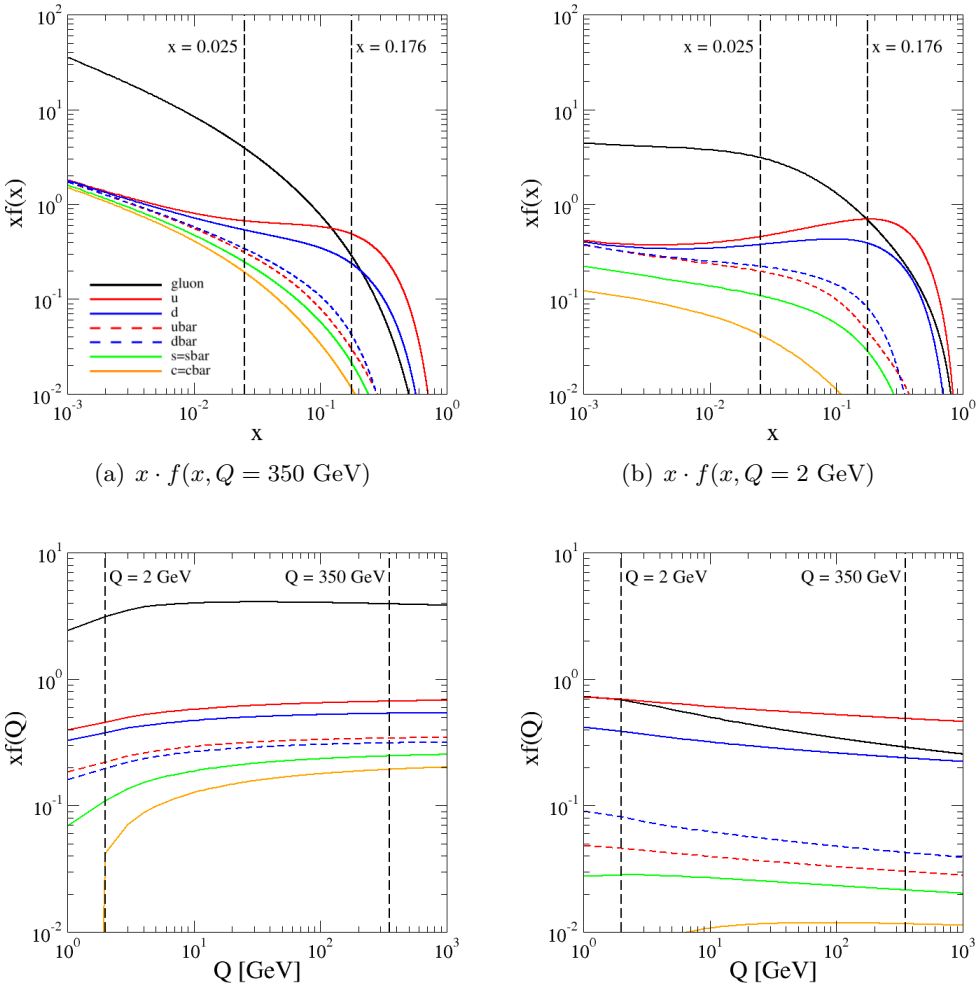


(a) $x \cdot f(x, Q = 350\ \text{GeV})$

(b) $x \cdot f(x, Q = 2\ \text{GeV})$

(c) $x \cdot f(x = 0.025, Q)$

(d) $x \cdot f(x = 0.176, Q)$

**Figure 3.2:** The parton densities of the proton as a function of their momentum fraction $x$ at fixed momentum transfer scale $Q$ ((a) and (b)) and as a function of $Q$ at fixed $x$ ((c) and (d)). The respective fixed scales are $Q \approx 2 \cdot m_t = 350$ GeV (a) and $Q = 2$ GeV (b). The fixed values of $x = 0.025$ (c) and $x = 0.176$ (d) represent the momentum fractions for the $t\bar{t}$ threshold at LHC and Tevatron assuming a symmetric $x$ as will be shown in 3.2.3. The distributions have been plotted with LHAPDF [28] using the CTEQ6M parametrisation [29].

Especially in the regions of low momentum transfers $Q$ one can clearly see the domination of $u$-quarks and $d$-quarks in the high $x$-range. We call these quarks the "valence quarks" of the proton, whilst all other non-dominating partons, i.e. the virtual $q\bar{q}$ pairs and the gluons, are referred to as the "sea". The shape of these distributions strongly determines the production mechanism of top quarks at hadron colliders, which will be discussed in the next section.

### 3.2.3 Top quark production in hadron collisions

The top quark can be produced either in strong interactions or in electroweak interactions. Since in $pp$ or $p\bar{p}$ collisions gluons are available from the very start and the strong interaction is a factor $10^6$ stronger, the strong production is by far the dominating process.

#### Strong pair production of top quarks

In the strong production, top quarks are produced in $t\bar{t}$ pairs either via $q\bar{q}$-annihilation or via gluon-gluon fusion. Figure 3.3 shows the Feynman diagrams for the lowest order strong $t\bar{t}$ production.

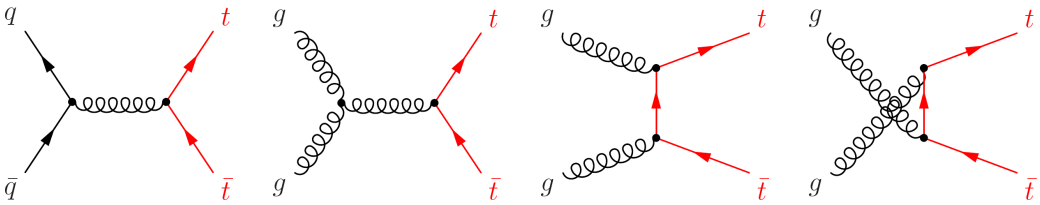


**Figure 3.3:** Feynman diagrams for the strong $t\bar{t}$ production. (a): quark-antiquark annihilation, (b) to (d): gluon-gluon fusion.

The cross section of the $t\bar{t}$ production can be calculated as [30]:

$$\begin{aligned}\sigma^{t\bar{t}}(\sqrt{s}, m_t, Q^2) &= \sum_{i,j} \int \mathrm{d}x_i \mathrm{d}x_j f_i(x_i, Q^2) f_j(x_j, Q^2) \\ &\times \quad \sigma^{ij\to t\bar{t}}(\rho, m_t^2, x_i, x_j, \alpha_S(Q^2), Q^2) \quad . \end{aligned} \tag{3.11}$$

Here, the summation indices $i$, $j$ run over all possible parton combinations $q\bar{q}$, $gg$, $gq$, $g\bar{q}$ and $\rho = 4m_t^2/\sqrt{\hat{s}}$ where $\hat{s}$ is the effective center of mass energy squared as defined in eq. (3.10). In case of the $t\bar{t}$ production we can apply the constraint $\hat{s} \geq 4m_t^2$, since the collision of two partons must produce at least enough energy to create a $t\bar{t}$ pair at rest. Using eq. (3.10), this constraint can be written as

$$x_i x_j \geq 4m_t^2/s\,. \tag{3.12}$$

To estimate a typical value of $x$ we set $x_i \approx x_j \equiv x$ and obtain [30]

$$x \approx 2m_t/\sqrt{s} \tag{3.13}$$

$$= 0.176 \qquad \text{(Tevatron Run II)} \tag{3.14}$$

$$= 0.025 \qquad \text{(LHC)} \tag{3.15}$$

Comparing these numbers using Figure 3.2, one can conclude that the strong production mechanism of $t\bar{t}$ pairs is different between Tevatron and LHC. While at Tevatron the production will be dominated by $q\bar{q}$-annihilation, the LHC will be dominated by $gg$-fusion. Table 3.1 summerizes the calculated cross sections for both LHC and Tevatron and lists the production branching ratios for an assumed top mass of $m_t = 175$ GeV. All calculations are done in NLO+resummation of LL and NLL soft logarithms appearing at all orders of pertubation theory. The uncertainties on $\sigma^{t\bar{t}}$ for both Tevatron and LHC have been estimated through the uncertainty on the $Q$-scale by calculating the cross section for an assumed double and half size scale: $Q = 2 \cdot m_t$ and $Q = 0.5 \cdot m_t$. The Tevatron number additionally contains the error on the PDF.

**Table 3.1:** Calculated cross sections and production branches for the strong $t\bar{t}$ production at the Tevatron and LHC.

| | $\sqrt{s}$ [TeV] | $\sigma^{t\bar{t}}$ [pb] | $q\bar{q} \rightarrow t\bar{t}$ | $gg \rightarrow t\bar{t}$ |
|---|---|---|---|---|
| Tevatron (Run II) | 1.96 | $6.76 \pm 0.21$ [31] | 85% | 15% |
| LHC | 14 | $833^{+52}_{-39}$ [32] | 10% | 90% |

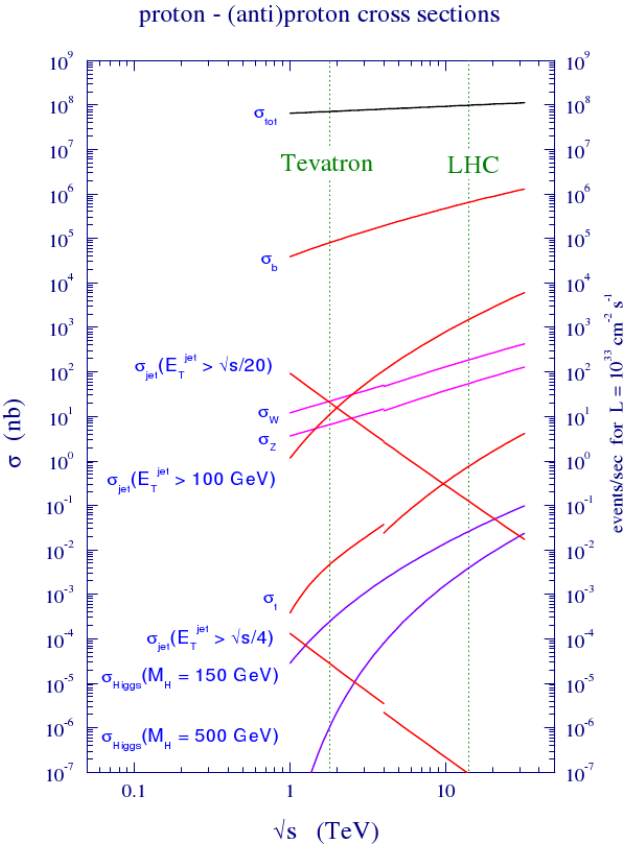


**Figure 3.4:** QCD predictions for hard-scattering cross sections at the Tevatron and the LHC [33]. The total cross section of proton-proton collisions for both colliders are also shown; at LHC, this is estimated to be (125±25) mb [34].

Applying the $t\bar{t}$ cross section of LHC to an assumed integrated luminosity of 1 fb$^{-1}$, one finds that approximately 833000 top quark pairs will be produced within ten days of an ideal running. This demonstrates that the LHC will be a top factory providing the possibility to investigate top quarks at very high statistics. For comparison, the predicted production cross sections for typical QCD processes at both Tevatron and LHC conditions are summarized in Figure 3.4.

### Weak single top quark production

In the standard model single top quarks can only be produced in weak interactions since they do not conserve flavor as described in section 3.1.2. Interesting features of single top investigations are e.g. the possibility to measure the CKM matrix element $|V_{tb}|^2$ since it is proportional to the cross section of single top production, as well as the possibility to investigate charge assymmetries at the LHC arising from the very nature of $pp$-collisions.
A 5.0 $\sigma$ observation of single top quarks has been reported from both DØ [35] as well as CDF [36].
One finds three possible production mechanisms:

(a) NLO $W$-boson and gluon fusion mode, which includes the LO t-channel contribution and is referred to as t-channel or $Wg$ as a whole,

(b) s-channel production,

(c) production of a top quark in association with a $W$-boson, shortly referred to as 'associated production' or simply $Wt$.

The corresponding Feynman diagrams are shown in Figure 3.5.

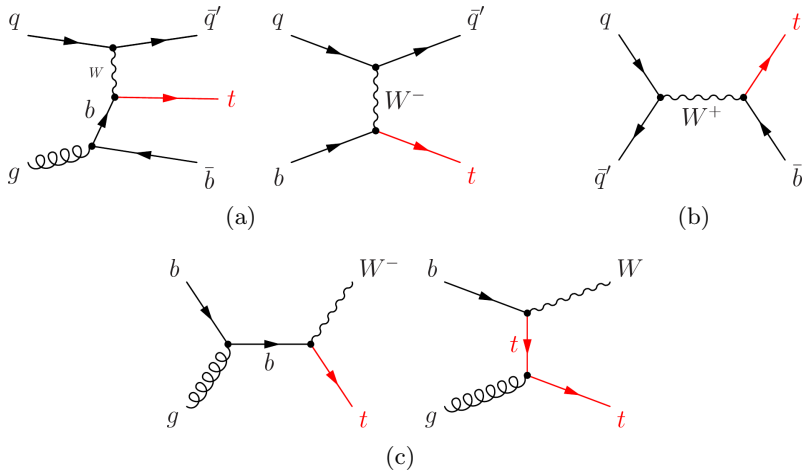


**Figure 3.5:** First order Feynman diagrams for weak single top production at the LHC: (a) $Wg$ fusion and t-channel, (b) s-channel, (c) associated production $Wt$

Due to the nature of weak interactions the single top production cross section is smaller than the one for the strong $t\bar{t}$ production. The total NLO cross sections sum up to about 1.5 pb for Tevatron (Run II) and about 320 pb for the LHC. A detailed overview of the contributions from the different production modes is given in Table 3.2.

**Table 3.2:** Calculated NLO cross sections for the weak single top production at the Tevatron and LHC for the main processes. If available, the cross sections are given separately for the respective top and antitop contribution. All evaluations are done using the CTEQ PDF parametrization. For the s- and t-channel, a top mass of $m_t = 175$ GeV has been used while for the $Wt$ production $m_t = 178$ GeV was assumed. Note that for $Wt$ from [37] the author quotes LO and NLO cross sections separately, and that the uncertainties strongly depend on the chosen scales.

| Process | Collision, $\sqrt{s}$ | | $\sigma_{LO+NLO}$ [pb] | Reference |
|---|---|---|---|---|
| $Wt$ | $p\bar{p}$, 1.96 TeV | | $\approx$0.113 | [37] |
| | $pp$, 14 TeV | | $\approx$65.57 | |
| t-channel | $p\bar{p}$, 1.96 TeV | $t$ | $0.99^{+0.14}_{-0.11}$ | |
| | $pp$, 14 TeV | $t$ | $155.9^{+7.5}_{-7.7}$ | [38] |
| | $pp$, 14 TeV | $\bar{t}$ | $90.7^{+4.3}_{-4.5}$ | |
| s-channel | $p\bar{p}$, 1.96 TeV | $t$ | $0.442^{+0.061}_{-0.053}$ | |
| | $pp$, 14 TeV | $t$ | $6.56^{+0.69}_{-0.63}$ | [38] |
| | $pp$, 14 TeV | $\bar{t}$ | $4.09^{+0.43}_{-0.39}$ | |

Single top events are a major background to $t\bar{t}$ physics due to the similar event topology and kinematic range. Note that the above cross sections hold for the total processes only; depending on the final particles emerging from the final state $W$-boson or quark and the type of investigation on $t\bar{t}$, the subsets of single top physics contributing to the background may vary. The respective contributions relevant for this thesis and their cross sections will be discussed separately in section 4.1.3.

### 3.2.4 Top quark decays

The decay of top quarks shows a very unique feature among the quarks. Its decay width as predicted by standard model NLO calculations [39] is approximately[5] given by :

$$\Gamma_t = \Gamma_t^0 \left(1 - \frac{m_W^2}{m_t^2}\right)^2 \left(1 + 2\frac{m_W^2}{m_t^2}\right) \left[1 - \frac{2\alpha_S}{3\pi}\left(\frac{2\pi^2}{3} - \frac{5}{2}\right)\right] \tag{3.16}$$

[5]Terms containing $m_b^2/m_t^2$, $\alpha_s^2$ and $\alpha_s \cdot (m_W^2/m_t^2)$ are neglected.

Here, $\Gamma_t^0$ is total width of the top quark calculated at leading order[6], given by $\Gamma_t^0 = G_F m_t^3 / 8\pi\sqrt{2}$. Applying a top mass of $m_t = 175$ GeV in 3.16, one finds the width of the top quark to be $\Gamma_t = 1.5$ GeV and therefore its lifetime of about $\tau_t = 1/\Gamma_t \approx 0.5 \cdot 10^{-24}$s. This is about 20 times smaller than the hadronization time scale $\tau_{Had} = 10^{-23}$s, hence the top quark will not build hadronic bound states. Instead, the top decays as a "free particle" via weak interaction. Viewing the CKM matrix (eq. (3.7)) it becomes clear that the top decays almost exclusively into a $b$-quark and a $W$-boson. The $b$-quark will either hadronize directly or further decay into a $c$-quark which will then hadronize. As a consequence, it will end up as a particle jet inside the hadronic calorimeter. The $W$-boson can decay either leptonically into a pair of a lepton and a neutrino or hadronically into a pair of one up-type and one down-type quark, also creating hadronic jets in the detector. One has to take into account though that the $W$-decay $W \to t\bar{b}$ is forbidden by kinematic reasons, only decays into the first two quark families contribute: $W \to u\bar{d}, c\bar{s}$. Figure 3.6 shows the Feynman diagram of the top quark decay with both possible final states of the $W$-boson.

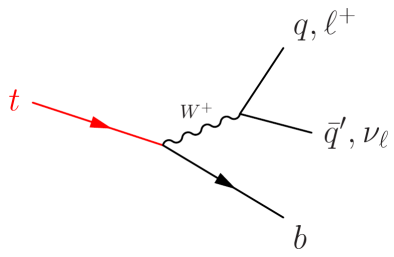


**Figure 3.6:** Feynman diagram of the top quark decay.

To a first approximation these $W$-bosons decay channels are equally valid. There are nine decay modes in total, three leptonic modes and two hadronic modes, of which each appears in a threefold multiplicity due to the additional degree of freedom arising from the quarks color-charge. This creates probabilities of 3/9 for the leptonic mode and 6/9 for the hadronic mode. The exact branching fractions as obtained from measurements are listed in Table 3.3.

**Table 3.3:** The decay modes of the $W^+$-boson as presented by the Particle Data Group [11]. The $W^-$-modes are charge conjugates of these modes. Note that the total sum of the branching fraction is only compatible to 100% if the uncertainties are taken into account.

| $W^+$-decay mode | Branching fraction [%] |
|---|---|
| $e^+\nu_e$ | $10.75 \pm 0.13$ |
| $\mu^+\nu_\mu$ | $10.57 \pm 0.15$ |
| $\tau^+\nu_\tau$ | $11.25 \pm 0.20$ |
| hadrons | $67.60 \pm 0.27$ |

[6]The NLO calculation presented here includes linear corrections on $\alpha_S$ as well as on $m_b$ and $m_W$ but neglects the respective squared terms.

The decay of a $t\bar{t}$ pair is now characterized by the decay of the respective $W$-bosons. Three possibilities arise:

- fully leptonic $t\bar{t}$
  Both $W$-bosons decay leptonically. This channel is also referred to as the dilepton channel, abbreviated $2\ell$.

- semileptonic $t\bar{t}$
  One $W$ decays hadronically into a pair of quarks while the other one decays into leptons. This channel is also referred to as the lepton+jets channel, abbreviated $\ell + j$.

- fully hadronic $t\bar{t}$
  Both $W$-bosons decay into quark pairs. This channel is also referred to as the all-jets channel, abbreviated $jj$.

In detail, each of the possible decay modes from one $W$-boson can be combined with the respective other one. The probability for each channel is listet in Table 3.4, as calculated from the individual probabilities given in Table 3.3. Note that the all-jets probability has been calculated as the difference of the sum of the other values to to 100% rather than from Table 3.3 to ensure the compatibility to a 100% total $t\bar{t}$ fraction. A common graphical representation of the probabilities is shown in 3.7 next to the table.

| $t\bar{t}$ decay channel | Branching fraction |
|---|---|
| $t\bar{t} \to e + e$ | 1.16 % |
| $t\bar{t} \to \mu + \mu$ | 1.12 % |
| $t\bar{t} \to \tau + \tau$ | 1.27 % |
| $t\bar{t} \to e + \mu$ | 2.27 % |
| $t\bar{t} \to e + \tau$ | 2.42 % |
| $t\bar{t} \to \mu + \tau$ | 2.38 % |
| $t\bar{t} \to e+$ jets | 14.53 % |
| $t\bar{t} \to \mu+$ jets | 14.29 % |
| $t\bar{t} \to \tau+$ jets | 15.21 % |
| $t\bar{t} \to$ all jets | 45.35 % |

**Table 3.4:** Numeric representation of the $t\bar{t}$ decay branching fractions

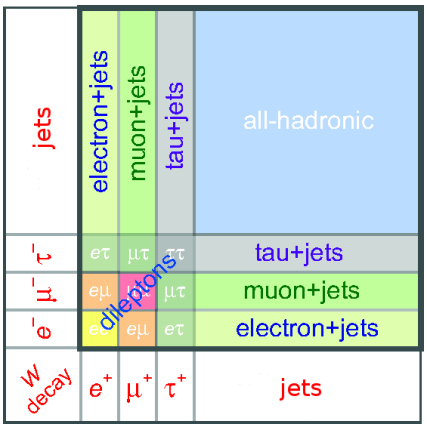


**Figure 3.7:** Graphical representation of the branching fractions in $t\bar{t}$ decays.

The topology of the three decay modes bears advantages as well as disadvantages to their investigation arising from their signatures in the detector.

First of all, each mode contains two jets from $B$-hadrons that emerge from the $b$-quarks from the top decays, providing the possibility to use $b$-tagging. This is a great advantage since $b$-tagging is a powerful tool if used carefully. More on the technique of $b$-tagging in ATLAS, its advantages and also difficulties is found in section 4.3.5.

Another advantage is the presence of high-$p_\perp$ electrons and muons from the leptonic $W$-decay which can be used as a trigger in the semi- and dileptonic mode. Since such a lepton is accompanied by a high-energy neutrino, one also finds large missing transverse energy $\not{E}_\perp$, which can be used to distinguish the event from low-$Q^2$ QCD background. Note however that the presence of two leptons in the

dileptonic mode underdetermines the event since only the total sum of $\not{E}_\perp$ can be measured. Also note that the leptonic $W$-decay in the $\tau$-mode is difficult to handle, since the $\tau$-lepton has a large mass and will therefore decay further into leptons as well as quarks in weak interactions, making it difficult to identify. For this reason it is usually treated separately, dividing the leptonic $W$-decay mode into the $(e, \mu)$-channel and the $\tau$-channel.

A general drawback is the high multiplicity of particle jets in $t\bar{t}$ events as jets appear in QCD background. This is especially a problem in the fully hadronic channel which has six jets, more preciseley two jets from the $b$-quarks and two jets each from the hadronic $W$-decay. As a consequence, the semileptonic channel has four jets and the dileptonic channel has two jets.

One also has to keep in mind that the respective decay channels occur in different statistics as can be seen in Table 3.4. This is not a disadvantage in the first place when speaking of the large statistics of $t\bar{t}$ events that will be produced in the LHC, but it has to be taken into account when it comes to simulation based studies, since the production of sufficiently sized samples requires computing time and disk space.
Table 3.5 summarizes the event topologies of the $t\bar{t}$ decay modes.

**Table 3.5:** Summary of the possible topologies of $t\bar{t}$ decays.

| $t\bar{t}$ decay mode | number of jets | thereof $b$-jets | presence of leptons | presence of $\not{E}_\perp$ | fraction in 100 % $t\bar{t}$ |
|---|---|---|---|---|---|
| dileptonic (incl. $\tau$-modes) | 2 | 2 | $2\times(e, \mu, \tau)$ | $2\times$ $\not{E}_\perp$ (under-det.) | 10.62 % |
| semileptonic ($e, \mu$-mode) | 4 | 2 | $1\times(e, \mu)$ | $1\times$ $\not{E}_\perp$ (well-det.) | 28.82 % |
| semileptonic ($\tau$-mode) | 4 (5) | 2 | $1\times\tau$ | $1\times$ $\not{E}_\perp$ (well-det.) | 15.21 % |
| fully hadronic | 6 | 2 | none | none | 45.70 % |

The fully hadronic channel is the most difficult channel to investigate. Although it appears in nearly half of all $t\bar{t}$ events, it suffers from a high jet multiplicity, no lepton and no missing energy. In contrast, the dilepton channel provides two leptons, but is under-determined with respect to missing energy and also suffers from low statistics.

The semileptonic channel is also called the 'golden channel' of $t\bar{t}$ decays. It has medium number of jets, of which two are $b$-jets, one lepton which is good for triggering and a well-determined $\not{E}_\perp$ due to the lepton, which makes the event well distinguishable from most physics background. The analysis performed in the context of this thesis will therefore focus on the semileptonic channel, yet the other channels will also be discussed if appropriate.

## 3.3 The top quark and its mass

### 3.3.1 The search for the top quark

Within the almost 30 years from the discovery of the $b$-quark in 1977 until the discovery of the top quark the lower bound on the top quark mass has been continually raised by direct searches, which were performed by hadron colliders as well as lepton colliders at both CERN and Fermilab. Figure 3.8 shows the historical development of the limits on the top quark mass in the last years until its discovery.

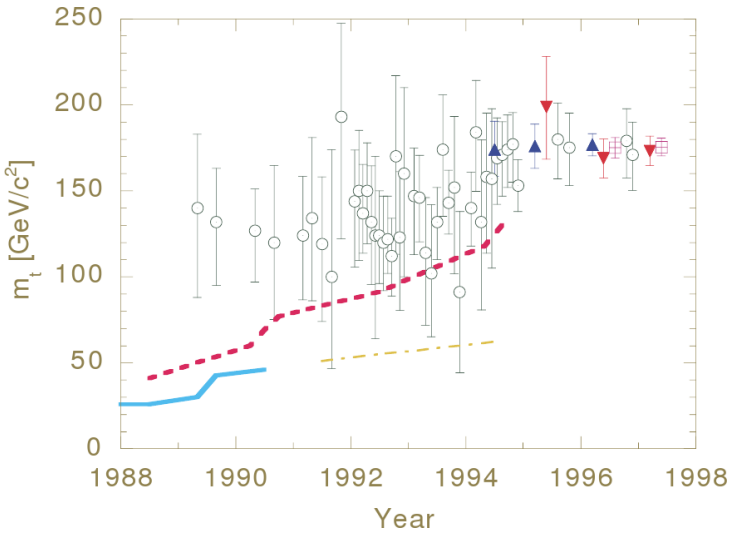


**Figure 3.8:** History of the determination of the top quark mass $m_t$ [40]: indirect determinations from fits to electroweak observables (open circles) and from direct searches in $e^+e^-$- (solid line) and $p\bar{p}$-collisions (broken line). An indirect bound is also inferred from the $W$-boson width (dot-dashed line). For the direct measurements, the triangles mark the time of initial evidence, discovery claim and latest update available to the author. Both CDF (upward triangles) and DØ (downward triangles) are shown. The crossed boxes show the up to date world averages with respect to the years they were published.

The search for the top quark finally succeeded when both CDF [41] and DØ [42] presented a first evidence for top in 1994. Only one year later, both experiments claimed the discovery, reporting top masses of $m_t = 176 \pm 8(\text{stat.}) \pm 10(\text{sys.})$ GeV (CDF [23]) and $m_t = 199^{+19}_{-21}(\text{stat.}) \pm 22(\text{sys.})$ GeV (DØ [24]). Since the discovery a lot of efford has gone into the measurement of the top quark mass, leading to a current world avarage of $m_t = (173.1 \pm 1.3)$GeV [10].

### 3.3.2 Motivations for a high precision top mass measurement

The top quark mass is an important parameter in the theoretical calculations of electroweak observables. Knowing these will not only allow for consistency tests of the standard model, but also to constrain the expected Higgs-mass $m_H$ and increase sensitivity to physics beyond the standard model.

The most important influence of the top mass on electroweak observables arises from the first order quantum corrections on heavy gauge boson masses $m_W$ and $m_Z$. The mass $m_W$ of the $W$-boson can be expressed via the electroweak mixing angle (Weinberg angle) $\theta_W$ [43]:

$$m_W = \left(\frac{\pi\alpha}{\sqrt{2}G_F}\right)^{1/2} \frac{1}{\sin\theta_W} \cdot \left(1 + \frac{\Delta r}{2}\right) \tag{3.17}$$

where $\alpha \equiv \alpha_{\text{QED}}$ is the fine structure constant, $G_F$ is the Fermi constant and $\Delta r$ represents the quantum corrections. Squaring eq. (3.17) and assuming small corrections $\Delta r$, one can write the Taylor expansion which is a more common form of eq. (3.17):

$$m_W^2 = \frac{\pi\alpha}{\sqrt{2}G_F} \cdot \frac{1}{\sin^2\theta_W} \cdot (1 + \Delta r) \tag{3.18}$$

Contributions to $\Delta r$ arise i.a. from one loop diagrams to the heavy gauge boson masses as shown in Figure 3.9.

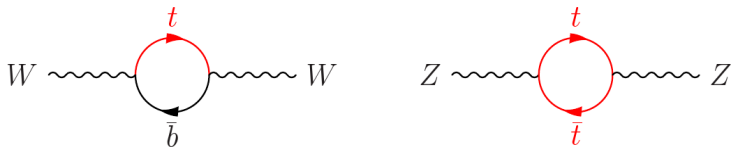


**Figure 3.9:** One loop corrections to the $W$- and $Z$-boson masses containing virtual top quark contributions.

The magnitude of $(\Delta r)_{\text{top}}$ is proportional to the mass of the top quark squared [30]:

$$(\Delta r)_{\text{top}} \approx -\frac{3G_F}{8\sqrt{2}\pi^2 \tan^2\theta_W} m_t^2 \,, \tag{3.19}$$

which demonstrates the significance of this correction. Before the direct observation of top quarks the probing of $(\Delta r)_{\text{top}}$ using data from electroweak fits was used to indirectly infer the top quark mass as shown in Figure 3.8. With the top quark discovered, a precise measurement of $m_t$ will add a new parameter to electroweak fits and thereby a large gain on the precision on the other parameters.

The one loop correction $\Delta r$ is also depending on the Higgs-boson mass. The contributing diagrams are shown in Figure 3.10.
Here, the magnitude is given by [30]:

$$(\Delta r)_{\text{Higgs}} \approx \frac{3G_F m_W^2}{8\sqrt{2}\pi^2} \left(\ln\frac{m_H^2}{m_Z^2} - \frac{5}{6}\right) . \tag{3.20}$$

The Higgs contribution is only logarithmic in $m_H$ and therefore less strong than the top quark contribution which is quadratic in $m_t$. Nevertheless, a precise knowledge of both $m_W$ and $m_t$ allows to infer the Higgs-boson mass from standard model fits to electroweak precision data. The best constrains on $m_H$ are obtained


**Figure 3.10:** One loop corrections to the $W$- and $Z$-boson masses containing virtual Higgs boson contributions.

using high-$Q^2$ reactions from various experiments and applying a $\chi^2$ minimization fit. These analyses have been performed extensively by the LEP-, Tevatron- and SLD[7]-Electroweak Working Groups and are described in detail in [44]. Figure 3.11 shows the value of $\Delta\chi^2 \equiv \chi^2 - \chi^2_{\text{min}}$ as a function of $m_H$ obtained by these groups. Results from direct searches for the Higgs boson at LEP [45] are also shown, presenting a lower limit for $m_H$ of 114.4 GeV at the 95% confidence level. A recent result the TEVNPH[8] Working Group also excludes Higgs masses between 160 GeV and 170 GeV [46].

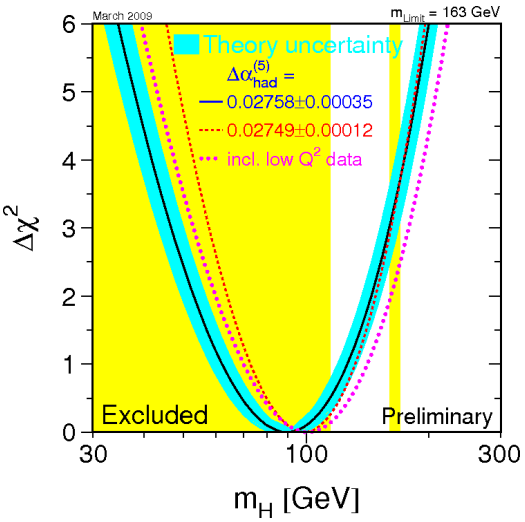


**Figure 3.11:** $\Delta\chi^2 \equiv \chi^2 - \chi^2_{\text{min}}$ vs. $m_H$ [44]. The blue line is the result of a fit using all high-$Q^2$ data including the theory error band resulting from missing corrections in higher order. The dotted line also includes data from low-$Q^2$ reactions. The broken line uses a different evaluation of $\alpha_S(m_Z^2)$. The yellow region on the left is an exclusion area from direct Higgs searches at LEP [45] and the yellow band on the right an exclusion area obtained recently by the TEVNPH Working Group [46].

According to the $\Delta\chi^2$ blueband a Higgs boson mass of $m_H \approx 90$ GeV is preferred which is excluded by direct searches. This might be taken as an indication that $m_H$ is indeed small but a precise prediction does not hold yet due to still inadequate standard model fits, but it might also be a hint for the existence of phenomena beyond the standard model that have not yet been taken into account.

Such a possible scenario is e.g. the minimal supersymmetric extension of the standard model (MSSM). Figure 3.12 shows the isolines for possible Higgs-boson masses for standard model as well as MSSM predictions in the correlation-plane of the two parameters $m_W$ and $m_t$. The ellipses of confidence level (CL) for the determination of these parameters are also shown for 68 %, 95 % and 95.7 % CL. It is obvious that the up to date precision indicates that a MSSM solution is possible. Yet, it is extremely important to further tighten the confidence on the standard model parameters and especially on the top quark mass to further consolidate the predictions.

[7] **S**tanford **L**inear **D**etector
[8] Tevatron New Phenomena and Higgs Working Group

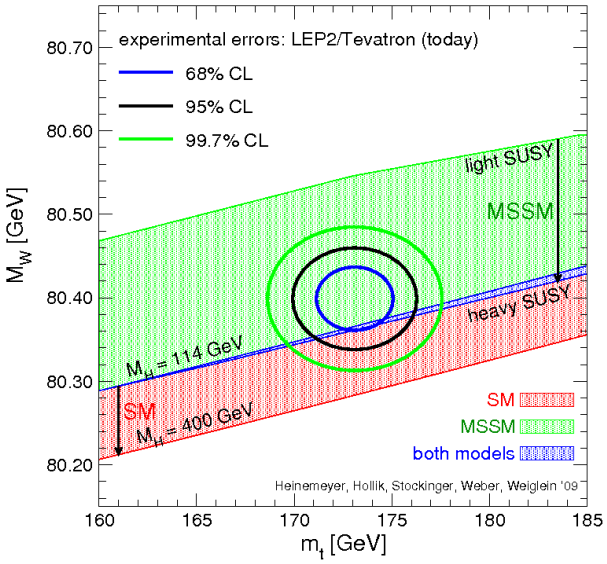


**Figure 3.12:** Comparison of SM and MSSM Higgs-mass solutions in the $m_W$-$m_t$ plane including up to date LEP and Tevatron precisions on these parameters. Result as taken from [47, 48] including two loop corrections [33].

## 3.4 Techniques to measure the top quark mass

This section presents strategies for the determination of $m_t$ as they are indicated for ATLAS and have been used at the Tevatron. The methods are discussed briefly and possible sources of systematic uncertainties are discussed.

### 3.4.1 Invariant mass of the $t\bar{t}$ decay products

A very mainstream method to measure a particles mass from its decay products is to simply calculate the invariant mass of the products. One has to keep in mind though that one has a lot of combinatorial possibilities to assemble these objects, which is basicly due to the fact that two top quarks are involved in the decay. Therefore, an event-by-event $\chi^2$-fit is applied to find the best combination. Eq. (3.21) shows a representation for $\chi^2$ in the semileptonic decay channel.

$$\begin{aligned}\chi^2 \;=\; & \sum_{i=\ell,4\text{ jets}} \frac{(\hat{p}_\perp^{\,i} - p_{\mathrm{j},\perp}^{\,i})^2}{\sigma_i^2} + \sum_j \frac{(\hat{p}_{\mathrm{j},\perp}^{\,UE} - p_\perp^{\,UE})^2}{\sigma_j^2} \\ & + \frac{(m_{\mathrm{jj}} - m_W^{PDG})^2}{\sigma_W^2} + \frac{(m_{\ell\nu} - m_W^{PDG})^2}{\sigma_W^2} + \frac{(m_{b\mathrm{jj}} - m_t^{\mathrm{fit}})^2}{\sigma_t^2} + \frac{(m_{b\ell\nu} - m_t^{\mathrm{fit}})^2}{\sigma_t^2}\end{aligned} \tag{3.21}$$

The first two sums in the first row of eq. (3.21) compare the measurement ('hat') and fit for each reconstructed object, i.e. the lepton and four jets in the first sum and the underlying event in the second sum. The second row starts with two sums constraining combination for the $W$–mass and to the value obtained by the Particle Data Group [11]. The last two terms constrain the reconstructed top quark mass itself, the parameter $m_t^{\mathrm{fit}}$ is the respective top quark mass fittet for the resulting $\chi^2$. The resolutions $\sigma_i$ are all obtained from MonteCarlo. The final value for the top quark mass is then obtained by an extrapolation $m_t(\chi^2) \rightarrow m_t(\chi^2 = 0)$, as shown in Figure 3.13.
This method has been investigated in detail for a possible application to ATLAS [49]. A special focus was laid on the investigation of systematic uncertainties, since statistical uncertainties are not expected to be an issue due to the large number of $t\bar{t}$ pairs will be produced. The main uncertainty of this method is due to

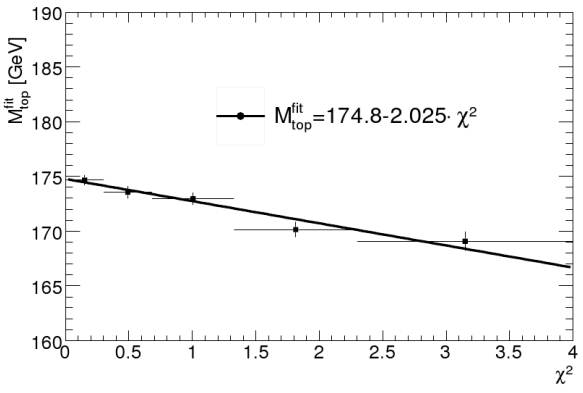


**Figure 3.13:** Estimate of the top quark mass as a function of $\chi^2$ for the ATLAS experiment. The points are fitted by a linear function to extract $m_t = m_t(\chi^2 = 0)$. The input top quark mass was $m_t^{\text{input}} = 175$ GeV [49].

measurement of the jet energy which plays an important role in this measurement. This uncertainty reflects in the so-called jet energy scale (JES) which is a mapping function to count back from the reconstructed jet energy to the parton level energy. Keeping control of the jet energy scale uncertainties is an important point in top quark mass measurements and is therefore a topic in further developments on techniques to measure $m_t$, of which the most important are described in the following.

### 3.4.2 The template method

The previously discussed method can be expanded using MonteCarlo simulations of $t\bar{t}$ events at different top quark masses. For each of these samples as well as for additional background samples the distributions of reconstructed top quark masses obtained from the $\chi^2$ fit can be used as templates for a comparison to real data [50]. The method benefits from the additional possibilty to fit the dijet $W$-boson mass $m_{\text{jj}}$ which can also be used to generate templates, allowing to put a constraint on the jet energy scale and thereby reducing the respective uncertainty. This method has been used by the CDF experiment and is still under investigation to be applied at ATLAS; examples of templates used by CDF are shown in Figure 3.14. The comparison of templates and reconstructed mass spectrum is done using an unbinned likelihood fit. The likelihood contains free parameters for the number of signal- and background events, the top quark mass and the jet energy scale. The likelihood of each sample is given by:

$$\mathcal{L}_{\text{sample}} = \mathcal{L}_{m_t} \times \mathcal{L}_{m_{\text{jj}}} \times \mathcal{L}_{\text{bkg}} \times \mathcal{L}_{\text{nev}} \quad , \tag{3.22}$$

where $\mathcal{L}_{m_t}$ contains information about the top quark mass, $\mathcal{L}_{m_{\text{jj}}}$ contains information about the dijet mass and therefore the jet energy scale, $\mathcal{L}_{\text{bkg}}$ represents the background and $\mathcal{L}_{\text{nev}}$ contains information of the number of signal- and background events in the correlated $m_t$ and $m_{\text{jj}}$ samples.

The advantage of the method is the explicit in-situ jet calibration and thus the possibility to measure the jet energy scale. An additional feature is the possibility to measure the signal fraction of the investigated sample. These features make the measurement of the top quark mass more powerful than the previously described $\chi^2$ alone. However, several systematic uncertainties remain which are common to both methods. The most important effects come from combinatorial background in the reconstruction of $m_t$ and $m_{\text{jj}}$ which due not only affect the result on the top quark mass but also on the jet energy scale. Additional effects arise from the energy response of the $b$-jet in the top quark decay which enters in the determination

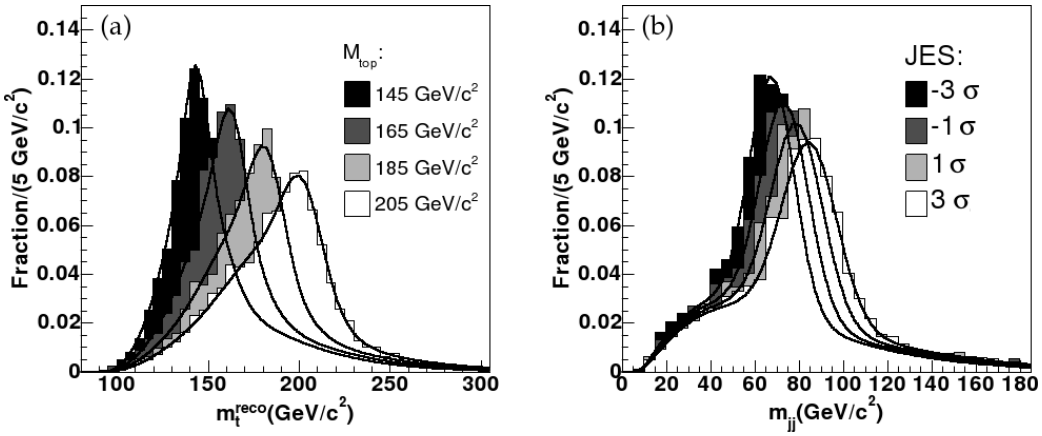


**Figure 3.14:** Examples of templates of top quark mass distributions (a) and dijet mass distributions (b) as used by the CDF collaboration. Both the top quark mass and the jet energy scale are shown in several variations. The underlying top quark mass in (b) is $m_t = 180$ GeV [50].

of $m_t$ as seen in eq. (3.21). These effects are based on the energy measurement of the respective $b$-jet as well as the imperfect knowledge of fragmentation which are both not covered within the template estimates. Another category is the presence of initial and final state gluon radiation (ISR/FSR), which also complicates the measurement due to the presence of additional jets as well as changed kinematics.

### 3.4.3 The Matrix Element (ME) method

The Matrix Element method uses a likelihood technique based on a per-event probability density to observe an event with certain measurement variables $x$. It has successfully been applied to both DØ [51] and CDF [52] and is currently under investigation to be applied to ATLAS. The probability is constructed from the matrix element of the considered processes contributing to that event and, in case of $t\bar{t}$ events, is depending on the top quark mass:

$$P_{\text{event}} = A(x)\left[C_S \cdot P_{\text{sig}}(x, m_t, k_{\text{JES}}) + (1 - C_S) P_{\text{bkg}}(x, k_{\text{JES}})\right] \quad . \tag{3.23}$$

where $P_{\text{sig}} \equiv P_{t\bar{t}}$ is the propability that the observed event is a $t\bar{t}$ signal event, $P_{\text{bkg}}$ the propability that it is background, $m_t$ is the top quark mass and $k_{\text{JES}}$ is the jet energy scale. The factor $A(x)$ accounts is simply an acceptance factor counting for geometry and efficiencies. $C_S$ is the signal fraction contributing to all events and has to be determined from data. The signal and background propabilities are calculated by integrating over all possible parton states leading to the set of variables $x$. For $t\bar{t}$ signals this probability can be written as:

$$P_{t\bar{t}} = \frac{1}{\sigma_{t\bar{t}}(m_t)} \int d^n\sigma(x_{\text{part}}, m_t)\, dq_1 dq_2 f(q_1) f(q_2)\, W(x, x_{\text{part}}) \quad . \tag{3.24}$$

The integral $d^n\sigma(x_{\text{MC}}, m_t)$ runs over the processes phase space and cross section which contains the matrix element squared, $f(q_1)$ and $f(q_2)$ are the parton density functions of the corresponding quarks and $W(x, x_{\text{MC}})$ is a so-called transfer function which maps parton level variables $x_{\text{part}}$ to the measured detector variables $x$.

The final likelihood can be written as:

$$\begin{aligned} \ln L(m_t, k_{\mathrm{JES}}) &= \sum_{i=1}^{N} \ln \left( C_{t\bar{t}} P_{t\bar{t}}(x_i, m_t, k_{\mathrm{JES}}) + C_{\mathrm{bkg}} P_{\mathrm{bkg}}(x, k_{\mathrm{JES}}) \right) \\ &- N \int A(x) \left[ C_{t\bar{t}} P_{t\bar{t}}(x_i, m_t, k_{\mathrm{JES}}) + C_{\mathrm{bkg}} P_{\mathrm{bkg}}(x, k_{\mathrm{JES}}) \right] dx \end{aligned} \tag{3.25}$$

The most likely topquark mass is then obtained by finding the maximum likelihood $L_{\max}$ in the investigated $N$-event sample. As one can see, the Likelihood simultaneously determines $m_t$, the jet energy scale and the signal fraction similar as in the template method.

The advantage of this method is that since it is event-by-event based, results can be obtained even on a sample with extremely low statistics. A drawback however is that the method suffers from large systematic uncertainties coming from theory, e.g. the uncertainties on the matrix elements and PDFs, as well as from MonteCarlo and detector simulations, e.g. the physics and detector modeling in the transfer functions. Apart from that, this method encounters similar systematic uncertainties to the template method with respect to combinatorics, $b$-jet properties and initial and final state radiation.

### 3.4.4 The decay length method

An alternative method to measure the top quark mass is to infer the mean transverse decay length of $B$-hadrons from the top quark decay to the mass of the top quark. This technique is referred to as the decay length method and is the main focus of this thesis. The method uses the secondary vertices from $b$-jets in preselected $t\bar{t}$ events to measure the transverse flight length of the $B$-hadrons which stem from the $b$-quarks from the top quark decay. Therefore, the methods relies mostly on tracking and vertex finding and hence has complementary uncertainties to the method described previously. Especially the dependance on the jet energy scale is assumed to be negligible which is a strong feature of the method. The decay length method is the main focus of this thesis and is described in detail in chapter 5, where the basic idea, theory and estiamtes for results and uncertainties at the ATLAS experiment are discussed.

## 3.5 Other top quark properties

### 3.5.1 The charge of the top quark

As already mentioned the electrical charge of the top-quark is expected to be $Q_t = 2/3\ e_0$ as the top rows up in the series of up-type quarks. In principle, the charge can be determined by the ratio

$$R = \frac{\sigma(e^+e^- \to \mathrm{Hadrons})}{\sigma(e^+e^- \to \mu^+\mu^-)} \tag{3.26}$$

at the top quark production threshold using an $e^+e^-$ collider. Since up to now the top quark has only been observed in $p\bar{p}$ collisions and no $e^+e^-$ colliders with a high enough center-of-mass energy exist, it is very difficult to directly measure the charge. First attempts on this have been undergone at the Tevatron by measuring the sum of charges in top events on each side ($t$ and $\bar{t}$) of the event separately.

Assuming a standard model decay of the top into a $W$-boson and a $b$-quark as described in section 3.2.4, it is possible to interpret the results as either standard model conform with $Q_t = +2/3\ e_0$ or as exotic $Q_t = -4/3\ e_0$. This can be understood if one does the gedankenexperiment of assuming the top quark to decay via $t \to W^- + b$ instead of $t \to W^+ + b$ (vice versa for the antitop quark). Up to now, the DØ experiment excludes the exotic solution at the 92% confidence level [53], making the top quark a standard model particle.

### 3.5.2 The spin of the top quark

The top quark is expected to have half-integral spin due to its nature as a quark. Since the top quark does not hadronize because of its short lifetime as described in section 3.2.4, the top quarks spin information will be carried on into its decay products, providing a powerful possibility to test the top quarks production and decay mechanisms. In the special case of $t\bar{t}$ events at hadron colliders, one finds that the top and antitop spins are highly correlated [54]. This allows to probe the production asymmetry $A$ as given by eq. (3.27), which is an appropriate observable to test the standard model conformity of the top quark production:

$$A = \frac{\sigma_{\uparrow\uparrow} + \sigma_{\downarrow\downarrow} - \sigma_{\uparrow\downarrow} - \sigma_{\downarrow\uparrow}}{\sigma_{\uparrow\uparrow} + \sigma_{\downarrow\downarrow} + \sigma_{\uparrow\downarrow} + \sigma_{\downarrow\uparrow}} \quad . \tag{3.27}$$

Here, $\sigma_{(\uparrow/\downarrow)(\uparrow/\downarrow)}$ is the cross section for a $t\bar{t}$ pair with spins up or down with respect to the selected quantisation axis. Another possibility to test standard model predictions in top quark decays is the measurement of the $W$-boson helicity. As discussed in section 3.1.2, one expects the $W$ from top decays to be not right handed as the top quark is a particle. Since the top quark is heavy, mixed helicity states leading to longitudinal polarization are also allowed, but the simple right-handed solution should be strongly suppressed. The three helicity states $F_0$ (longitudinal), $F_R$ (righthanded) and $F_L$ (lefthanded) and be extracted form the angular distribution of $\Psi$:

$$\frac{1}{N}\frac{dN}{d\cos\Psi} = \frac{3}{2}\left[F_0\left(\frac{\sin\Psi}{\sqrt{2}}\right)^2 + F_L\left(\frac{1-\cos\Psi}{2}\right)^2 + F_R\left(\frac{1+\cos\Psi}{2}\right)^2\right] \quad , \tag{3.28}$$

where $\Psi$ is the angle between the $W$-direction in the top rest frame and the direction of the final lepton from the $W$-decay. The expected standard model values for the helicity states and the asymmetry are summarized in Table 3.6.

**Table 3.6:** Standard model predictions for the helicity of $W^+$-bosons emerging from top quarks [55].

| $F_0$ | $F_L$ | $F_R$ | $A$ |
|---|---|---|---|
| 0.695 | 0.304 | 0.001 | 0.422 |

To measure the helicity parameters $F_i$ as well as the production asymmetry $A$ the full event has to be reconstructed. This is obviously a challenging task, but it has been demonstrated that at ATLAS a precision of 1% to 5% is achievable [55].

# Chapter 4

# The data, analysis framework and selection of physics objects for ATLAS top quark analyses

In the past years many preparational studies have been done to provide the best possible understanding of all the ATLAS experiments concerns. These involve theory, detector development and infrastructure as well as computing tests and analysis preparations. The latter have been studied in the context of the so–called **C**omputing **S**ystem **C**ommissioning (CSC) efforts [56] which had two main goals:

1. to perform an operational test of the ATLAS software system and running the full analysis chain. This main task was the origin of the expression "CSC", as it tested the simulation and reconstruction on local computing system as well as world-wide grid facilities.

2. to estimate ATLAS performance and analysis capabilities before initial operation. This was accomplished by applying a fully simulated detector output which is assumed to represent an ideal, fully operational detector.

3. to define a common set of observables for each physics group that will be the same in both simulation and measurement data.

The main focus of these studies with respect to the top quark mass was the estimation of systematic uncertainties, as statistical uncertainties will be negligible in the long term of LHC as was shown in section 3.2.3. Nevertheless, due to the limitation of available simulation data statistics indeed is a concern as will be discussed later.

In order to provide a fundamental basis for all investigations in the top quark group, a set of standards to meet in the individual analyses had been classified. These standards involve:

- usage of datasets and cross sections as provided by the group,
- usage of common data files that had been created with the TopView analysis framework (release 00-12-14-03),
- usage of the same physics objects,
- usage of a commonly defined event selection by all subgroups. Any deviation of this selection should be motivated and keept as small as possible.

The studies concerning the decay length method for the measurement of the top quark mass presented in this thesis have been accomplished in the context of the CSC efforts. Therefore, the standards defined for CSC have largely been followed throughout the thesis. This chapter describes the simulated data, the physics objects and event selection as well as the basic contents of TopView that have been used for the analysis. An additional content of TopView that has been developed especially for this study and was successfully implemented as a standard in TopView will be described separately in section 4.2.2.

## 4.1 Investigated data

As already mentioned the analysis of simulated physics data was one of the main tasks in the course of the CSC studies. Various physics processes have been simulated using a multitude of event generators. The special subset for the investigation of top quark physics that have been used in this thesis will be described in this section. Each used generator has been chosen by the ATLAS physicists community due to its power in modeling the respective physics aspects of a sample [57]. All datasets discussed here represent LHC proton-proton collisions with a center of mass energy of $\sqrt{s}$ =14 TeV. The generated physics processes have been fully simulated using Geant4 ATLAS detector simulation and reconstruction. Underlying events are present in all datasets, however pile-up is not included.

The tables in this section summarize the relevant datasets for the studies presented here. Each sample is listed with the identification number, physics signature, amount of available events and the top quark working group recommendations for the cross sections. As most of the cross sections quoted below were calculated in LO precision, the correction factors (so-called $k$-factors) to rescale the cross sections to an approximate NLO value

$$\sigma_{\text{corr}} = k \cdot \sigma \tag{4.1}$$

are quoted as well. In case the tables quote $k = 1$ the corresponding cross section was calculated to a NLO precision.

The number of events shown in the tables represent the actual number of events found in the data files. Each sample therefore represents its own luminosity content $\mathcal{L}_{\text{evt}}$ which can easily be calculated via the well-known relation

$$\mathcal{L}_{\text{evt}} = \frac{N_{\text{evt}}}{\sigma} \tag{4.2}$$

from the number of events $N_{\text{evt}}$ and the cross section $\sigma$ of the respective process. To obtain the number of events for a certain luminosity $\mathcal{L}_{\text{target}}$, a scaling factor $s$ is applied that is defined by

$$s = \frac{N_{\text{target}}}{N_{\text{evt}}} = \frac{\mathcal{L}_{\text{target}}}{\mathcal{L}_{\text{evt}}} = \frac{\mathcal{L}_{\text{target}}}{N_{\text{evt}}} \cdot \sigma\,. \tag{4.3}$$

The scaling of events to obtain a certain statistics brings up the issue of scaling the uncertainties related to the respective amount of statistics. This holds especially for the treatment of statistical uncertainties, but systematic uncertainties are also affected as will become clear later on.

Several cases have to be taken into account here:

- The statistical uncertainties related to the actual amount of events available in a data sample.
  This number is obtained from the analysis before any scaling is done, hence it represents the actual statistical significance of that sample. This becomes important especially in the case where a too large error affects the functionality of the analysis.

- The statistical uncertainty of the scaled sample.
  This uncertainty reflects the statistical power of the investigated luminosity to which the sample was scaled. It is obtained by calculating the analysis results on the sample after the scaling was done, which is a useful technique to provide an estimate of what can be expected in the actual experiment. One has to keep in mind though that using only scaled uncertainties might lead to false conclusions in case that the unscaled uncertainties are indicating that the sample does not have a significant statistical power. In this case, the scaled uncertainty might be small and resulting inconsistencies may be mistaken as systematic errors. Also note that in some cases the actual sample containes a larger integrated luminosity than the scaled one, in which case the scaled uncertainty will increase.

- Systematic errors that do not depend on the size of the sample.
  As just mentioned these errors have to be identified clearly to be systematic, i.e. not depending on the investigated statistics. In this case the corresponding uncertainty does not depend on the scaling.

### 4.1.1 Negative weights and the subtraction method in NLO event generators

Due to the high energy regime of the LHC the simulation of physics is required at the precision of next-to-leading order predictions. However the generation of such events is a challeging task due to the divergencies appearing at higher order in pertubative quantum field theories. A solution to this is provided by the introduction of 'counter events' with negative weights which reflect the subtraction terms in the pertubation series that cancel these divergencies. This technique is therefore called the subtraction method. Considering the distributions of observables the counter events contribute with equal but opposite weight to all distributions. However one has to keep in mind that while in NLO computations only the sum of positive and negative contributions converges, the positive and negative weights in the subtraction method are separately finite [58]. The first choise next-to-leading order generator using negative weights is called MC@NLO [58–60], which has been used for the calculation of matrix elements of some of the datasets discussed in the following. Approximately 13% of all events in MC@NLO have negative weights ($w = -1 \equiv w_-$) while the rest has positive weights ($w = +1 \equiv w_+$). For convenience, the number of events found in the files as given by $w_+ + w_-$ will be called the 'total number' of events $w_{\text{tot}}$ in the following, while the number of events contributing to the distributions and to the calculation of the luminosity (eq. (4.2)) as given by $w_+ - w_-$ will be called the 'effective number' of events $w_{\text{eff}}$.

### 4.1.2 $t\bar{t}$ signal samples

The matrix elements of the top pair production samples have been provided by MC@NLO, version 3.1. For the parton densities the CTEQ6M parametrization has been used [29]. The hadronization has been simulated by HERWIG [61, 62] and the underlying event by JIMMY [63]. No cuts on the generator levels are applied except for the fact that the fully hadronic $t\bar{t}$ channel is separated from the semi- and dilepton channel in their own self-contained sample. The combined semi- and dilepton sample has been produced assuming three different top quark masses which have been used for several mass measurement techniques including the decay length method. The so-called "central sample" $m_t = 175$ GeV has been produced in the full statistics representing an integrated luminosity of 1 fb$^{-1}$ which is approximately 450000 effective events, while the off-center masses of $m_t = 160$ GeV and $m_t = 190$ GeV contain only about 73000 effective events. In the course of this thesis, a subsample of the central mass sample containing about 660 pb$^{-1}$ (approximately 330000 effective events) has been used. The sample for the fully hadronic channel has also been produced by MC@NLO, however only 71000 effective events with $m_t = 175$ GeV have been simulated since this sample was indicated for cross sections studies and as background for the previously discussed samples rather than mass measurements for the reasons discussed in section 3.2.4.

**Table 4.1:** $t\bar{t}$ signal samples used throughout this thesis [49]. All cross sections are calcuated using the branching fractions presented in Table 3.4. For the combined semi- and dilepton channel the total sum of the cross section is quoted. Note that although the cross section is usually depending on the top quark mass, the same numerical value based on $m_t = 175$ GeV is used for all samples.

| Dataset | physics process | # events | $k$-factor | $\sigma$ [pb] |
|---|---|---|---|---|
| MC@NLO : fully simulated $t\bar{t}$ events | | | | |
| 5200 | $t\bar{t}$ $(m_t = 175$ GeV) | $w_+$ : 389744 | 1.00 | 455.17 |
| | $\ell + j$ and $2\ell$ decay channels | $w_-$ : 60256 | | |
| 6203 | $t\bar{t}$ $(m_t = 160$ GeV) | $w_+$ : 85389 | 1.00 | 455.17 |
| | $\ell + j$ and $2\ell$ decay channels | $w_-$ : 13706 | | |
| 6204 | $t\bar{t}$ $(m_t = 190$ GeV) | $w_+$ : 86586 | 1.00 | 455.17 |
| | $\ell + j$ and $2\ell$ decay channels | $w_-$ : 13414 | | |
| 5204 | $t\bar{t}$ $(m_t = 175$ GeV) | $w_+$ : 84275 | 1.00 | 377.83 |
| | fully hadronic decay channel | $w_-$ : 12925 | | |

### 4.1.3 Single top quark signal samples

The single top signal samples have been produced using an AcerMC matrix element [64] and hadronization is provided by PYTHIA [65, 66]. As for the $t\bar{t}$ signal samples the CTEQ6M parametrization has been used to describe the parton density function. The s-channel and associated production $Wt$ have been calculated at leading order accuracy, while the t-channel has been generated in NLO to include the gluon fusion as shown in Figure 3.5 (a). The t-channel data therefore has negative weights; the subtraction method used here is described in [67]. Generator cuts have been applied to the s-channel and t-channel production to force the $W$-boson from the top quark to decay leptonically. In the case of $Wt$ production, either the $W$-boson from the top quark or the associated $W$-boson are forced to decay leptonically; the dilepton mode is not included. This enables the usage of the trigger for analyses in the single top sector and at the same time makes the samples a background for $t\bar{t}$ analyses in the semileptonic channel due to the similar topology. The cross sections for the samples of single top production listed in 4.2 differ from those in Table 3.2 as they include the respective branching fractions of the investigated channels.

**Table 4.2:** Single top quark signal samples used in this thesis [49]. The quoted cross sections already contain the $k$-factors.

| Dataset | physics process | # events | $k$-factor | $\sigma$ [pb] |
|---|---|---|---|---|
| AcerMC + PYTHIA : fully simulated single top events ($m_t = 175$ GeV) | | | | |
| 5500 | associated production $Wt$<br>$\ell + j$ decay channel | 15200 | 1.14 | 29.07 |
| 5501 | s-channel<br>$\ell + j$ decay channel | 9750 | 1.5 | 3.45 |
| 5502 | $Wg$-fusion/t-channel<br>$\ell + j$ decay channel | $w_+$ : 17386<br>$w_-$ : 1114 | 0.98 | 79.674 |

### 4.1.4 $W$+jets Background

As discussed in section 3.2.4 the semileptonic $t\bar{t}$ decay channel is characterized by four high-$p_\perp$ jets, one lepton and its associated missing energy. The main physics background apart from the single top signature for this channel is therefore the leptonic decay of $W$-bosons accompanied by final state partons that create jets. This topology is referred to as $W$+jets and is divided into several subsets listed in Table 4.3. All samples have been generated using ALPGEN matrix elements [68]. For the parton showering and the underlying event HERWIG and JIMMY have been used. To match the calculations of shower processes and matrix elements, the MLM-matching algorithm [69] has been applied during the generation of events.

Three basic characteristics were considered in the input matrix element of the $W$+jets samples:

- $W + n$ gluons, where $n$ is an integer between 2 and 5. Each gluon that is produced is handed to the shower algorithm and creates jets, and the $W$-boson is forced by a generator cut to decay leptonically. The signature of these samples is therefore the presence of one lepton, $\not\!\!E_\perp$ and two to five jets which are light jets as well as heavy jets, although the latter are not modeled accurately by the shower algorithm, since HERWIG uses a showering model with massless quarks [61]. The samples are referred to as the $W$+jets sample.

- $W + b\bar{b} + n$ gluons. Here, the number of final state gluons $n$ runs from 0 to 3 while one additional gluon is forced to decay into a pair of $b$-quarks and the $W$-boson is forced to decay leptonically. These samples provide a $b$-jet background which is more accurate than the heavy quarks in the $W$+jets sample, as the bottom quarks are already contained in the matrix element and therefore have $m_b \neq 0$ GeV. These samples are referred to shortly as $Wbb$.

- $W + c\bar{c} + n$ gluons. This signature is analog to the $W + b\bar{b}$ samples, and it is therefore referred to as $Wcc$.

Example representations of Feynman diagrams of $W$+jets events as described above are shown in Figure 4.1.

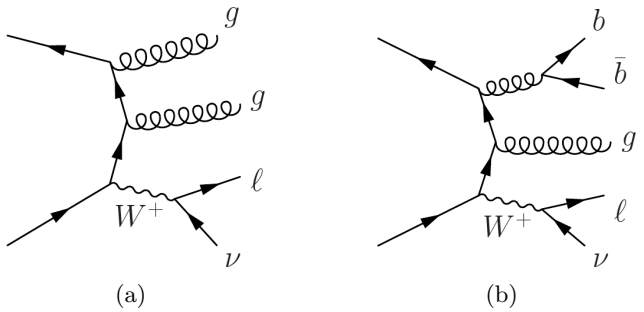


**Figure 4.1:** Examples of $W$+jets events: (a) $W + 2$ gluons, (b) $W + b\bar{b} + 1$ gluon.

The $W$+jets samples contain a certain overlap with the $Wbb$ and $Wcc$ samples which can be demonstrated using Figure 4.1. Assuming that the shower algorithm converts the first gluon into a pair of $b$-quarks, one finds that the event actually fakes the signature of $W + b\bar{b} + 1$ gluon which is shown in Figure 4.1 (b). This feature leads to a double counting of events as well as to a mixture of massless and massive $b$-quarks if the samples are used in combination. Avoiding these effects is a non-trivial task since the production of heavy flavored jets can not be turned of a priori in the shower algorithms. Dedicated strategies for the treatment of this feature are still under discussion within the top quark working group as the $W$+jets signature is an important background and needs to be described correctly. In the course of this thesis the influence of the overlap will be estimated by comparing the combined samples and the $W$+jets with $Wbb$ and $Wcc$ separately, see sections 4.4.6 and 5.2.3 for details.

**Table 4.3:** Samples containing leptonic $W + n$ partons used as background to $t\bar{t}$ [49]. The quoted cross sections already contain the $k$-factors if $k \neq 1$.

| Dataset | physics process | # events | $k$-factor | $\sigma$ [pb] |
|---|---|---|---|---|
| ALPGEN + HERWIG + JIMMY : leptonic $W + n$ gluons | | | | |
| 8240 | $W \to e\nu$ + 2 partons | 21950 | 1.15 | 246.12 |
| 8241 | $W \to e\nu$ + 3 partons | 11250 | 1.15 | 142.52 |
| 8242 | $W \to e\nu$ + 4 partons | 6000 | 1.15 | 61.71 |
| 8243 | $W \to e\nu$ + 5 partons | 4950 | 1.15 | 25.67 |
| 8244 | $W \to \mu\nu$ + 2 partons | 7000 | 1.15 | 18.79 |
| 8245 | $W \to \mu\nu$ + 3 partons | 12500 | 1.15 | 74.40 |
| 8246 | $W \to \mu\nu$ + 4 partons | 3200 | 1.15 | 41.41 |
| 8247 | $W \to \mu\nu$ + 5 partons | 2750 | 1.15 | 23.21 |
| 8248 | $W \to \tau\nu$ + 2 partons | 19700 | 1.15 | 100.86 |
| 8249 | $W \to \tau\nu$ + 3 partons | 13000 | 1.15 | 100.21 |
| 8250 | $W \to \tau\nu$ + 4 partons | 5750 | 1.15 | 52.77 |
| 8251 | $W \to \tau\nu$ + 5 partons | 550 | 1.15 | 23.93 |
| **total** | | **108600** | | **910.6** |
| ALPGEN + HERWIG + JIMMY : leptonic $W + bb + n$ gluons | | | | |
| 6280 | $W \to \ell\nu + bb + 0$ partons | 6250 | 2.57 | 16.08 |
| 6281 | $W \to \ell\nu + bb + 1$ partons | 7200 | 2.57 | 17.91 |
| 6282 | $W \to \ell\nu + bb + 2$ partons | 4000 | 2.57 | 10.07 |
| 6283 | $W \to \ell\nu + bb + 3$ partons | 3000 | 2.57 | 7.12 |
| **total** | | **20450** | | **51.18** |
| ALPGEN + HERWIG + JIMMY : leptonic $W + cc + n$ gluons | | | | |
| 6284 | $W \to \ell\nu + cc + 0$ partons | 7000 | 1.00 | 6.72 |
| 6285 | $W \to \ell\nu + cc + 1$ partons | 3500 | 1.00 | 7.49 |
| 6286 | $W \to \ell\nu + cc + 2$ partons | 4500 | 1.00 | 4.36 |
| 6287 | $W \to \ell\nu + cc + 3$ partons | 2500 | 1.00 | 2.45 |
| **total** | | **17500** | | **21.02** |

### 4.1.5 Samples for the investigation of ISR/FSR systematic uncertainties

Gluon bremsstrahlung from initial and final state partons, also referred to as initial- (ISR) and final state radiation (FSR), has a major impact on the measurement of the top quark mass. The uncertainties arise from two effects:

- higher multiplicity of jets due to additional gluons which affect the even selection and combinatorics in the reconstruction,
- change of the kinematics of all particles involved in the hard process.

The amount of ISR and FSR is basically determined by the strength of the coupling in strong interactions. To determine the uncertainties arising from ISR and FSR, the default value of $\Lambda_{QCD} = 250$ MeV has therefore been varied in the generation of dedicated $t\bar{t}$ signal samples. Two samples have been created using an AcerMC matix element interfaced with PYTHIA for the hadronization. One of these uses half the default value of $\Lambda_{QCD}$ for ISR and twice the default value for FSR which leads to a lower reconstructed top quark mass using the $\chi^2$ fit method [49] while the other sample goes vice versa. They are therefore referred to as the 'high-mass' and 'low mass' samples. For reference a $t\bar{t}$ signal sample with default $\Lambda_{QCD}$ has also been created with AcerMC and PYTHIA, since a comparison with the MC@NLO datasets is not possible due to the generator differences.

**Table 4.4:** $t\bar{t}$ signal samples with modified $\Lambda_{\mathrm{QCD}}$ for ISR and FSR studies [49].

| Dataset | physics process | # events | $k$-factor | $\sigma$ [pb] |
|---|---|---|---|---|
| AcerMC + PYTHIA : fully simulated $t\bar{t}$ events ($m_t = 175$ GeV) | | | | |
| 5205 | default $\Lambda_{\mathrm{QCD}} = 250$ MeV<br>$\ell + j$ and $2\ell$ decay channels | 150000 | 1.00 | 455.17 |
| 6250 | $2\times\Lambda$(ISR), $0.5\times\Lambda$(FSR), high mass<br>$\ell + j$ and $2\ell$ decay channels | 227105 | 1.00 | 455.17 |
| 6251 | $0.5\times\Lambda$(ISR), $2\times\Lambda$(FSR), low mass<br>$\ell + j$ and $2\ell$ decay channel | 198600 | 1.00 | 455.17 |

## 4.2 ATHENA and TOPVIEW: The ATLAS analysis framework

The software package ATHENA is the offline analysis framework for ATLAS data. It is an enhanced version of the GAUDI-framework that has originally been developed by the LHC-B experiment [70]. The underlying component-based architecture (also called GAUDI) was designed to be applicable to a wide range of physics data-processing. The fact that it is component-based allows for several features:

- Flexibility:
  A wide range of shared components can be developed independently and used if appropriate. For example, a common statistics tool developed within the global framework can be applied to the specific data formats implemented by different experiments but could also be replaced by the certain group.

- Separation of data and algorithms:
  The interface to access a certain data format, e.g. track point data that is obtained in a tracker, is completely separated from the algorithm that fits the track and computes its parameters, which creates an independency between the producer and consumer of the data.

- Run-time optimization:
  In a dedicated run of the analysis where usually not all tools are needed, the respective computational run only needs to process the code required for this analysis.

- Customization:
  Each user of the software can compile its very-own software package and additionally add his own code without destroying or disturbing the rest of the framework.

- Revision control:
  The software can be developed by every member of the collaboration. Therefore, the enhancement of the framework is fast and safe, as every specialized tool can be developed and revised by the respective experts.

The ATHENA-framework makes an extensive use of these features. The software is continuously extended by the members of ATLAS and regular updates are available. ATHENA contains reconstruction algorithms for basic particle objects like electrons or muons as well as for more abstract objects like tracks, jets or missing energy. These reconstruction algorithms are the same for both real data and simulation as the same data formats are used in both approaches.

Each physics subgroup compiles a more customized tool for their respective analysis, e.g. TOPVIEW for top quark physics or SUSYVIEW for super symmetry physics. All these tools are summarized as the EVENTVIEW-tools. These tools are optimized for their respective physics studies in the sense that they take care of the preselection of objects that are used later by the group, thereby making sure that all subgroups investigate the same physics.

The studies presented in this thesis are based on ATHENA version 12.0.7 and TOPVIEW version 00-12-14-03, where the global ATHENA version is represented by the first two numbers and the TOPVIEW (sub-)version is represented by the last numbers. Lately, the "VIEW" tools have been reorganized and therefore renamed into e.g. TOPPHYSTOOLS with version 14 of ATHENA, but the basic content is the same. Details on this will not be discussed here since this thesis is based on the already mentioned versions.

### 4.2.1 Data format and analysis flow

Both data formats and analysis flow steps of the ATLAS experiment have been defined at very early stages in the development of the ATLAS computing model to ensure compatibility at the earliest stage possible [70]. The format of the first data available offline, which has been already referred to as 'raw-data', is the first in a list of data formats that represent different stages in the analysis.

The sequential list of basic data formats is as follows:

- Raw Data (RDO):
  Raw data objects (RDO) are events as provided by the Event Filter (section 2.3). These events arrive in a "byte-stream" format, reflecting the format in which data is delivered from the detector, rather than in an object-oriented representation.

- Event Summary Data (ESD):
  ESD refers to event data written as the output of the reconstruction process. Its content is intended to make access to RDO files unnecessary for most physics applications other than for calibration or re-reconstruction. In contrast to the RDO format, data in the ESD is stored in an object-oriented representation.

- Analysis Object Data (AOD):
  The AOD is a reduced event representation derived from ESD. It contains physics objects and other elements of analysis interest.

- Derived Physics Data (DPD):
  The DPD is an n-tuple-style representation of event data for end-user analysis and histogramming. It has been included in the data flow to consider the standard physics formats suitable for direct analysis and display via standard analysis tools (PAW[1] or ROOT[2] for example), though histogramming, and display will also be possible in the scope of direct AOD analysis.

- Simulated Event Data (SIM):
  SIM refers to a range of data types, beginning with GenEvents provided by MonteCarlo (MC) generators, HIT data from simulation of interactions with the detector and detector response data DIG (digitization). It may also include additional data like pile-up, minimum bias events, or the simulation of cavern background. The output filetype will be analog to the formats of measurement data discussed above. Nevertheless, simulated events are often larger than events from measurement because they usually contain a description of the event as generated by the MonteCarlo and from simulation. This additional information is referred to as "MCTruth" or simply "Truth", which is stored along with the reconstruction data in the respective files.

Each dataset described in section 4.1 has been processed in the so-called full analysis chain which is sketched in Figure 4.2, and was available as either AOD or DPD for the final analysis. In the full chain processing line, the hard process that is generated with MonteCarlo generators and represents the collission process is handed to a detector simulation that is as close to reality as possible. An alternative processing line called AtlFast exists that provides a more time-saving but less accurate detector simulation; it has therefore not been considered for the CSC studies.

[1] **P**hysics **A**nalysis **W**orkstation, http://paw.web.cern.ch/paw/
[2] http://root.cern.ch/

In the course of this thesis the official DPD files for all datasets were used for the analysis, with an exception of the three $t\bar{t}$ signal samples 5200, 6203 and 6204 ($m_t$ =175, 160 and 190 GeV) which had been reprocessed to include additional content which is described in the next section.

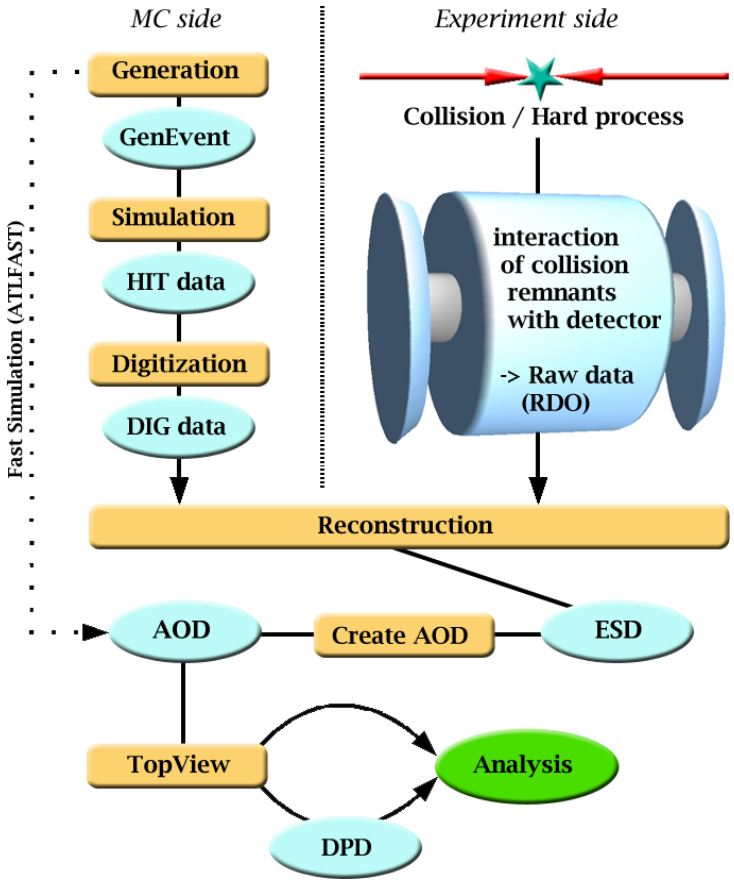


**Figure 4.2:** Scheme of the data flow defined for ATLAS devided in the full chain of MonteCarlo data generation and detector simulation and the data flow of the experimental side. The AtlFast fast simulation line is also indicated. The further processing of AODs after reconstruction is also shown for the specific top quark analysis (TopView).

### 4.2.2 The TopView analysis package

TopView [71] is an analysis package dedicated to the analysis of top quark physics which is embedded in the Athena framework. It is designed to run on AOD datafiles and is capable of doing full physics analysis on the AOD level as well as creating DPD files that can be analyzed separately as shown in Figure 4.2. As already mentioned, the main usecase of TopView was the production of common DPD files for the top quark working group. TopView provides a variety of analysis types of which the following have been used to produce the DPD data [71]:

1. Pre physics analysis:
   This step refines the reconstructed physics objects that come with the ESD and AOD to make them suitable for top quark analysis.

2. Baseline analysis:
   This step does the object preselection and removes overlap (e.g. electrons that are stored separately from jets but are actually part of it). Additional processes like calibration or $b$-tagging are also done in this step.

3. Event analysis:
   The final analysis based on a event-by-event basis is also done by TopView. It contains a basic event selection and analysis of the event by reconstructing e.g. the top quark itself and the $W$-boson and $b$-jet from the top quark decay. However, this is a grey area since special analyses need a more dedicated view of the event; the event selection and reconstruction provided by TopView is therefore not to be used by default.

TopView is fully customizable. Additional analysis code can be easily implemented which has been done in the course of this thesis to implement the specific physics observables needed for the investigation of the decay length method. Parts of the implementation were successfully added as standard to the TopView tools while others were only used for the private re-processing of the data for several reasons that will be discussed in detail in appendix A. An overview of the respective implementations is listet in following, technical details are also described in appendix A:

- The reconstructed secondary vertices of jets. This was done on the baseline level by implementing the correct jet preselection, obtaining the reconstructed vertices of the jet and storing these with their associated jet in the final DPD output. The reconstructed secondary vertices were defined as a standard variable in TopView and are therefore available in the official samples.

- The reconstructed primary vertices of the event. These were only used in the private production.

- An event-by-event representation of the hard $t\bar{t}$ process from the Monte-Carlo level. This was done to obtain several MCTruth variables such as true primary and secondary vertices or a handle on the decay channel of the $t\bar{t}$ pair. This tool was only used for the private DPD production.

## 4.3 Reconstruction of physics objects

This section describes the definition of physics objects used throughout this thesis. These definitions and the underlying reconstruction of objects are standard in ATLAS. The event selection is optimized for the studies presented here but is mostly identical to the standard $t\bar{t}$ selection used in ATLAS. Note that the reconstruction of particle jets and vertices is described more detailed as they are the basic observables used in the decay length method. The leptons and missing energy are only used for the event selection and do not have a large impact on the results; their reconstruction is therefore only described briefly.

### 4.3.1 Particle jets

A particle jet or simply 'jet' is the collimated accumulation of particles in the shower processes of final state partons. The total content of particles in a jet is usually due to several parallel mechanisms described in the following. The jet is created from a final state parton which, due to color confinement, hadronizes into mesons or baryons. Accompanying hadrons may arise from gluon bremsstrahlung of the final state parton. The hadrons from this step decay further into what are mostly pions $\pi^{\pm}$ and kaons $K^{\pm}$ [11]. These mesons have large lifetimes and therefore traverse large parts of the detector; typical flightlengths are $c\tau_{\pi^{\pm}} \approx 7.8$ m and $c\tau_{K^{\pm}} \approx 3.7$ m [11]. The hadrons thereby create hits in the tracking detectors and are finaly stopped in the hadronic calorimeters, where they undergo shower processes and deposit their energy.
Additionaly to hadrons the jet can contain charged leptons and neutrinos from the decay of short living hadrons which occur in the early history of the jet. The charged leptons also create hits in the tracking systems and are measured by the electromagnetic calorimeter, while the neutrinos escape.
The formation of particle jets is very characteristic. Particles traversing the calorimeter deposit their energy in consecutive calorimeter cells called "towers" as shown in Figure 4.3. The direction of the jets is basically given by its parent final state parton, and the daughter particles emerge within an opening angle to this direction, making the jet looking cone-shaped as also seen in Figure 4.3.

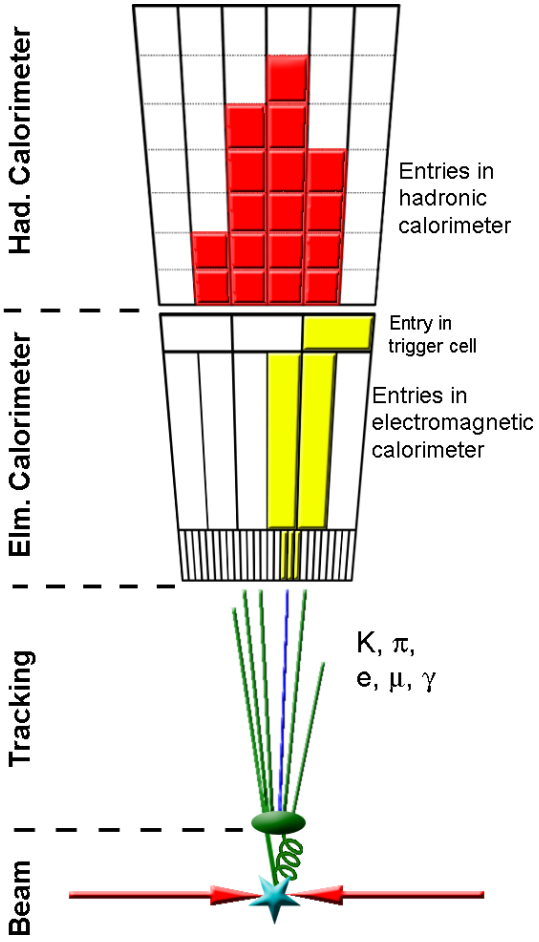


**Figure 4.3:** Sketch of a segment of the ATLAS detector with the formation and subsequent measurement of a cone-shaped particle jet.

Jets are reconstructed using dedicated algorithms, which are designed to map the measured energy to the initial parton as accurate as possible. A jet algorithm works in two steps:

1) association of calorimeter towers to identify the jet.

2) recombination of the set of momenta that have been identified with the jet in step 1).

For the reconstruction of jets in the present ATLAS analysis scheme the so-called "cone4" algorithm is used [72]. This algorithm associates all calorimeter towers to the jet that lie within a cone of

$$\Delta R = \sqrt{(\eta^i - \eta^C)^2 + (\varphi^i - \varphi^C)^2} < 0.4 \tag{4.4}$$

around the energy center of the jet. Here, $\eta^C$ and $\varphi^C$ are the coordinates of the cone center and $\eta^i$ and $\varphi^i$ are the coordinates of the geometric centers of the individual towers. $\eta$ and $\varphi$ are the pseudorapidity and azimuth of the jet as defined in Table 2.1.The algorithm starts with a trial cone and calculates the energy weighted center of this cone, which is than used as the new starting position for a new trial cone. This calculation is iterated until a stable cone is found, i.e. until the center of the energy deposition is identical to the geometric center of the cone. Figure 4.4 provides a schematic representation of the algorithm.

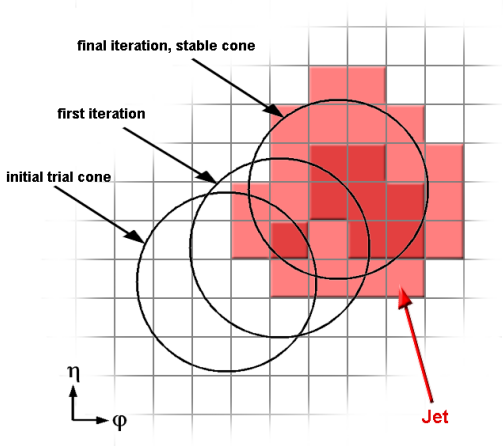


**Figure 4.4:** Sketch of the iterative jet reconstruction using the cone algorithm. The energy center of each cone is used as the center of a new cone in the next iteration step until the iteration is stable.

In the final step, the jet momentum is recombined by the summing up the four-momenta of the individual cells found within the cone to reconstruct the energy of the initial parton. This is a challenging task and a source of a serious amount of uncertainties due to several effect like detector resolution and acceptance, general instrumentational effects and algorithm dependance of the jet reconstruction. To map the measured jet energy back to the parton level a so-called called 'jet energy scale' (JES) correction factor is applied which is difficult to determine. At ATLAS an initial uncertainty of 5% on the JES is assumed, while the ultimate goal is 1% JES [56].

### 4.3.2 Primary and secondary vertices

At the LHC design luminosity of $10^{34}$ cm$^{-2}$ s$^{-1}$ the ATLAS experiment will face approximately 20 proton collisions per bunch crossing. The experiment therefore has to deal with a multi-vertex environment as shown in Figure 4.5.

A typical event will contain a pile-up of several proton-proton collisions. The so-called primary vertex (PV) is the point of the hard collision which is usually the focus of interest for all physics investigations. It is accompanied by by several low-$p_\perp$ proton-proton collisions (so-called minimum bias events). Other vertices in the event are the displaced secondary vertices (SV) coming from e.g. photon

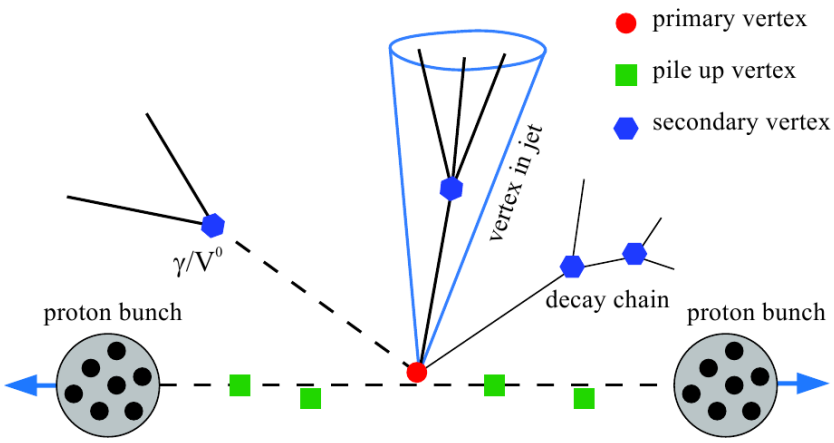


**Figure 4.5:** Vertex topologies as they are expected at the ATLAS experiment [73]. The proton-proton collision will produce primary vertices and pile-up vertices (red and green), while the decay products will produce secondary vertices (blue).

conversions ($\gamma$) or from long-lived neutral particles like $\Lambda^0$ or $K_S^0$ (called $V^0$ for historical reasons [74–76]) and vertices contained inside jets. Especially the jets from $b$-quarks and $c$-quarks have to be mentioned since both quarks produce hadrons with significantly large lifetimes and therefore largely displaced vertices. Additional tertiary vertices can occur in decay chains of particles that are contained inside the jet. An example of such a vetex is the vertex of hadrons containing a $c$-quark (referred to as $D$-hadrons) that are produced in the decay of $B$-hadrons in $b$-jets. This section focusses on the reconstruction of primary vertices and of secondary vertices from $b$-jets in ATLAS.

For the identification of primary vertices the InDetPriVxFinder algorithm [73, 77] is used. The algorithm uses a "fitting-after-finding" approach, starting from a preselected subset of tracks which are afterwards used for vertex fitting. An alternative process where tracks and vertices are fittet concurrently ("finding-through-fitting") is also implemented but not used in the course of the CSC studies. The InDetPriVxFinder algorithm starts by selecting ("finding") track candidates which are subsequently used for vertex fitting. To form a good candidate, the track must be compatible with the expected bunch crossing region, i.e. the impact parameter is required to be $d_0 < 1$ mm. Outlying tracks are neglected in the search for primary vertices. In the following step clusters along the $z$-axis are formed from the remainig candidates using the $z$-distribution of the individual impact parameters $z_0$ of each track. The tracks are ordered in $z_0$ and the full range of $z_0$ is scanned for clusters, where the maximum cluster size is restricted to be less than 3 mm. The resulting cluster is treated as an independent vertex candidate and the vertex is fitted using the Billoir method [78]. After the reconstruction of the initial vertex candidates, the tracks contributing a $\chi^2 > 5$ to that candidate are rejected and the vertex candidate is refitted to obtain the final vertex.

Secondary vertices from $b$-jets are more difficult to reconstruct. As already mentioned, these jets have a complex topology of secondary and tertiary vertices due to the presence of both long-lived $B$-hadrons and $D$-hadrons. The ATLAS reconstruction uses the BTagVrtSec algorithm [79] for the measurement of secondary vertices inside jets. The idea of this algorithm is to construct a single vertex for both $b$- and $c$-hadrons as sketched in Figure 4.6. The advantage of this method is that the vertex detection efficiency is maximized keeping the probability of finding fake vertices in light jets low at the same time. This is especially important when it comes to $b$-tagging, as the precise reconstruction of the decay chain is less important here.

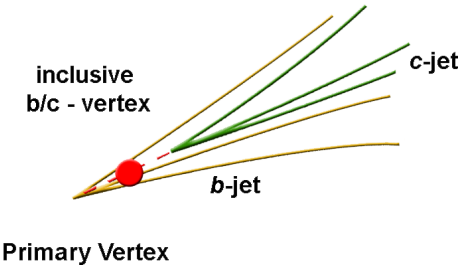


**Figure 4.6:** Sketch of the BTagVrtSec algorithm: all disclaced tracks are fittet to one inclusive secondary vertex. The separate $B$-hadron and $D$-hadron vertices are not distinguished.

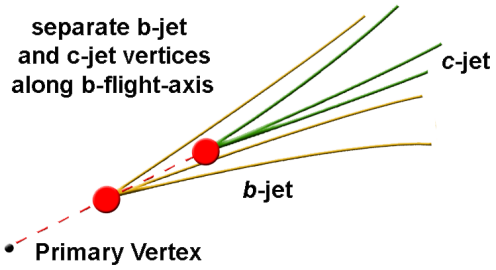


**Figure 4.7:** Sketch of the JetFinder algorithm: the secondary vertices of $b$- and $c$-jets are separately fittet using the $B$-hadron flight axis as a constraint.

Another method implemented in ATLAS is the JetFinder algorithm sketched in 4.7. This algorithm fits the secondary and tertiary vertex separately by assuming all particles in the decay chain to be located along a common axis, thereby reducing the problem from three dimensions to one. This method shall only be mentioned here for the sake of completness as it is not used in the course of this study.

The vertex finding using the BTagVrtSec algorithm starts from preselected tracks, which is a similar approach as in the finding of primary vertices. The difference in this step is that the preselection also uses more displaced tracks, i.e. the cut on the impact parameter is relaxed to $d_0 < 3.5$ mm. The vertex search continues by finding good ($\chi^2 < 4.5$) two-track vertex combinations inside the jet. Here, the jet is defined independently to the otherwise used jet algorithm by applying a cone of $\Delta R = 0.4$. To accept a two-track combination, each contained track must have a large enough distance $D_{SP}$ to the reconstructed primary vertex, precisely $D_{SP}/\sigma_{D_{SP}} > 2.0$ is required. To suppress two-track combinations from long living neutral particles like $\Lambda^0$ or $K^0_S$, these tracks are rejected if their associated invariant $\pi^+\pi^-$ and $p\pi^-$ mass spectra show peaks due to $\Lambda^0$ or $K^0_s$ decays. Example distributions of these mass spectra are shown in Figure 4.8 a) and b). Vertices from $\gamma$-conversions in the detector material are rejected by not accepting two-track vertex combinations that are located in this material as shown in Figure 4.8 c).

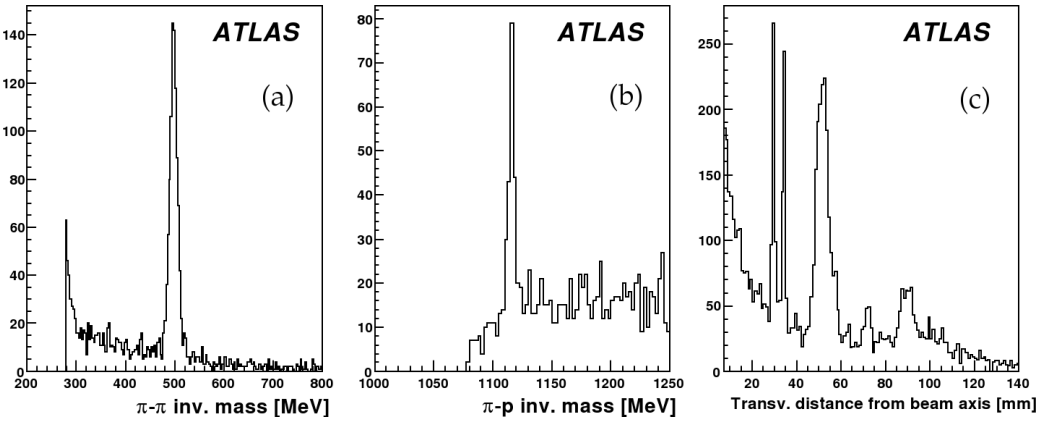


**Figure 4.8:** Properties of two-track combinations: (a) the $\pi^+\pi^-$ invariant mass spectrum with a peak of $K^0$ decays, (b) the $p\pi$ invariant mass spectrum with a peak of $\Lambda^0$ decays, (c) the transverse distance of primary and secondary vertices with peaks due to interactions in the beam pipe and pixel layers [79].

In the final step all remaining two-track vertex candidates are fitted to a single secondary vertex. If the resulting $\chi^2$ of this vertex fit is unacceptable ($\chi^2 > 3$), the candidate with the highest contribution to $\chi^2$ is removed and the vertex is refitted. This procedure is repeated until a good vertex is found. If no candidate is left, the jet is marked to have no reconstructable secondary vertex by setting the vertex coordinates to (0,0,0).

### 4.3.3 Leptons

In the semileptonic $t\bar{t}$ channel leptons play an important role as described in section 3.2.4. In particluar, electrons and muons are well reconstructable particles in contrast to the $\tau$-lepton due to its unpredictable behaviour. The reconstruction of $\tau$-leptons is therefore not considered further in this section as the focus lies on electrons and muons.

An electron is reconstructed by the tracking system and the electromagnetic calorimeters. The $\eta$-range in which an electron candidate is accepted is defined by the combined coverage of these two subdetectors, precisely the range $|\eta| < 2.5$ is accepted due to the tracker coverage (see Table 2.2) with an additional exclusion area $1.37 < |\eta| < 1.52$ due to the crack region in the calorimeter. To separate final state electrons from secondary electrons resulting from $b$- or $c$-hadron decays, an additional isolation criterion is applied. An electron candidate is flagged as isolated if the additional transverse energy $E_T$ in a cone with radius $\Delta R = 0.2$ around the electron axis is less than 6 GeV. Electrons measured by ATLAS are categorized by certain "quality" requirements which can be 'loose', 'medium' or 'tight'.

A full list of all quality requirements is found in [80], the basic 'medium' requirements which are used in this thesis are as follows:

- the accepted calorimeter cells are within $|\eta| < 2.47$,
- the first and second calorimeter layer must have measured a certain energy[3],
- at least one hit in the pixel detector and nine hits in the TRT must be present,
- the impact parameter must be smaller than 1 mm.

Muons are reconstructed by combining the information of both the inner detector and the muon spectrometer. The tracks of detectors are evaluated by separate tracking algoritms and matched by the STACO algorithm [81], which performs a statistical combination of the inner and outer track vectors to obtain the combined track vector. The acceptance for this algorithm is defined by the $\eta$-coverage of the inner detector ($\eta < 2.5$). To isolate muons from jets an isolation cut of 6 GeV similar to the electron reconstruction is applied.

Note that in the available MonteCarlo samples electrons and muons are only present if their transverse momentum is larger than 10 GeV as leptons with lower $p_\perp$ are truncated on the generator level.

### 4.3.4 Missing energy

Missing energy $\not{E}_\perp$ in the detector arises primarily from high momentum particles that only interact weakly with the detector. As these particles usually stem from the hard collision processes, $\not{E}_\perp$ is essential for many physics analyses in ATLAS. For example, the searches for new particles arising in supersymmetric scenarios will strongly rely on $\not{E}_\perp$, since neutral supersymmetric particles are expected to escape ATLAS undetected. In the case of semileptonic $t\bar{t}$ decays the presence of $\not{E}_\perp$ is due to the neutrino from the leptonic $W$-boson.

In the default ATLAS reconstruction, $\not{E}_\perp$ is measured starting from the reconstructed and calibrated high-$p_\perp$ objects in the event. All energy outside these objects is further classified as low-$p_\perp$ deposits and calibrated accordingly.Additional corrections are applied for e.g. the assumed energy loss in the cryostats and other 'dead' regions like readout electronics. The total sum of all missing energy is than calculated from the by adding up the contributions from each type of component:

$$\not{E}_\perp = -\sum_i \left( E_{xy,i}^{\text{high-}p_\perp} + E_{xy,i}^{\text{low-}p_\perp} \right) \tag{4.5}$$

### 4.3.5 Identification of $b$-jets

As already mentioned in section 4.3.2 the jets stemming from $b$-quarks are usually displaced due to the high lifetime of the $b$-quark. The displacement is measureable by both the impact parameter from the jet tracks as well as from the secondary vertex of the jet. This fact is used by $b$-tagging algorithms that try to identify $b$-jets by their displacement. ATLAS analyses use a tagger that combines a secondary vertex based algorithm (SV1) and an algorithm based on the measurement of the three-dimensional impact parameters (IP3D).

The impact parameter based tagging uses the signed impact parameter for the discrimination of light jets and $b$-jets. The sign is calculated with respect to the primary vertex from the direction of the jet and the position of the primary vertex:

$$\text{sign}(d_0) = \left(\vec{e}_{p_\text{j}} \times \vec{e}_{p_\text{t}}\right) \cdot \left(\vec{e}_{p_\text{t}} \times (\vec{r}_\text{PV} - \vec{r}_\text{t})\right) . \tag{4.6}$$

Here, $\vec{e}_{p_\text{j}}$ is the unit vector pointing in the direction of the jet axis, $\vec{e}_{p_\text{t}}$ is the direction of the track, $\vec{r}_\text{PV}$ is the position of the primary vertex and $\vec{r}_\text{t}$ is the position of the track point of the closest approach to the primary vertex. sign($d_0$) is expected to be randomly distributed for tracks from the primary vertex, while tracks from $b$-jets (and $c$-jets) tend to have positive sign [82]. Figure 4.9 a) shows the distributions for signed impact parameters for tracks from light jets, $c$-jets and $b$-jets as they are expected for the ATLAS experiment. Instead of the sign itself, the significance $d_0/\sigma_{d_0}$ is usually used since it gives more weight to precisely measured tracks. The distribution of significances for the impact parameters shown in Figure 4.9 a) are shown in Figure 4.9 b).

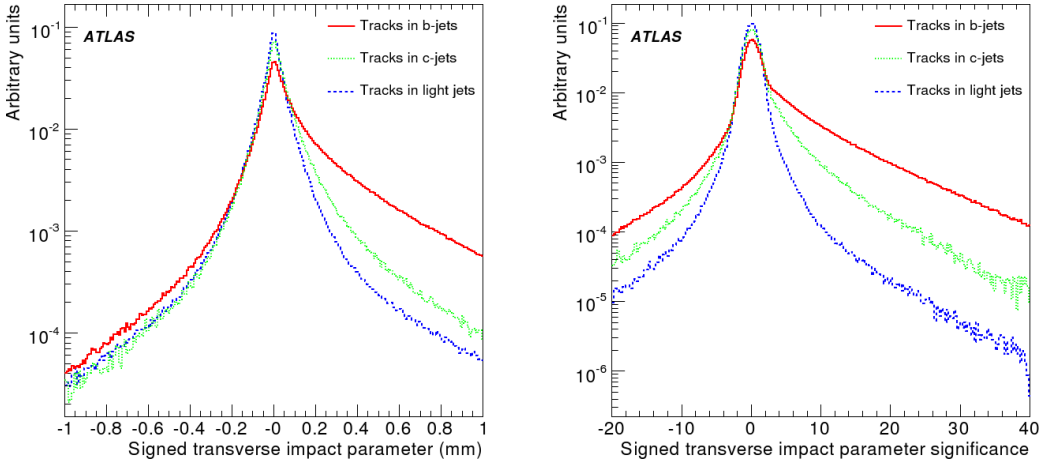


(a) (b)

**Figure 4.9:** Signed impact parameter distributions (a) for tracks in light jets (blue), $c$-jets (green) and $b$-jets (red) and their significances (b) as expected for the ATLAS experiment [82].

Secondary vertex based $b$-tagging starts from the reconstruction of secondary vertices as described in section 4.3.2. For a reconstructed vertex three of its properties can be used to discriminate light jets from $b$-jets, these are the invariant mass of all tracks associated to this vertex, the ratio of the sum of energies of these tracks to the sum of the energies of all tracks in the jet and the number of two-track vertices. Figure 4.10 illustrates these properties for light jets and $b$-jets.

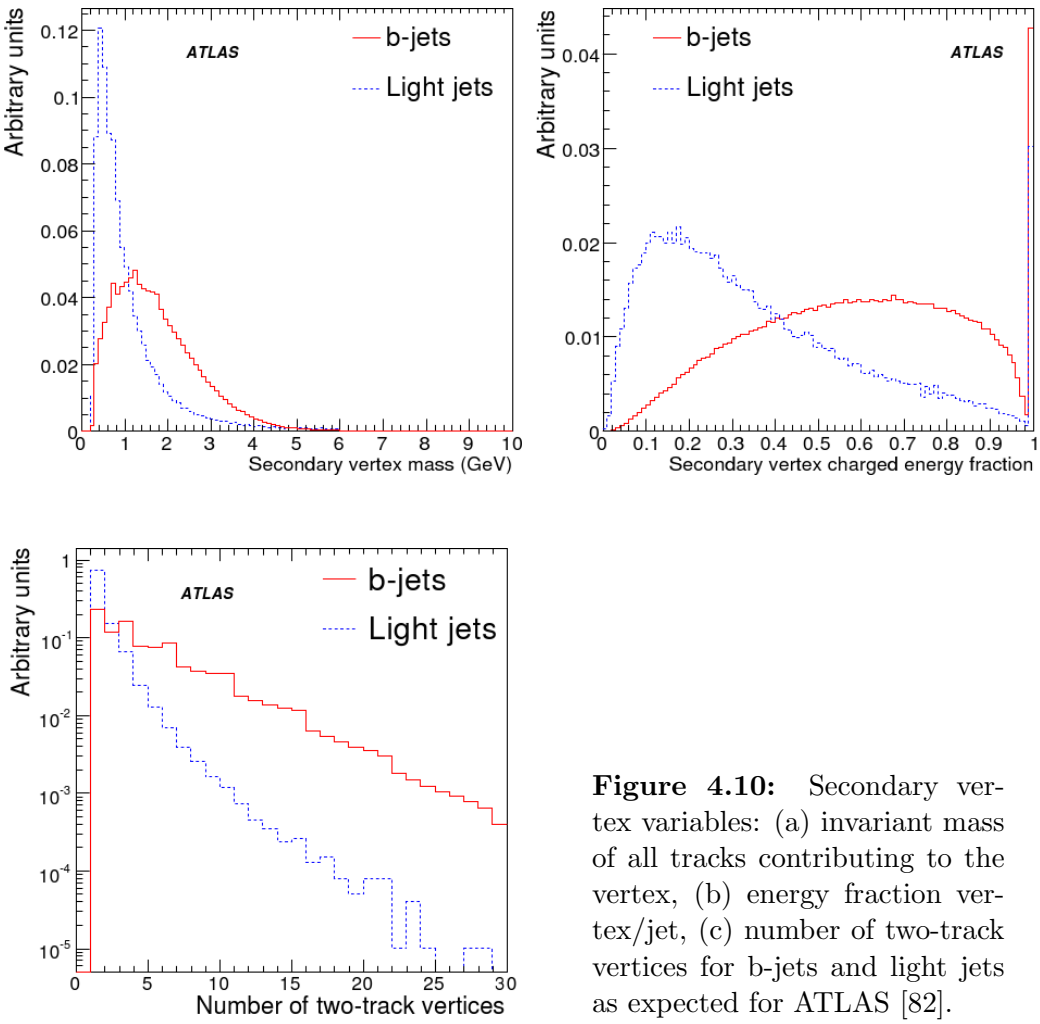


**Figure 4.10:** Secondary vertex variables: (a) invariant mass of all tracks contributing to the vertex, (b) energy fraction vertex/jet, (c) number of two-track vertices for b-jets and light jets as expected for ATLAS [82].

The final tagging for both impact parameter based and secondary vertex based methods uses a likelihood ratio technique. The discriminating variables are compared to pre-defined and normalized probability distributions for the $b$-jet and light jet hypotheses $P(b)$ and $P(u)$. The so-called 'tagging weight' $w$ for each track or vertex $i$ is than calculated from this comparison by $w_i = P_i(b)/P_i(u)$. The total jet weight is thus given by the logarithmic sum of $w_i$

$$w_j = \sum_i \ln(w_i) = \sum_i \ln\left(\frac{P_i(b)}{P_i(u)}\right) . \tag{4.7}$$

The combined total jet weight used in ATLAS is simply calculated by the sum of weights of both IP3D and SV1:

$$w_j = w_{\mathrm{IP3D}} + w_{\mathrm{SV1}} . \tag{4.8}$$

The distributions of for $w$SV1, $w$IP3D and $w$IP3D+SV1 of light jets, $c$-jets and $b$-jets for $w_j$ as found in the available MonteCarlo data are shown in Figure 4.11. In the analysis of reconstructed jets this distribution can be used to label jets as either light jets or $b$-jets if their weight $w_j$ is lower or higher a pre-defined threshold, which is called the $b$-tag cut. This cut is chosen such that the overall $b$-tagging efficiency is $\varepsilon_b = 60$ %. The final value of this cut depends on the object- and event selection that is applied to the event and will be discussed in section 4.4.5.

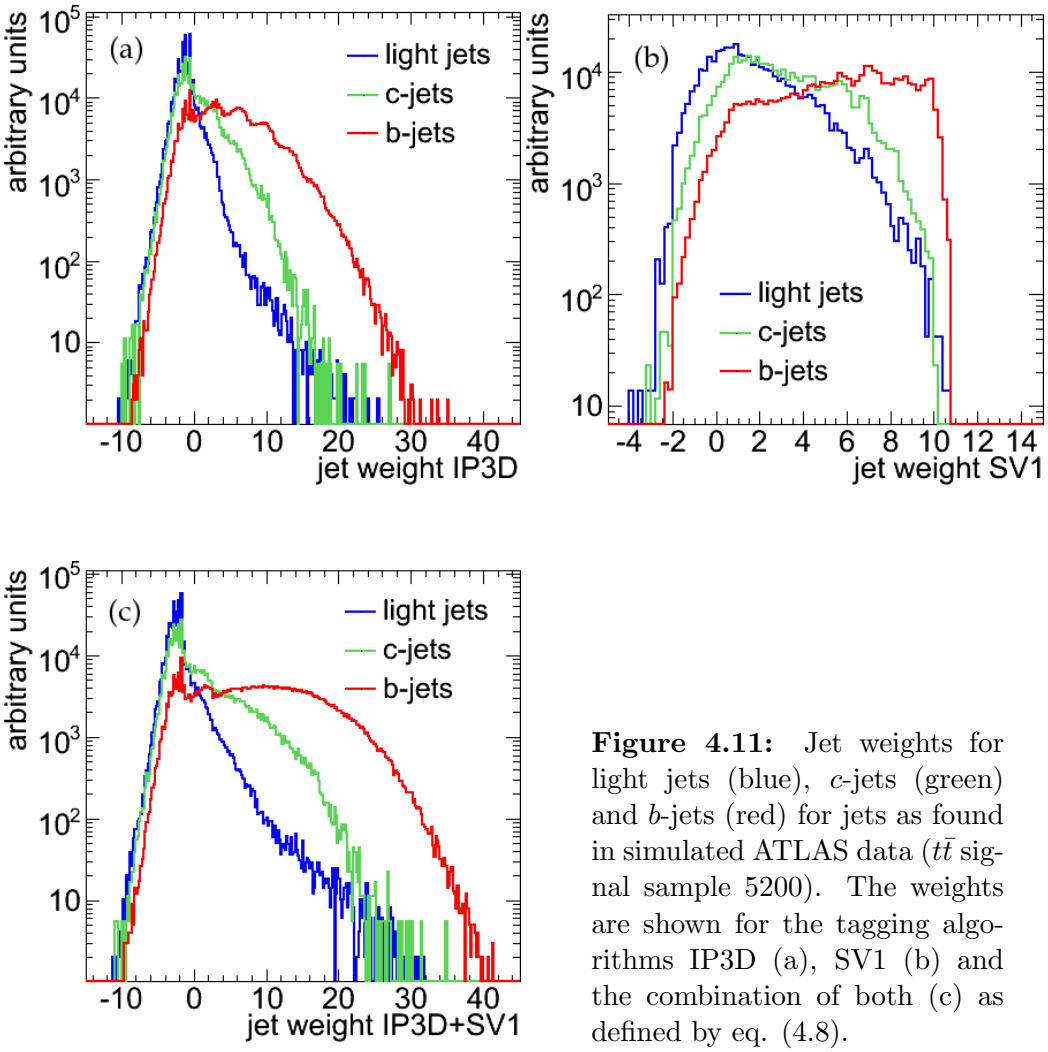


**Figure 4.11:** Jet weights for light jets (blue), $c$-jets (green) and $b$-jets (red) for jets as found in simulated ATLAS data ($t\bar{t}$ signal sample 5200). The weights are shown for the tagging algorithms IP3D (a), SV1 (b) and the combination of both (c) as defined by eq. (4.8).

## 4.4 Event Selection for $t\bar{t}$ Events

As already mentioned this thesis focusses on analysis in the semileptonic $t\bar{t}$ channel. An appropriate event selection that filters a large part of signal events from the background can be derived from th decay topology of this channel which was described in detail in section 3.2.4 and summarized in Table 3.5. The detector signatures associated to this topology are:

- four high-$p_\perp$ jets of which two are $b$-jets,
- one high-$p_\perp$ lepton, where only electrons and muons are considered here,
- a large amount of missing energy.

For the application of the event selection the previously described physics objects are used. Most of the cut values used within this thesis had been commonly defined previously by the top quark working group for the CSC studies. The cuts of particle jets are an exception to this for reasons that are discussed in detail in section 5.3.3. Although the reconstructed physics objects were provided by TopView, the cuts had to be implemented manually in the analysis as discussed in section 4.2.2. This holds for both the object selection described previously as well as for the special event selection cuts listet in the following.

### 4.4.1 Trigger

From the trigger menu described in section 2.3 the trigger items e25i and $\mu$20i are used for selection. This corresponds to the presence of a high-$E_\perp$ electron ($E^e_\perp > 25$ GeV) or muon ($E^\mu_\perp > 20$ GeV) from the leptonic $W$-boson in the top quark decay. The selection is done exclusive, i.e. only events with either exactly one electron *or* one muon are accepted.

### 4.4.2 Leptons

Exactly one reconstructed lepton (either electron or muon) with $p^e_\perp > 25$ GeV or respectively $p^\mu_\perp > 20$ GeV is requested. This cut basically corresponds to the trigger selection. As with the trigger selection, the lepton is required to be exclusively an electron or muon.

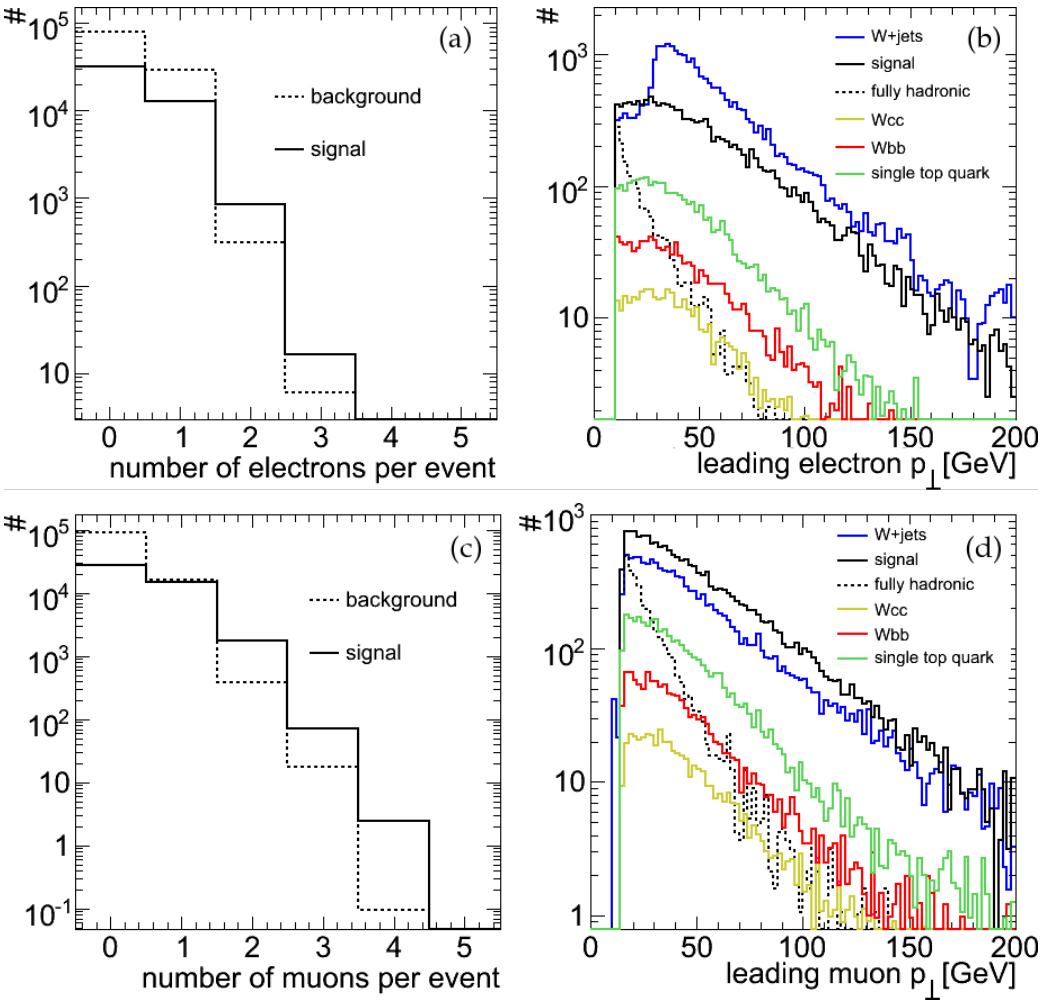


**Figure 4.12:** Electron and muon multiplicities ((a) and (c)) and their leading transverse momenta $p_\perp$ ((b) and (d)) in signal and background events. All distributions are scaled to represent an integrated luminosity of 100 pb$^{-1}$.

Figure 4.12 shows the multiplicity of leptons and their distribution of the leading transverse momenta as found in the $t\bar{t}$ signal samples 5200 and 5204 and the background samples $W$+jets, $Wbb$, $Wcc$ and single top quark. The distribution of the leading $p_\perp$ demonstrates the discrimination power of the lepton requirement to reduce low-$p_\perp$ QCD background. Although this has not been investigated with dedicated samples, the fully hadronic signal sample can be taken as an example due to the similar topology which basically consists of jets and no high-$p_\perp$ lepton. As mentioned earlier most of the other background samples are not affected to much by this cut as they were forced to contain leptons during their generation. Note that the $p_\perp$ distributions are truncated below 10 GeV (electrons) due to generator cuts described in section 4.3.3.

### 4.4.3 Missing energy

$\not{E}_\perp$ is required to be $> 20$ GeV. Together with the lepton requirement, this cut discriminates the investigated samples from QCD background, which is obvious from the fully hadronic $t\bar{t}$ sample similar to the lepton cut. The distributions of $\not{E}_\perp$ in the $t\bar{t}$ signal sample 5200 and 5204 ($m_t = 175$ GeV) as well as the background samples for $W$+jets, $Wbb$, $Wcc$ and single top quarks are shown in Figure 4.13.

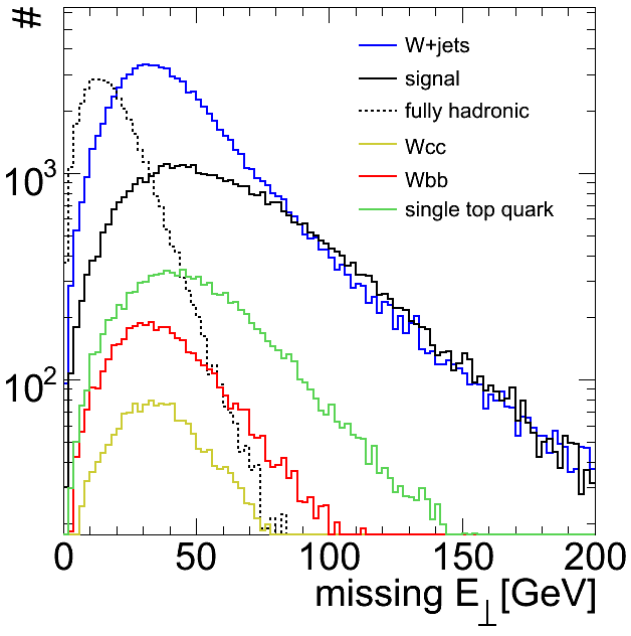


**Figure 4.13:** Distribution of $\not{E}_\perp$ for the $t\bar{t}$ signal samples and background from $W$+jets, $Wbb$, $Wcc$ and single top quarks. The signal is separated into the combined semi- and dileptonic contribution (solid black line) and the fully hadronic contribution (dashed black line).

### 4.4.4 Particle jets

At least four jets with $p_\perp^{\text{jet}} > 15$ GeV are requested. Though the $p_\perp$ cut is within range allowed for the CSC studies, it should be mentioned that it has been changed from the CSC default of $p_\perp^{\text{jet}} > 40$ GeV to ensure the stability of the decay length method. The instability at higher cut values is due to an effect of a combined dependance of the decay length on both the $p_\perp^{\text{jet}}$ cut and the top quark mass which will be discussed in detail in section 5.3.3. The distribution of the jet multiplicity for all events in the signal samples and the distributions of jet $p_\perp$ for these samples are shown in Figure 4.14. The respective samples are 5200 and 5204 for the $t\bar{t}$ signal and $W$+jets, $Wbb$, $Wcc$ and single top quark for the background. It is evident that the cut on the jet $p_\perp$ is working only on the lower bound of the distribution and that a higher cut of $p_\perp^{\text{jet}} > 40$ GeV has a higher rejection power. Nevertheless, the low cut is kept in the further analysis for the just mentioned reasons.

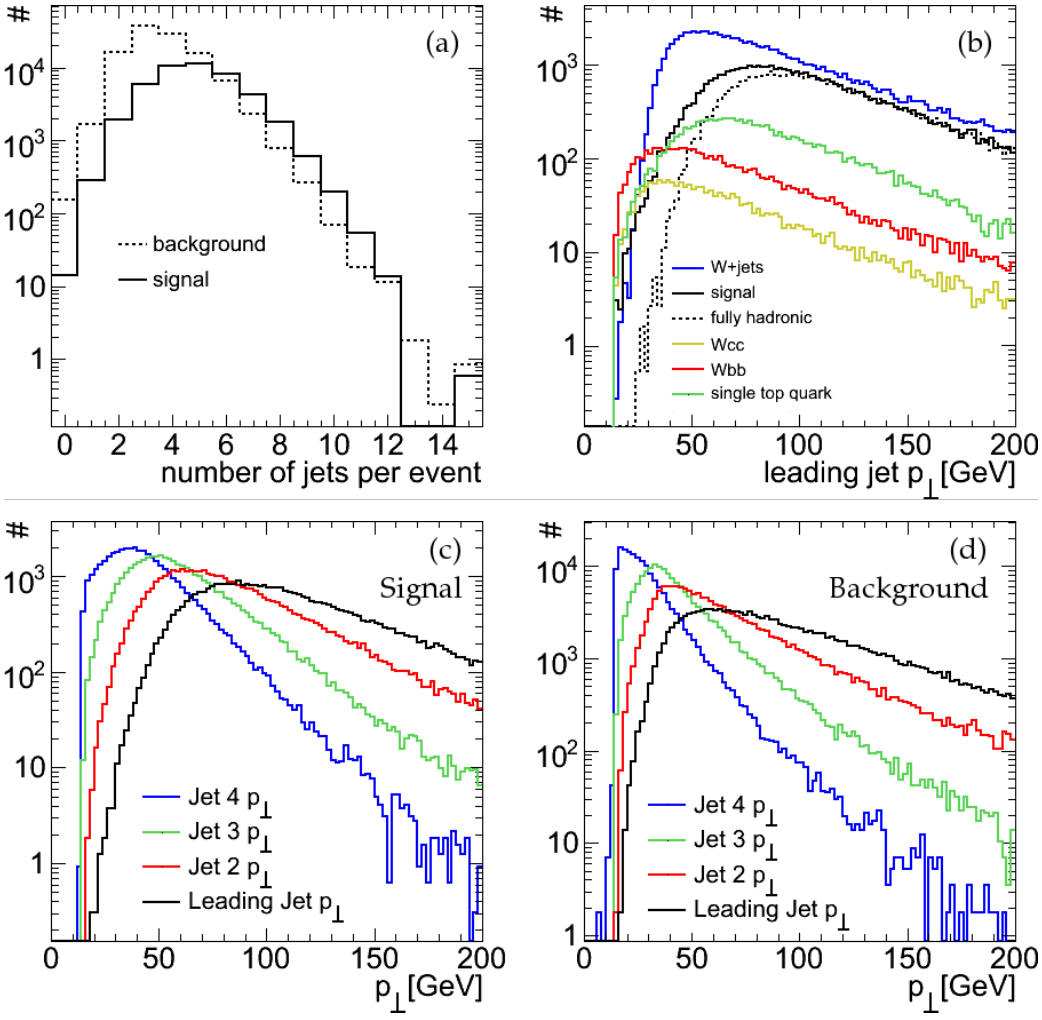


**Figure 4.14:** Jet multiplicities from signal and background events (a) and leading transverse momenta $p_\perp$ for subsamples of these events with four or more jets (b). (c) and (d) represent the $p_\perp$ distributions of the four leading jets in the signal and background samples for all events with at least four jets.

### 4.4.5 *b*-tagging

Out of all jets in an event exactly one *or* two must be identified as a *b*-jet. This is the most essential cut concerning the decay length method since the tagged jets are assumed stem from the *B*-hadron from the top quark decay. As described in section 4.3.5 the cut on the jet weight is chosen such that a *b*-tagging efficiency of $\varepsilon_b = 60\%$ is achieved. The efficiency is defined as the number of the true *b*-jets passing the selection, i.e. whose jet weight $w_j$ is higher than the *b*-tag cut $c_b$, divided by the total number of all true *b*-jets:

$$\varepsilon_b = \frac{N_{(\text{true b-jet AND tagged})}}{N_{(\text{true b-jet})}} \,. \tag{4.9}$$

To determine the denominator in eq. (4.9) the true *b*-jets have to be identified from the reconstructed jets that pass the event selection. The identification of true *b*-jets is done by matching the *b*-partons from MCTruth to the jets. A jet-to-parton combination is matched if their distance in $\eta$-$\varphi$ is

$$\Delta R = \sqrt{(\eta_j - \eta_b)^2 + (\varphi_j - \varphi_b)^2} < 0.2 \,. \tag{4.10}$$

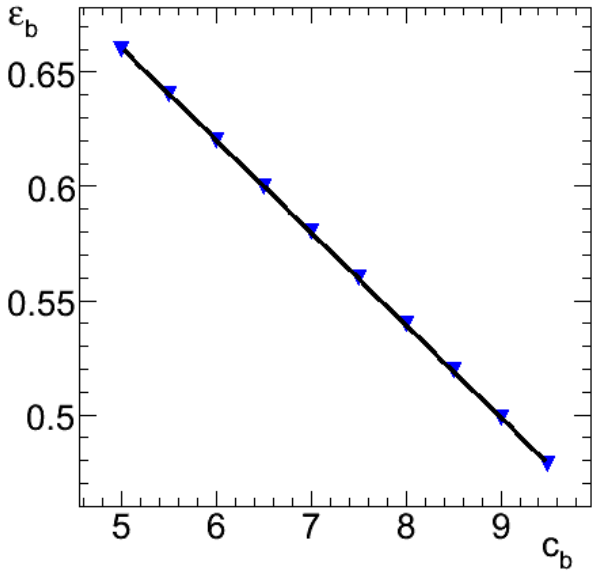


**Figure 4.15:** The *b*-tagging efficiency as a function of the *b*-tag cut for the determination of the cut $c_b(\varepsilon_b = 60\%)$. The sample is the semileptonic subsample of the $t\bar{t}$ signal sample 5200.

This technique has been applied to the selected semileptonic $(e + \mu)$ events from the $t\bar{t}$ signal sample 5200 for various values $c_b$ of the *b*-tag cut to determine $\varepsilon_b(c_b)$ using eq. (4.9). The distribution of jet weights for the combined SV1+IP3D tagger are shown in Figure 4.16, The resulting values for $\varepsilon_b$ are shown in Figure 4.15. The function $\varepsilon_b(c_b)$ is obtained by a linear fit to these values. The result

$$\varepsilon_b(c_b) = (-0.04039 \pm 0.00008) \cdot c_b + (0.8624 \pm 0.0006) \tag{4.11}$$

can be used to determine the *b*-tag cut that represents a *b*-tagging efficiency of 60% :

$$c_b(\varepsilon_b = 60\%) = 6.496 \pm 0.021 \,, \tag{4.12}$$

which is marked in Figure 4.16. Note that this value has been obtained for the reference signal sample 5200 where $m_t = 175$ GeV. Nevertheless, this cut is used

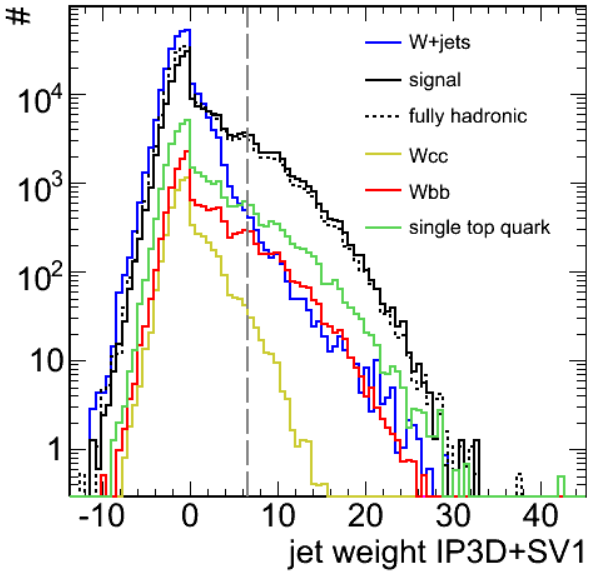


**Figure 4.16:** Distribution of the combined jet weight SV1+IP3D for all jets found in the $t\bar{t}$ signal samples and the background samples. All samples are scaled to represent an intergrated luminosity of 100 pb$^{-1}$. The dashed vertical line marks the cut value $c_b(\varepsilon_b = 60\%)$.

by default for all samples that are investigated in the course of this thesis. This includes the signal samples with other simulated top quark masses as well, although in principle one has to expect a dependance of $\varepsilon_b(c_b)$ on $m_t$.

As the tagged $b$-jets will be used in the analysis to determine the decay length, the purity $\mathcal{P}$ of the selection can be defined using the fraction of jets that are tagged but do not stem from $b$- or $\bar{b}$-quarks from the top quark decays. For the $t\bar{t}$ signal sample 5200 this is found to be

$$\mathcal{P} = 1 - \frac{N^{\text{tagged}}_{\text{wrong}}}{N^{\text{tagged}}_{\text{all}}} = \frac{N^{\text{tagged}}_{\text{right}}}{N^{\text{tagged}}_{\text{all}}} = 86.1\% \tag{4.13}$$

using the cuts defined in this section. This result is also obtained for the samples 6203 and 6204 with different top quark masses. Using the default cuts from CSC studies with $p_\perp^{\text{jet}} > 40$ GeV instead of 20 GeV, one finds that the purity changes only slighty to $\mathcal{P}^{\text{CSC}} = 87.4$ %.

The multiplicities of tagged jets using the weight cut defined by eq. (4.12) for the signal samples 5200 and 5204 as well as for the background samples $W$+jets, $Wbb$, $Wcc$ and single top quark are shown in Figure 4.17. The $b$-tagging cut is therefore found to have a high rejection power on the physical background. The fraction of signal events with either one or two $b$-tagged jets is $\epsilon_{\text{Sig}} = 72.58$ %, while only $\epsilon_{\text{Bck}} = 13.72$ % of background events fulfill this requirement. 86.21 % of all background events do not have any jet that passed the $b$-tagging cut. The rejection factor of this cut is therefore

$$\text{R}_{\text{rej}} = \frac{\epsilon_{\text{Sig}}}{\epsilon_{\text{Bck}}} = 5.3\,. \tag{4.14}$$

It should be noted that a $b$-jets is not necessarily one of the four jets with highest $p_\perp$. Figure 4.18 shows the distribution of $b$-tagged jets from the reconstruction as well as of MCTruth $b$-jets sorted by their $p_\perp$ (called jet ID in the Figure). 5.7 % of all true $b$-jets and 6.6 % of reconstructed $b$-tagged jets are found in the jets with an ID $> 3$, i.e. they are not part of the four leading jets. A possible modification of the cut that has been considered within other CSC analyses [49] is to request that the $b$-tagged jets are required to be among the four leading jets. This

modification does however not lead to a significant change in the purity which increases only about 1 % to $\mathcal{P} = 86.4$ %, thereby decreasing the total amount of considerable jets by 5.3 %. Thus, this modification will not be considered further.

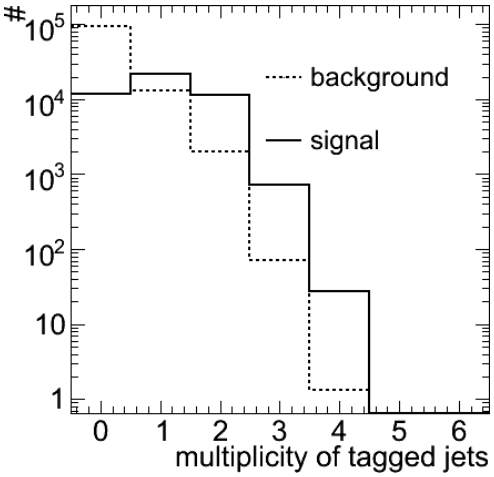


**Figure 4.17:** Multiplicity of tagged jets in the $t\bar{t}$ signal samples (solid) and background samples (dashed). All events are scaled to represent an integrated luminosity of 100 pb$^{-1}$.

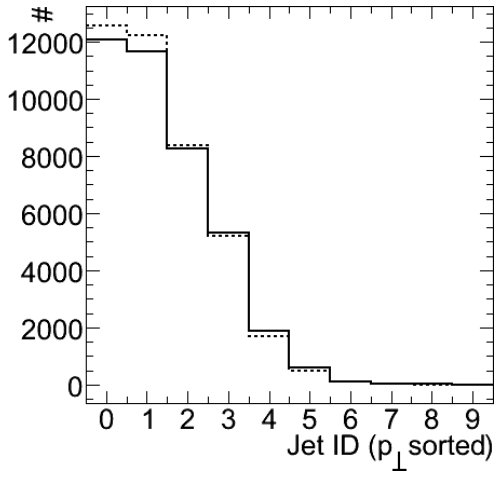


**Figure 4.18:** Distribution of identification number of tagged jets (solid) and of true $b$-jets from top quark decays (dashed). The distributions are obtained from the unscaled $t\bar{t}$ signal sample 5200.

### 4.4.6 Cut efficiency

the cut based step-by-step reduction of events, which is referred to also as the cut flow, is shown in Table 4.6 on page 72 for the previously described samples. In each step, the respective cuts of the previous step are extended by one further cut, making the last step the complete event selection as described in this section. The cut sequence is

I combined trigger and lepton cut,

II missing energy $\not{E}_\perp$,

III number and $p_\perp$ of particle jets,

IV $b$-tagging.

The numbers of events in Table 4.6 are scaled using eq. (4.3) to represent an integrated luminosity of 100 pb$^{-1}$. A graphical representation of this cut flow of the $t\bar{t}$ signal samples with central mass ($m_t = 175$ GeV) combined with the relevant physics background is shown in Figure 4.19.

Although the event selection is optimized for a selection of the semileptonic $t\bar{t}$ decay channel, one obtains the benefit of having a large contribution to the signal from the dilepton channel. The fully hadronic channel is strongly supressed, which can be explained by the cut on the lepton and missing energy what becomes clear directly in the first step of the cut flow. Nevertheless, a small contribution remains which can also be counted as signal.

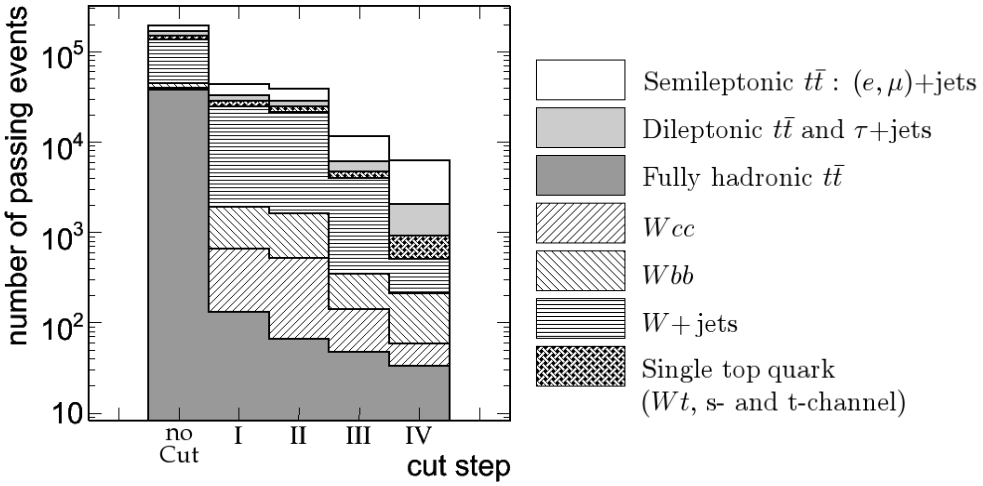


**Figure 4.19:** The cut flow for the $t\bar{t}$ signal samples with the central mass ($m_t$ = 175 GeV) and the respective background samples. The unicolored areas represent the $t\bar{t}$ signal contributions, the dashed areas are background.

The remaining background is strongly suppressed by the event selection. This holds especially for the $W$+jets background which is reduced to 0.5 % of its initial amount as can be seen in Table 4.6. Note however that the largest contribution arises from the $W$+jets samples which is not expected a priori. As already mentioned this is assumed to be due to the double counting of $Wbb$ and $Wcc$ events in the $W$+jet samples. In a worst case scenario the contribution of $W$+jets must be taken completely into account which is shown in Figure 4.19. The signal to background ratio in this case is $S/B^{w.c.} = 6.07$. The best case scenario is obtained by assuming that the light jet contribution is completely rejected by the event selection and the remaining events are due to double counting of heavy jets. In this case, the correct contribution of heavy jets is described by the $Wbb$ and $Wcc$ samples alone and the $W$+jets sample must not be taken into account. The best case signal to background ratio is then found to be $S/B^{w.c.} = 9.15$. Note that the influence on the decay length method is a more complex problem than simply the view of the signal to background ratio, as the distribution of decay lengths is the decisive factor. An estimate on this will be discussed in detail in section 5.2.3.

A special case of background is the presence of single top quark events. As described in section 4.1.3 the samples are created such that they have a similar signature to $t\bar{t}$ events. This also involves the presence of one or two $b$-quarks of which one stems from the top quark and one is an associating parton from the hard process. As the $b$-quarks from the top quark decay in principle can be counted as signal, the contribution of single top quarks also suffers from an admixture of $b$-quarks which are not correlated to the top quark decay. As with the $W$+jets background, the effect on the decay length method will be discussed in section 5.2.3.

The $t\bar{t}$ signal samples with three different top quark masses behave as expected. The number of events passing the event selection increases linearly with higher top quark mass as seen clearly in Table 4.6. This is due to the fact that higher initial top quark masses can produce decay products with higher momen-

tum which therefore are more likely to pass the event selection. However it should be noted that the cut flow is strongly dependant on the choise of the jet $p_\perp$ cut as mentioned earlier. Applying the CSC default cut (four jets with $p_\perp^{\text{jet}} > 40$ GeV each), one finds that especially the sample with the low top quark mass ($m_t = 160$ GeV) suffers from this cut as can be seen from Table 4.5. The rejection factors $\mathrm{R_{rej}} = N_{\text{no Cuts}}/N_{\text{all Cuts}}$ of the combined semileptonic and dileptonic channels are compared in Table 4.5 for both the low and high jet $p_\perp$ cut, which is $p_\perp^{\text{jet}} > 15$ GeV and $p_\perp^{\text{jet}} > 40$ GeV respectively. The effect on the final analysis is discussed separately in section 5.3.3.

**Table 4.5:** The cut flow for the $t\bar{t}$ signal samples 5200, 6203 and 6204 for the CSC default jet $p_\perp$ cut ($p_\perp^{\text{jet}} > 40$ GeV). The shown cut flow starts from the jet cut as the other cuts were not changed here. The rejection factor for the 'high jet cut' is obtained from the final number of passing events in the last cut step in relation to the number of events with no cuts applied. The respective number for the 'low jet cut' is obtained from Table 4.6. All numbers are scaled to 100 pb$^{-1}$.

| physics signature | No cut | Jets cut (CSC) | $b$-tagging | $\mathrm{R_{rej}}$ high jet cut | $\mathrm{R_{rej}}$ low jet cut |
|---|---|---|---|---|---|
| Cut Step | | III | IV | | |
| $t\bar{t}$ signal, combined semi- and dilepton channel | | | | | |
| $m_t = 160$ GeV | 45517.4 | 1687.61 | 1353.09 | 33.6 | 9.5 |
| $m_t = 175$ GeV | 45517.4 | 2311.39 | 1856.23 | 24.52 | 8.53 |
| $m_t = 190$ GeV | 45517.4 | 2698.43 | 2178.71 | 20.89 | 7.93 |

The samples with modified $\Lambda_{\text{QCD}}$ show a higher number of passing events in the high mass sample ($2 \times \Lambda_{\text{QCD}}^{\text{ISR}}$) than the reference sample while the low mass sample goes vice versa. This can be explained by the higher (lower) multiplicity of reconstructed jets in the high mass (low mass) sample with respect to the reference sample as seen in Figure 4.20. The effect can be understood by taking into account the higher intensity of bremsstrahlung of the initial state partons which are more likely to produce jets. This is not the case for bremsstrahlung in in $t\bar{t}$ final states, where the top quarks do not produce bremsstrahlung due to their extremly short lifetime and the bremsstrahlung from the further decay products is more likely to immerse in their respective jets. The average number of reconstructed jets $N_{\text{jets}}$ in the samples is found to be $N_{\text{jets}}^{\text{low}} = 5.21$ in the high mass sample, $N_{\text{jets}}^{\text{high}} = 4.78$ in the low mass sample and $N_{\text{jets}}^{\text{ref}} = 4.98$ in the reference sample with normal reconstructed mass.

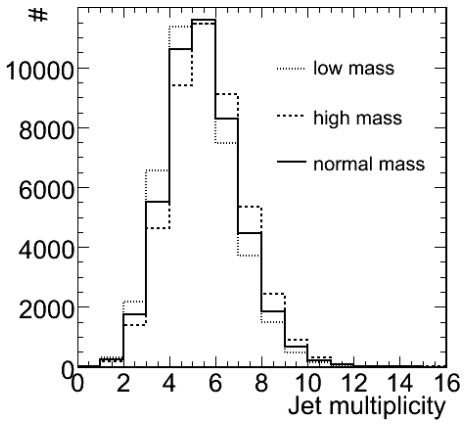


**Figure 4.20:** Jet multiplicities in the $t\bar{t}$ signal samples with modified $\Lambda_{\text{QCD}}$.

**Table 4.6:** The step-by-step reduction of events (cut flow) for all investigated samples usin the event selection criteria described in section 4.4. Every step uses the selection from the previous step adding the additioanl cut associated to that step. All numbers are events passing the respective step scaled to 100 pb$^{-1}$.

| physics signature | No cut | trigger and leptons | $\not\!\!E_\perp$ | Jet number and $p_\perp$ cut | $b$-tagging |
|---|---|---|---|---|---|
| Cut Step | | I | II | III | IV |
| $t\bar{t}$ ($m_t = 175$ GeV) | | | | | |
| $t\bar{t}$ Signal $\ell+$ jets ($\ell = e, \mu$) | 24010.9 | 10621.0 | 9552.8 | 5398.9 | 4186.8 |
| $t\bar{t}$ Signal $2\ell$ and $\tau+$ jets | 21506.4 | 4485.0 | 4205.6 | 1478.4 | 1151.6 |
| $t\bar{t}$ Signal fully hadronic | 37782.6 | 130.3 | 65.1 | 47.129 | 33.4 |
| Single top ($m_t = 175$ GeV) | | | | | |
| Single top $Wt$ | 2907.0 | 957.2 | 837.9 | 296.2 | 189.7 |
| Single top s-channel | 345.0 | 91.3 | 81.2 | 10.0 | 8.1 |
| Single top t-channel | 7967.4 | 2333.1 | 2080.5 | 318.8 | 212.0 |
| $W$+jets background | | | | | |
| $Wbb$ | 5118.6 | 1255.5 | 1084.2 | 208.5 | 152.0 |
| $Wcc$ | 2102.0 | 524.8 | 450.7 | 93.4 | 25.6 |
| $W$+jets | 91156.7 | 22842.6 | 19873.2 | 3668.7 | 297.6 |
| $t\bar{t}$ ($m_t = 160$ GeV) | | | | | |
| $t\bar{t}$ Signal $\ell+$ jets ($\ell = e, \mu$) | 24010.9 | 10449.1 | 9305.3 | 5109.7 | 3852.4 |
| $t\bar{t}$ Signal $2\ell$ and $\tau+$ jets | 21506.4 | 4477.7 | 4167.6 | 1259.8 | 939.7 |
| $t\bar{t}$ ($m_t = 190$ GeV) | | | | | |
| $t\bar{t}$ Signal $\ell+$ jets ($\ell = e, \mu$) | 24010.9 | 10669.4 | 9556.8 | 5709.2 | 4539.9 |
| $t\bar{t}$ Signal $2\ell$ and $\tau+$ jets | 21506.4 | 4608.61 | 4344.5 | 1539.1 | 1198.8 |
| $t\bar{t}$ with varied $\Lambda_{\mathrm{QCD}}$ ( = initial and final state radiation) ($m_t = 175$ GeV) | | | | | |
| $t\bar{t}$ low mass | 45517.4 | 14707.5 | 13375.7 | 7457.8 | 5797.1 |
| $t\bar{t}$ normal mass | 45517.4 | 14931.5 | 13544.1 | 7328.3 | 5597.7 |
| $t\bar{t}$ high mass | 45517.4 | 14817.2 | 13429.7 | 7116.4 | 5395.1 |

# Chapter 5

# The Decay Length Method For Top Quark Mass Measurement

As already discussed the top quark mass is an important parameter in both standard model calculations and as a constraint to new physics, especially concerning the Higgs-boson mass and MSSM. Therefore, detailed studies on the possibility to study the top quark mass at ATLAS have been performed in advance to the experiment's start. The main course of this chapter is the presentation of studies on a relatively new method for the determination of the top quark mass. This so called decay length method measures the mean transverse decay length of $B$-hadrons emerging from top quark decays and infers it to the mass of the parent top quark. This technique has originally been developed by CDF [83] and has not been considered at ATLAS before. Therefore, the studies presented here will focus on matters concerning the initial appliance of this technique to the ATLAS experiment. These matters can be summarized as follows:

- applicability of the method to ATLAS conditions,
- estimation of its uncertatinties with a focus on systematics and
- further prospects of the method.

This chapter deals with the physics concerned with this technique. The implementation of analysis tools that have been developed especially for this study are described in appendix A.

## 5.1 Principle of the decay length method and the analysis approach

As discussed in section 3.2.4 the top quark decay has a very characteristic topology. For the discussion of the decay length method the following summarized features of the decay are relevant:

- The top quark decays as a (quasi-) free particle, i.e. all properties of the top quark are directly correlated to the decay products.
- A top quark decays almost exclusively into a $b$-quark and a $W$-boson via weak interaction.

- The mass of the top quark $m_t = (173.1 \pm 1.3)$ GeV is about 40 times as high as the mass of the $b$-quark

Combining these points leads to the conclusion that the bottom quark and subsequent $B$-hadron from a top quark decay aquire a high boost $\gamma_B$ which is correlated to the mass of the primary top quark. Using basic kinematic calculations the boost $\gamma_B$ can be expressed as

$$\begin{aligned} \gamma_B &\equiv X_\gamma \cdot \gamma_b = X_\gamma \cdot \frac{1}{2} \frac{m_t^2 + m_b^2 - m_W^2}{m_b(E_t - |\vec{p}_t| \cos(\theta_{tb}))} \\ &= X_\gamma \cdot \frac{1}{2} \frac{m_t^2 + m_b^2 - m_W^2}{m_b(\sqrt{m_t^2 + |\vec{p}_t|^2} - |\vec{p}_t| \cos(\theta_{tb}))} , \end{aligned} \tag{5.1}$$

where $\gamma_b$ is the $\gamma$-factor of the parent $b$-quark of the $B$-hadron and $X_\gamma$ describes the transition of the $\gamma$-factor during the hadronization. $X_\gamma$ can be written as

$$X_\gamma \equiv \frac{\gamma_B}{\gamma_b} = \frac{E_B/m_B}{E_b/m_b} = D(x_b) \cdot \frac{m_b}{m_B} , \tag{5.2}$$

where $D(x_b)$ is the fragmentation function of $b$-quarks which describes the momentum fraction $x_b$ that the $B$-hadron retains from its parent $b$-quark. Eq. (5.1) clearly demonstrates the dependance of $\gamma_B$ on $m_t$. Since the boost directly impacts the $B$-hadron's lifetime in the lab system, the top quark mass can be statistically infered to the hadrons averaged lifetime. Rather than measuring the lifetime, one can instead use the mean distance of travel, also referred to as the mean decay length $\langle L_{xyz} \rangle$ of the $B$-hadron, where $L_{xyz}$ is given by

$$L_{xyz}^B = \gamma_B \beta_B c \tau_B = \tau_B \frac{p_B}{m_B} \quad . \tag{5.3}$$

An alternative view is thus that the decay length is depending to the $B$-hadron's kinematics which is strongly correlated to the parent top quark mass. In practice, the transverse component $L_{xy}^B$ is preferably used since the longitudinal component of the $t\bar{t}$ momentum is very unpredictable in proton-proton collisions.

Both $L_{xyz}$ as well as $L_{xy}$ are basically distributed exponentially due to the distributions of the individual hadron lifetimes $\tau_B$. An additional modification to the pure exponential function is due to the presence of $\gamma_B$ which is individual for each $B$-hadron as well. A detailed investigation on the parametrization of the distribution of $L_{xy}$ ass well as on the further parameters is ongoing [84] and is not discussed within the course of this thesis.

The top quark mass can be determined by estimating the mean transverse decay length for different top quark masses $\langle L_{xy} \rangle (m_t)$ using MonteCarlo simulations. The function $\langle L_{xy} \rangle (m_t)$ is called the mass estimator which is shown in a schematic representation in Figure 5.1. In measurements one can then determine $\langle L_{xy} \rangle$ from the distribution of transverse decay lengths and conclude the top quark mass as seen in Figure 5.1. The uncertainty on $m_t$ is obtained from the error band on the mass estimator that is composed of statistic and systematic uncertainties.

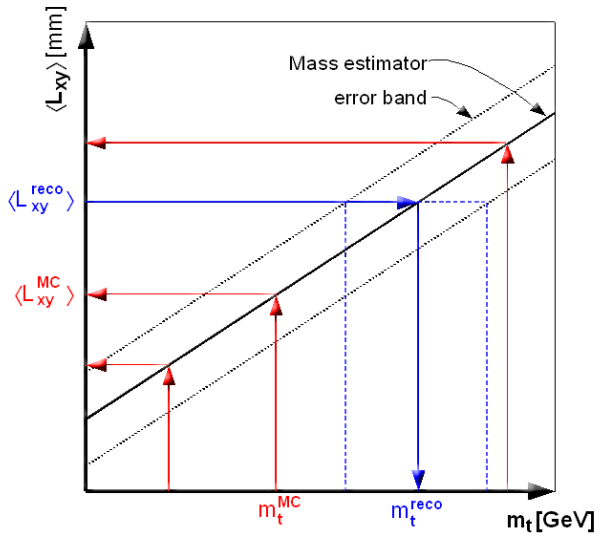


**Figure 5.1:** Schematic view of the mass estimator. The red arrows represent the input from MC Simulations where the mean transverse decay length $\langle L_{xy} \rangle$ is determined for several assumed input masses $m_t$. The blue arrow represents the measurement, where the input of $\langle L_{xy} \rangle$ is obtained from the distribution of transverse decay lengths which is used to deduce the top quark mass. The blue dottet lines represent the uncertainties on $m_t^{\text{reco}}$ which are obtained from the errorband on the mass estimator.

The very advantage of this technique is that the measurement of the decay length in the detector exclusively relies exclusively on tracking as seen in Figure 5.2. The decay length is calculated from measurement data using the spatial distance of the primary vertex of the event and the secondary vertex of the decay of the $B$-hadron. Both vertices can be obtained using the tracks emerging from them as described in section 4.3.2. The decay length method is therefore a promising ansatz as the systematic influences are complementary to those of other mass measurements which mostly rely on the calorimetric reconstruction of jets rather than tracking.

The spatial distance of primary vertex (PV) and secondary vertex (SV) is calculated from their cartesian coordinates $\vec{r}_{\text{PV}}$ and $\vec{r}_{\text{SV}}$ as follows:

$$\begin{aligned} L_{xyz} &= \sqrt{(x_{SV} - x_{PV})^2 + (y_{SV} - y_{PV})^2 + (z_{SV} - z_{PV})^2} \\ &\equiv \left( \sum_{i=1}^{3} \Delta r_i^2 \right)^{\frac{1}{2}} \end{aligned} \tag{5.4}$$

The transverse component is then

$$L_{xy} = \sqrt{\Delta x^2 + \Delta y^2}, \tag{5.5}$$

which is the basic equation in the measurement of transverse decay lengths.

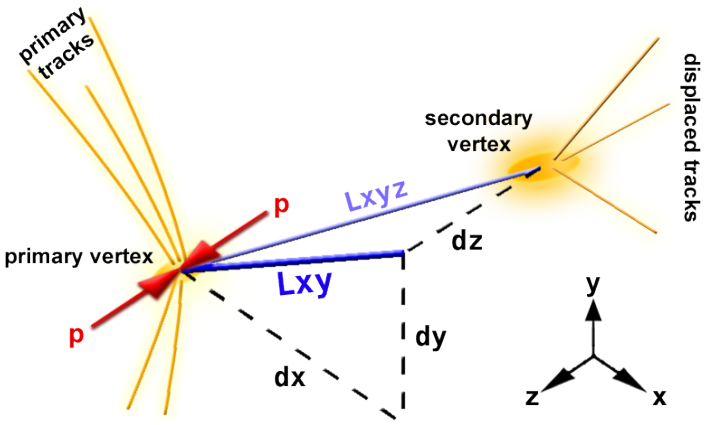


**Figure 5.2:** Schematic representation of the transverse decay length $L_{xy}$ in the detector. The protons that move along the $z$-axis collide at the primary vertex and produce a long-lived $B$-hadron as well as multiple short living states. These states decay instantaneous and produce particles that leave tracks in the detector pointing at the primary vertex, while the long lived particle decays outside of this range and can be identified by a displaced secondary vertex.

Assuming that the primary vertices are perfectly aligned along the $z$-axis, one can approximate $x_{PV} = y_{PV} \approx 0$ and reduced eq. 5.5 to

$$L_{xy} \quad = \quad \sqrt{x_{SV}^2 + y_{SV}^2}. \tag{5.6}$$

This assumption holds as can be seen from the distributions of the primary vertex coordinates shown in Figure 5.3. Here, the distributions of both the MC-Truth vertices as well as of reconstructed primary vertices are shown. For the MCTruth primary vertices the coordinates of the $t\bar{t}$ production obtained from the MCTruth top quarks have been used.

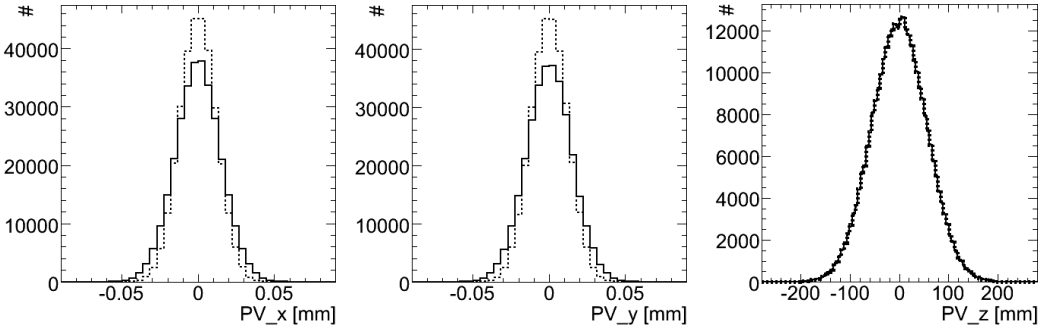


**Figure 5.3:** Primary vertex coordinates $x$, $y$ and $z$ from MCTruth (solid line) and reconstruction (dashed line).

The distributions demonstrate that although the $z$-coordinate is distributed broadly along the beam axis the $x$- and $y$-coordinates are indeed negligible. However one has to keep in mind that the above assumption only holds for the present Monte Carlo data and has to be checked on real data once it is available.

### 5.1.1 Outline of the analysis steps

During the phase of data taking the ATLAS detector will record a large amount of physics events containing a conglomerate of several physics signatures. To filter the fraction of $t\bar{t}$ events from this conglomerate the event selection described in section 4.4 is applied. To identify the decay lengths of $B$-hadrons from top quark decays inside these events the tagging of $b$-jets plays an important role. In a sample of events that pass the $t\bar{t}$ event selection, jets which are identified as $b$-jets are likely to stem from the $b$-quark from the top quark decay. The secondary vertices from these jets therefore provide the coordinates which can be used to determine the $B$-hadron decay length.

To investigate the applicability of the decay length method to ATLAS several analysis steps are taken. In a first step the decay length method is applied on pure semileptonic $(e, \mu)$+jets $t\bar{t}$ events as these are the focus of the studies. This step provides information on the general applicability of the method to ATLAS conditions and allows to study detector and analysis related effects through a comparison with MCTruth information.

The second step is the comparison of the results in the pure $(e, \mu)$+jets signal with those in the full $t\bar{t}$ signal, i.e. taking into account the $\tau$+jets channel, the dilepton channels and fully hadronic channel. This step is important as a large contribution of these events is expected. The contribution of non-semileptonic events is expected to yield comparable results for the decay length distributions as the $b$-jets in these events do not differ from those in the pure signal sample. Hence, they contribute to the signal although they are not intentionally included.

In the third step the background admixture that passes the event selection is included to obtain a final estimate for the measured decay length at ATLAS. Especially the combination of different background samples is of interest as many special cases have to be taken into account, e.g. the single top quark contribution which is partly signal or the different combinations of $W$+jets, $Wcc$ and $Wbb$ which are investigated separately to get a handle on the overlap effects.

The final step is the investigation of systematic uncertainties that arise from the analysis procedure itself as well as from other physics induced effects. All known effects are listet and their influence on the decay length method is discussed. A comparison to other mass measurements is also drawn in this context.

## 5.2 Application of the decay length method to simulated ATLAS data

This section describes the initial application of the decay length method on ATLAS simulation data to obtain a first expectation for the mass estimator. The analysis is based on the MonteCarlo data which was produced for the ATLAS CSC studies. All data is available in the DPD format and the analysis was done using the ROOT analysis framework. The event selection that is applied to the data is described in section 4.4. Whenever scaling factors are used on the samples the target integrated luminosity is 100 $\text{pb}^{-1}$ and eq. (4.3) is used for the calculation.

The mean values presented in the following are weighted arithmetic means which are calculated by the well-known formula

$$\bar{x}_w = \frac{\sum_i^n w_i x_i}{\sum_i^n w_i}\,, \tag{5.7}$$

where $\bar{x}_w$ is the mean of the elements $x_i$, $n = \mathrm{w_{tot}} = \mathrm{w_+}+\mathrm{w_-}$ is the total size of the investigated population and the weights $w_i$ are the event weights $\mathrm{w_+}$ and $\mathrm{w_-}$ which are either $+1$ or $-1$ as described in section 4.1.1. The uncertainty of the mean is then calculated by the also well-known formula

$$\sigma_{\bar{x}_w} = \sqrt{\frac{1}{(\sum_i^n w_i) - 1}} \cdot \sqrt{\frac{\sum_i^n w_i x_i^2}{\sum_i^n w_i} - \left(\frac{\sum_i^n w_i x_i}{\sum_i^n w_i}\right)^2}\,. \tag{5.8}$$

Note that due to the admixture of about 13% $\mathrm{w_-}$ events the error of the mean is underestimated by roughly 16%. This is however not critical in case the underlying population is scaled to represent a luminosity of 100 $\mathrm{pb}^{-1}$, since the size of that population is indeed given by the scaled number of $\mathrm{w_+}-\mathrm{w_-}$.

### 5.2.1 The decay length distributions and the mass estimator of semileptonic $t\bar{t}$ signal events

Figure 5.4 shows the distributions of transverse decay lengths and the mass estimator obtained from the $t\bar{t}$ signal samples 5200, 6203 and 6204 with the simulated top quark masses $m_t^{6203} = 160$ GeV $m_t^{5200} = 175$ GeV and $m_t^{6204} = 190$ GeV. From the available $450 \cdot 10^3$ total events in sample 5200 only a subsample containing $\mathrm{w_+}+\mathrm{w_-} = 100000$ events has been used to fit the available statistics in the samples 6203 and 6204. Only the contributions from the semileptonic $t\bar{t}$ decay channel involving $e$+jets and $\mu$+jets are considered here to investigate a sample that fits to the applied event selection. The distributions have been scaled to represent an integrated luminosity of 100 $\mathrm{pb}^{-1}$. The results for the mean transverse decay lengths, their statistical uncertainties for both the scaled and unscaled sample sizes and the respective scaling factors are listet in Table 5.2. Note that as the scaling factor is $< 1$ the statistical uncertainty of the scaled sample is larger than the respective unscaled uncertainty. Therefore, the unscaled uncertainty is quoted whenever the true statistical power of a result is relevant.

The decay lengths are obtained from the secondary vertex coordinates of the $b$-tagged jets in the sample using eq. (5.6). Due to the event selection each event contains either one or two of these jets. A further selection is applied to the $b$-tagged jets to obtain meaningful values of decay lengths:

- The jet must have a reconstructed secondary vertex. This does not hold for all jets as the secondary vertex reconstruction might fail.

- A reconstructed secondary vertex must be located within the inner layer of the pixel detector. This cut simply truncates the tail of the decay length distribution and is arbitrary. Additionally, the contribution of vertices which are due to interactions with the pixel detector is suppressed by this cut. Note however that secondary vertices that are found inside the beam pipe are still considered. In this study the upper limit for considered decay lengths is chosen to be $L_{xy} < 50$ mm.

Using this requirement an average of usable decay lengths per event in the order of $\approx 1.4$ is found. This number of course depends on the underlying top quark mass and is listet in Table 5.1 for the three masses.

**Table 5.1:** Mean number of usable decay lengths per event. The number is influenced by the $b$-tag requirement of the event selection and by the additional requirements to obtain meaningful values of decay lengths as described in the text.

| $m_t$ [GeV ] | usable decay lengths per event |
|---|---|
| 160 | $1.36 \pm 0.01$ |
| 175 | $1.39 \pm 0.01$ |
| 190 | $1.40 \pm 0.01$ |

An additional feature of the distributions of reconstructed decay lengths is the drop of the distributions in the region $L_{xy} < 2$ mm which is shown in the inlet of Figure 5.4 (a). This drop is due to the inefficiency of the secondary vertex reconstruction in the near-beam region, which is due to the rejection of vertices that are located close to the primary vertex. The mass estimator itself is built from the decay length distributions using their arithmetic means and respective statistical uncertainties.

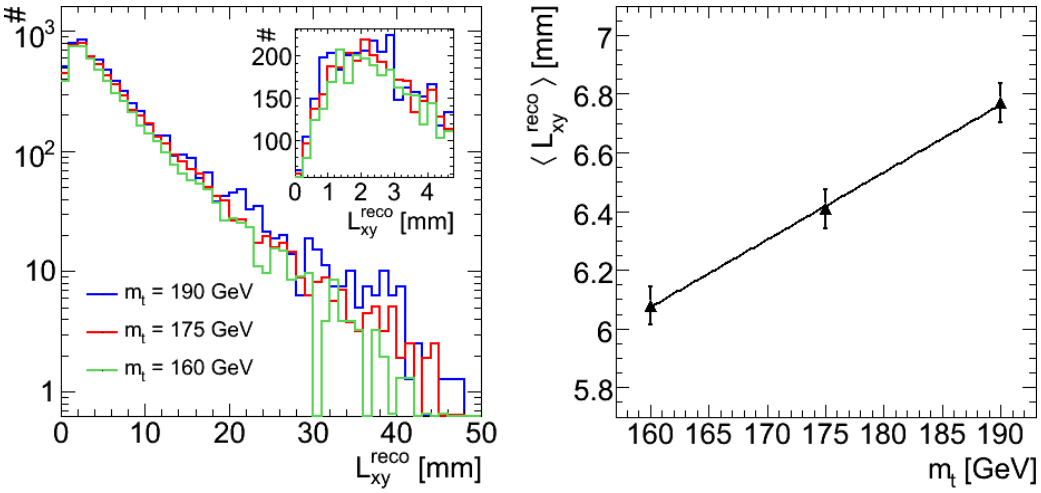


**Figure 5.4:** The decay length distributions of reconstructed $(e, \mu)$+jets $t\bar{t}$ events that pass the event selection (a) and the associated mass estimator obtained from the means of these distributions (b). The inlet in Figur (a) provides a detailed view of the drop of the decay length distributions that is due to the reconstruction algorithm as described in the text. The distributions are scaled to represent a luminosity of $100^{-1}$ pb, while the error bars in the mass estimator represent the unscaled statistical uncertainties. The linear function is obtained from a fit to this data and is described by eq. (5.10).

**Table 5.2:** Mean reconstructed transverse decay lengths for different assumed top quark masses obtained from the $(e, \mu)$+jets channel in $t\bar{t}$ decays.

| $m_t$ [GeV ] | $\langle L_{xy}^{\mathrm{reco}} \rangle$ [mm] | $\sigma_{\langle L_{xy}^{\mathrm{reco}} \rangle}$ stat., scaled | $\sigma_{\langle L_{xy}^{\mathrm{reco}} \rangle}$ stat., unscaled | scaling factor |
|---|---|---|---|---|
| 160 | 6.080 | 0.080 | 0.065 | 0.649 |
| 175 | 6.408 | 0.082 | 0.065 | 0.634 |
| 190 | 6.770 | 0.085 | 0.068 | 0.629 |

The mass estimator demonstrates that the mean values of transverse decay lengths are clearly distinguishable for different masses of the parent top quark. The dependance of $\langle L_{xy}^{\mathrm{reco}} \rangle$ on $m_t$ is obtained from a linear fit on the mass estimator. The interpolation center of the fit is chosen to be $m_t = 175$ GeV using the following parametrization of the fit function:

$$\langle L_{xy}^{\mathrm{reco}} \rangle (m_t) = \text{ slope } [\frac{\mathrm{mm}}{\mathrm{GeV}}] \cdot (m_t - 175 \text{ GeV}) + \text{ constant [mm]}\,. \tag{5.9}$$

In this parametrization the constant represents the absolute scale of the expected mean transverse decay length while the slope describes the dependance of $\langle L_{xy}^{\mathrm{reco}} \rangle$ on the top quark mass around the central point of $m_t = 175$ GeV. The fit to the mass estimator represented by Table 5.2 yields

$$\begin{aligned} \langle L_{xy}^{\mathrm{reco}} \rangle (m_t) &= (2.30 \pm 0.31) \cdot 10^{-2} \frac{\mathrm{mm}}{\mathrm{GeV}} \cdot (m_t - 175 \text{ GeV}) \\ &+ (6.42 \pm 0.04)\,\mathrm{mm} \end{aligned} \tag{5.10}$$

The absolute scale of the mean reconstructed transverse decay length is in found to be in the order of 6.5 mm around a top quark mass of $m_t = 175$ GeV, which is clearly resolvable by the ATLAS detector. The relative statistical uncertainty of $\langle L_{xy} \rangle$in a sample of 100 pb$^{-1}$ can be estimated using the results presented in Table 5.2 to be 1.3 %, which is a satisfying result since this uncertainty will be reduced by far in the long term of the LHC. The dependance of the top quark mass is found to be about 20 $\mu$m per 1 GeV top quark mass.

The mass estimator as described by eq. (5.10) provides a first estimate on the dependance of the mean transverse decay lengths of $t\bar{t}$ signal events on the top quark mass. This number is influenced by several effects like the additional contributions from other $t\bar{t}$ decay channels and background which will be discussed in the following.

### 5.2.2 The decay length distributions and the mass estimator of the combined semi- and dilepton $t\bar{t}$ signal

The influence of an admixture of the previously unconsidered $\tau$+jets and dileptonic $t\bar{t}$ decay channel are expected to yield a mass estimator that is comparable to that of pure $(e, \mu)$+jets channel. The pure dilepton channel alone must however not be taken too serious as the event selection is not designed to fit these channels and therefore provides a lower number of events. To quantify the overall effect the analysis described in section 5.2.1 is repeated on the remaining $\tau$+jets and dileptonic events from the same sample as well as on the complete sample that represents the combined semileptonic and dileptonic channel. Table 5.3 summarizes the results for the mean transverse decay lengths for these analysis and also shows the results from the $(e, \mu)$+jets analysis for comparison. The respective decay length distributions are shown in Figure 5.5. The mass estimators for each signature are compared in Figure 5.6.

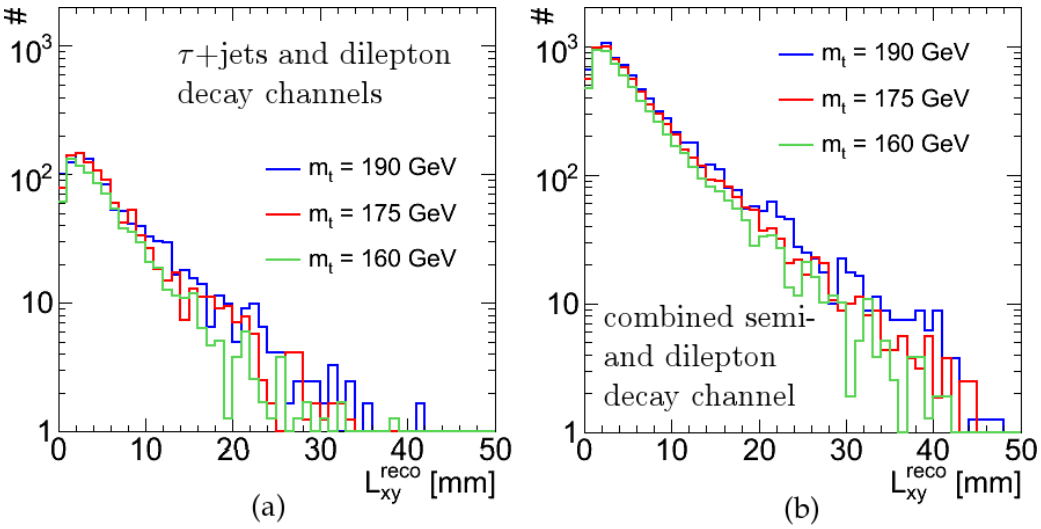


**Figure 5.5:** The decay length distributions for the $\tau$+jets and dilepton events (a) and for the combined semi- and dilepton events (b).

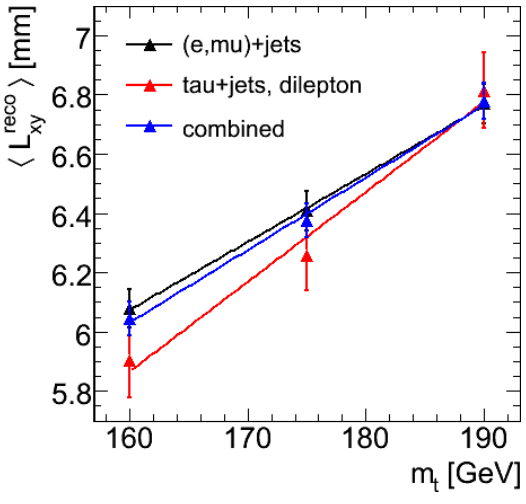


**Figure 5.6:** Comparison of the mass estimators for the $(e, \mu)$+jets channel (black), the $\tau$+jets and dileptonic channel (red) and the combined semi- and dilepton channel (blue).

**Table 5.3:** Comparison of the results for mean transverse decay lengths for $(e, \mu)$+jets channel, the $\tau$+jets and dileptonic channel as well as the combined semileptonic and dileptonic $t\bar{t}$ decay channel. The uncertainties represent the unscaled statistical uncertainties of the mean values which are used as they represent the true statistical power of the sample.

| $m_t$ [GeV ] | $\langle L_{xy}^{\text{reco}} \rangle$ [mm] $(e, \mu)$+jets events | $\langle L_{xy}^{\text{reco}} \rangle$ [mm] $\tau$+jets and $2\ell$ events | $\langle L_{xy}^{\text{reco}} \rangle$ [mm] combined sample |
|---|---|---|---|
| 160 | 6.080 ± 0.065 | 5.90 ± 0.13 | 6.044 ± 0.057 |
| 175 | 6.408 ± 0.065 | 6.26 ± 0.12 | 6.376 ± 0.057 |
| 190 | 6.770 ± 0.068 | 6.81 ± 0.13 | 6.779 ± 0.060 |

For each of these sets the mass estimator is parametrized through a linear fit using eq. (5.9) yielding the parameters listed in Table 5.4.

**Table 5.4:** Parameters of the mass estimators for the results of the different signal sets shown in Table 5.3.

| $t\bar{t}$ decay channel | slope $[10^{-2} \frac{\text{mm}}{\text{GeV}}]$ | constant [mm] |
|---|---|---|
| semileptonic $(e, \mu)$+jets | 2.30 ± 0.31 | 6.42 ± 0.03 |
| $\tau$+jets and dileptonic | 3.03 ± 0.60 | 6.32 ± 0.07 |
| combined semi- and dileptonic | 2.45 ± 0.28 | 6.40 ± 0.03 |

Within their statistic uncertainties the results are found compatible. However note that the results obtained from the $\tau$+jets and dilepton events show a stronger decrease of $\langle L_{xy}^{\text{reco}} \rangle$ with decreasing top quark mass relative to the other samples as seen in Table 5.3 and Figure 5.6. Due to this stronger decrease the slope is systematically higher than for the semleptonic and the combined sample as seen in Table 5.4.

An explanation to this is the very low number of entries in the high $L_{xy}$-range of the decay length distributions which shifts the mean to lower values as seen in Figure 5.5. The reason for the low number of events here is a combination of both the generally lower statistics in this channel and the fact that the distributions are obtained only as a byproduct from the semileptonic event selection. The result from this channel alone is however considered less important since the actual distribution consists of the combined channels. The agreement of the pure $(e, \mu)$+jets and the combined sample demonstrates that the decay length method is indeed independent of the fact that the event selection was not designed to fit all respective topologies. Generally speaking, the $\tau$+jets and dilepton events can be taken into account as signal and are not a background in the common sense.

### 5.2.3 The decay length distributions and mass estimators of the combined signal and background samples

To investigate the influence of physics background on the decay length method the contributions to the background are categorized according to their physics signatures. The categories can be summarized as the $W$+jets background which has to be discussed separately due to the overlap effects of the $W$+jets and the $Wbb, Wcc$ samples and the single top quark as it contains partly signal due to the presence of a $b$-quark that stems from a top quark. Unfortunately the single top quark samples are only available with the central top quark mass $m_t = 175$ GeV so the influence on the mass estimator can only be estimated. The same holds for the fully hadronic $t\bar{t}$ signal sample which is also discussed in this section. A precise investigation of the influence on the mass estimator is discussed only for the $W$+jets samples as they are independent of the top quark mass.

Table 5.5 summarizes the mean transverse decay lengths obtained for each sample using the same event selection and analysis as for the investigation of the pure signal samples. For each sample the uncertainties are listet for both the unscaled sample as well as the for the sample that represents an intergarted luminosity of 100 pb$^{-1}$, which is obtained by applying the scaling factor also listet in the table. The number of $L_{xy}$ entries represents the weighted but unscaled multiplicity of usable decay lengths contributing to the mean and is hence the population on which the mean is based.

Tables 5.6, 5.7 and 5.8 provide an overview of several signal and background combinations that probe the respective influences of the background on the reconstruction of $\langle L_{xy}^{\mathrm{reco}} \rangle$. The signal is to be understand in these tables as the combined semi- and dilepton $t\bar{t}$ decay channel. For the discussion of the fully hadronic channel and single top quark signature only the central sample 5200 with an assumed top quark mass $m_t = 175$ GeV is used for compatibility. The following combinations of signal and background are considered:

- fully hadronic $t\bar{t}$ events in combination with the $t\bar{t}$ signal.
  Although the fully hadronic channel has basically to be considered a signal contribution a very low influence is expected on the overall result.

- the combination of the $t\bar{t}$ signal with $W$+jets, $Wbb$ and $Wcc$.
  These combinations test the influence of the general $W$+jets signature. Also, the overlap effects can be studied through different compositions of these samples.

- the combination of $t\bar{t}$ and single top quark events.
  The comparison of this combinations with the result from the $t\bar{t}$ events allow an estimate of the effect from the special single top signature which in principle is half signal.

- the total combination of all samples.
  This gives an estimate on the expectation of reconstructed decay lengths at ATLAS.

**Table 5.5:** The mean transverse decay lengths for the investigated signal ($m_t$ = 175 GeV) and background samples. The uncertainties of the means are quoted for both the unscaled and scaled populations. The unscaled number of $L_{xy}$ entries contributing to the mean and the scaling factor for an integrated luminosity of 100 pb$^{-1}$ are listet additionally.

| Dataset | Physics content | $\langle L_{xy}^{\mathrm{reco}} \rangle$ [mm] | $\sigma_{\langle L_{xy}^{\mathrm{reco}} \rangle}$ [mm] unscaled | $\sigma_{\langle L_{xy}^{\mathrm{reco}} \rangle}$ [mm] scaled | Number of $L_{xy}$ entries | scaling factor |
|---|---|---|---|---|---|---|
| 5200 | $t\bar{t}$ $(e,\mu)$+jets | 6.408 | 0.065 | 0.082 | 9075 | 0.63 |
| 5200 | $t\bar{t}$ $\tau$+jets and $2\ell$ | 6.26 | 0.12 | 0.15 | 2567 | 0.61 |
| 5204 | $t\bar{t}$ fully hadronic | 6.73 | 0.72 | 0.99 | 79 | 0.53 |
| 6280 | $Wbb + 0$ jets | 5.25 | 0.93 | 1.93 | 28 | 0.26 |
| 6281 | $Wbb + 1$ jets | 5.82 | 0.49 | 0.99 | 173 | 0.25 |
| 6282 | $Wbb + 2$ jets | 5.67 | 0.42 | 0.84 | 250 | 0.25 |
| 6283 | $Wbb + 3$ jets | 6.48 | 0.35 | 0.72 | 360 | 0.24 |
| 6284 | $Wcc + 0$ jets | 5.70 | 1.17 | 3.56 | 8 | 0.10 |
| 6285 | $Wcc + 1$ jets | 4.14 | 0.88 | 2.01 | 32 | 0.21 |
| 6286 | $Wcc + 2$ jets | 6.19 | 0.71 | 2.37 | 106 | 0.10 |
| 6287 | $Wcc + 3$ jets | 6.39 | 0.88 | 2.98 | 90 | 0.10 |
| 8240 | $W \to e\nu + 2$ jets | 3.10 | 0.58 | 0.54 | 21 | 1.12 |
| 8241 | $W \to e\nu + 3$ jets | 5.20 | 1.54 | 1.36 | 27 | 1.27 |
| 8242 | $W \to e\nu + 4$ jets | 5.47 | 0.84 | 0.83 | 58 | 1.03 |
| 8243 | $W \to e\nu + 5$ jets | 3.50 | 0.70 | 0.98 | 47 | 0.52 |
| 8244 | $W \to \mu\nu + 2$ jets | 5.36 | 1.05 | 2.10 | 43 | 0.27 |
| 8245 | $W \to \mu\nu + 3$ jets | 4.18 | 0.58 | 0.75 | 60 | 0.60 |
| 8246 | $W \to \mu\nu + 4$ jets | 4.60 | 0.076 | 0.66 | 32 | 1.29 |
| 8247 | $W \to \mu\nu + 5$ jets | 4.84 | 0.89 | 0.97 | 53 | 0.84 |
| 8248 | $W \to \tau\nu + 2$ jets | 1.49 | 1.03 | 6.72 | 2 | 0.51 |
| 8249 | $W \to \tau\nu + 3$ jets | 3.73 | 1.61 | 1.93 | 4 | 0.77 |
| 8250 | $W \to \tau\nu + 4$ jets | 5.10 | 2.10 | 2.20 | 9 | 0.92 |
| 8251 | $W \to \tau\nu + 5$ jets | 3.03 | 1.96 | 0.83 | 4 | 4.35 |
| 5500 | Single top $Wt$ | 5.89 | 0.16 | 0.36 | 1187 | 0.19 |
| 5501 | Single top s-channel | 6.94 | 0.39 | 2.14 | 313 | 0.04 |
| 5502 | Single top t-channel | 5.67 | 0.23 | 0.33 | 542 | 0.49 |

**Influence of the fully hadronic $t\bar{t}$ decay channel on $\langle L_{xy}^{\mathrm{reco}} \rangle$**

**Table 5.6:** Comparision of the mean transverse decay lengths for the $t\bar{t}$ signal sample (semi- and dilepton channel) combined with the fully hadronic $t\bar{t}$ channel. The uncertainties are not scaled to represent the statistical power of the samples.

| Combination of physics samples | $\langle L_{xy}^{\mathrm{reco}} \rangle$ [mm] |
|---|---|
| $t\bar{t}$ signal | 6.376 ± 0.057 |
| $t\bar{t}$ signal + $t\bar{t}$ fully hadronic | 6.378 ± 0.057 |
| $t\bar{t}$ fully hadronic only | 6.73 ± 0.71 |

The contribution from the fully hadronic $t\bar{t}$ decay channel shown in Figure 5.7 does clearly not provide a significant change to the overall reconstructed mean transverse decay length as seen in Table 5.6. This is due to the very low number of contributing decay lengths as well as to the fact that the fully hadronic channel anyhow provides a signal-like result. Although this cannot be checked on the other top quark masses due to the non-existing samples for the fully hadronic channel, no significant change to this result is expected here. Therefore, the fully hadronic channel will not be considered further in the discussion of the mass estimator.

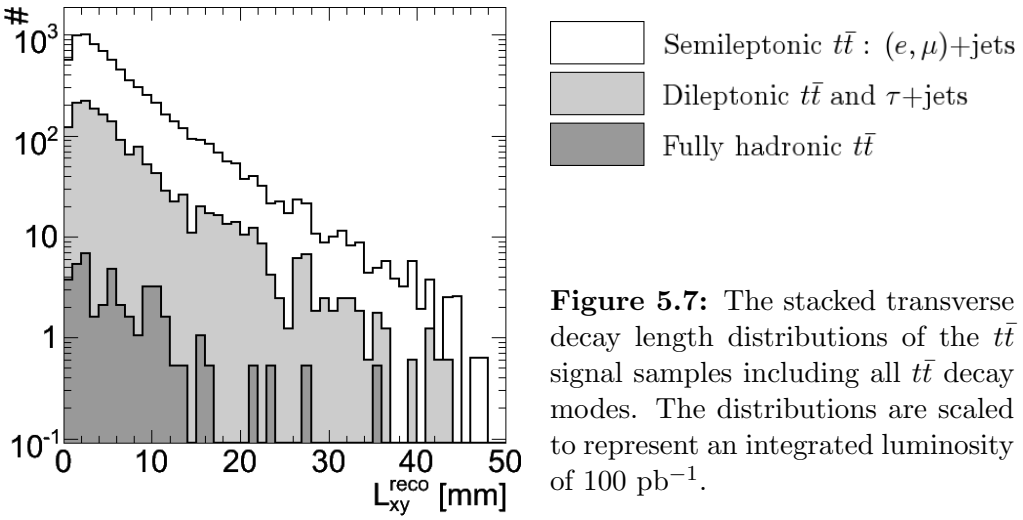


**Figure 5.7:** The stacked transverse decay length distributions of the $t\bar{t}$ signal samples including all $t\bar{t}$ decay modes. The distributions are scaled to represent an integrated luminosity of 100 pb$^{-1}$.

**Influence of single top quark events on $\langle L_{xy}^{\mathrm{reco}} \rangle$**

The mean transverse decay length of the combined single top quark events is expected to yield a slightly lower value than the pure signal events. This can be explained by the presence of an additional $b$-quark in the t-channel and s-channel productions of the single top quark, which is likely to be tagged but contributes with a decay length that is not correlated to the top quark decay. The expectation is confirmed by the result for the lone single top events presented in Table 5.7. The contribution to the distributions of decay lengths single top quarks are shown in Figure 5.8

**Table 5.7:** Comparision of the mean transverse decay lengths for the $t\bar{t}$ signal sample (semi- and dilepton channel) combined with single top quark samples (ST). The uncertainties are not scaled to represent the statistical power of the samples.

| Combination of physics samples | $\langle L_{xy}^{\text{reco}} \rangle$ [mm] |
|---|---|
| $t\bar{t}$ signal | 6.376 ± 0.057 |
| ST only ($Wt$ + t-channel + s-channel) | 5.796 ± 0.142 |
| $t\bar{t}$ signal + $\text{ST}_{Wt}$ | 6.361 ± 0.056 |
| $t\bar{t}$ signal + $\text{ST}_{\text{s-chan.}}$ | 6.377 ± 0.057 |
| $t\bar{t}$ signal + $\text{ST}_{\text{t-chan.}}$ | 6.351 ± 0.056 |
| $t\bar{t}$ signal + $\text{ST}_{Wt}$ + $\text{ST}_{\text{s-chan.}}$ + $\text{ST}_{\text{t-chan.}}$ | 6.339 ± 0.054 |

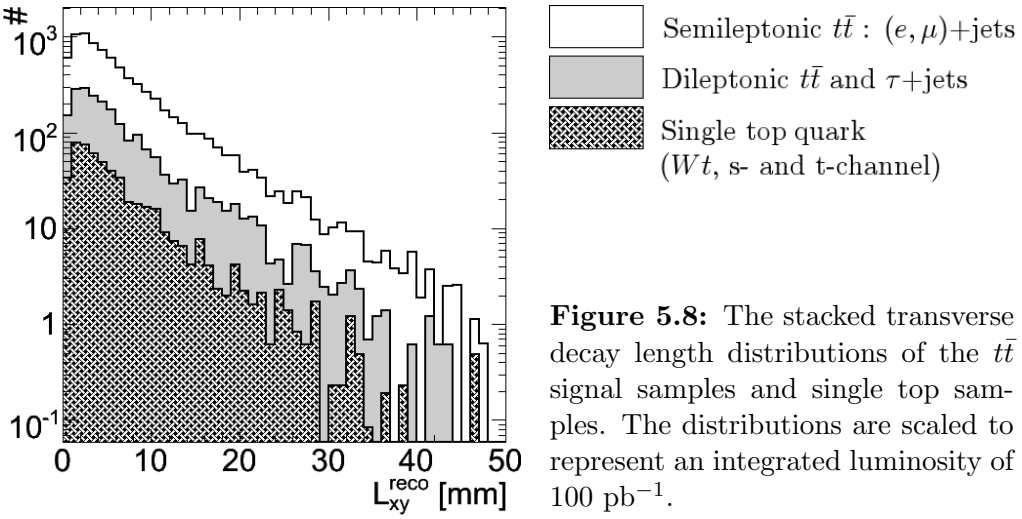


**Figure 5.8:** The stacked transverse decay length distributions of the $t\bar{t}$ signal samples and single top samples. The distributions are scaled to represent an integrated luminosity of 100 $\text{pb}^{-1}$.

Although the result for the combined $t\bar{t}$ and single top quark sample is in very good agreement with the pure $t\bar{t}$ signal, the general trend to lower $\langle L_{xy}^{\text{reco}} \rangle$ is visible in this combination. This trend is however not significant within the available amount of events as seen from the uncertainties of the available statistics in Table 5.7. Also it cannot be checked on the other mass samples as the single top quark events are only available with the central mass. The overall effect on the mass estimator can therefore not be estimated with a sufficient significance at this point.

A sidemark is that the single top quark signature in principle provides the opportunity to do a stand-alone decay length analysis on the $b$-quark from the single top quark, which is however not considered here. Such a study could also provide more information about the nature of the different $b$-quarks appearing there, hence improving the analysis method also for $t\bar{t}$ events.

**Influence of $W$+jets, $Wcc$ and $Wbb$ events on $\langle L_{xy}^{\mathrm{reco}} \rangle$**

**Table 5.8:** Comparision of the mean transverse decay lengths for the $t\bar{t}$ signal sample (semi- and dilepton channel) combined with the $W$+jets, $Wbb$ and $Wcc$ samples. The uncertainties are not scaled to represent the statistical power of the samples.

| Combination of physics samples | $\langle L_{xy}^{\mathrm{reco}} \rangle$ [mm] |
|---|---|
| $t\bar{t}$ signal | 6.376 ± 0.057 |
| $W$+jets only | 4.55 ± 0.34 |
| $Wcc$ only | 5.72 ± 0.49 |
| $Wbb$ only | 6.04 ± 0.23 |
| $Wbb$ and $Wcc$ only | 6.00 ± 0.21 |
| combined $W$+jets, $Wbb$ and $Wcc$ | 5.17 ± 0.23 |
| $t\bar{t}$ signal + $Wbb$ + $Wcc$ | 6.365 ± 0.056 |
| $t\bar{t}$ signal + $W$+jets | 6.303 ± 0.057 |
| $t\bar{t}$ signal + $W$+jets + $Wbb$ + $Wcc$ | 6.294 ± 0.055 |

The several $W$+jets signatures show a clear dependance of the nature of the final state partons on $\langle L_{xy}^{\mathrm{reco}} \rangle$. Here, the $W$+jets samples which contain numerous light jets show the lowest mean value, while the mean inceases over the $Wcc$- and $Wbb$-samples. Due to the nature of the jets involved in these signatures this behavior is expected. Within the combination of $Wcc$ and $Wbb$ the latter is clearly dominating the mean transverse decay length which is also expected.

The mean transverse decay length from the combined signal and $Wcc/Wbb$ samples are compatible within their statistical uncertainties. However the additional contribution from the $W$+jets sample reduces the mean significantly. This is due to the fact that a large fraction of events contribute to the distribution with lower decay lengths than the signal as becomes clear from combining Tables 4.6 and 5.8. To investigate this influence on the overall method the mass estimator is rebuilt taking into account the complete $W$+jets contributions. The results for $\langle L_{xy}^{\mathrm{reco}} \rangle$ or both the pure signal and the combined signal and $W$+jets samples are compared in Table 5.9 and the mass estimators are compared in Figure 5.9. The distribution of transverse decay lengths for the $t\bar{t}$ signal sample with central mass ($m_t = 175$ GeV) and the $W$+jets, $Wcc$- and $Wbb$-samples is shown in Figure 5.10.

**Table 5.9:** The mean transverse decay lengths of the semi- and dileptonic $t\bar{t}$ decay channel only and for the same sample combined with $W$+jets, $Wcc$ and $Wbb$. The uncertainties represent the unscaled statistical uncertainties of the respective parameters.

| $m_t$ [GeV] | $\langle L_{xy}^{\text{reco}} \rangle$ [mm] $t\bar{t}$ signal | $\langle L_{xy}^{\text{reco}} \rangle$ [mm] $t\bar{t}$ and $W$+jets |
|---|---|---|
| 160 | 6.044 ± 0.057 | 5.980 ± 0.056 |
| 175 | 6.376 ± 0.057 | 6.294 ± 0.056 |
| 190 | 6.779 ± 0.060 | 6.678 ± 0.058 |

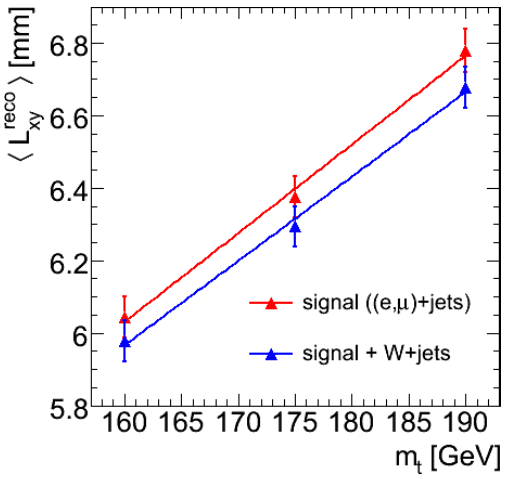


**Figure 5.9:** The mass estimators for the semi- and dilpetonic $t\bar{t}$ decay channel only (red) and for the same sample combined with $W$+jets, $Wcc$ and $Wbb$ (blue). The error bars represent the unscaled statistical uncertainties.

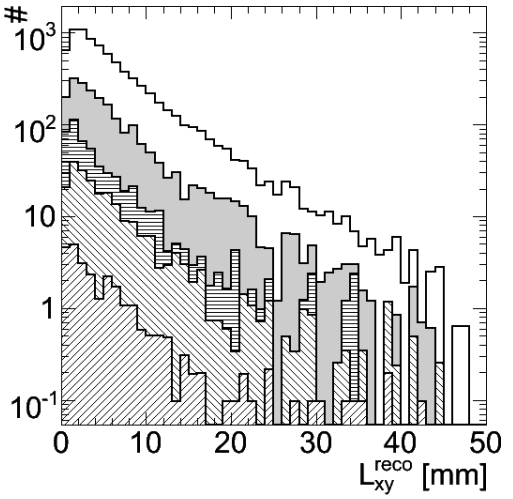


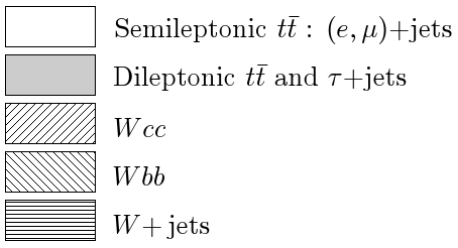


**Figure 5.10:** The stacked transverse decay length distributions of the $t\bar{t}$ signal sample 5200 with the central top quark mass and the $W$+jets samples. The distributions represent an integrated luminosity of 100 pb$^{-1}$.

Both mass estimators are fitted according to eq. (5.9). For the pure signal the result is:

$$\begin{aligned} \langle L_{xy}^{\text{reco}} \rangle (m_t) &= (2.45 \pm 0.28) \cdot 10^{-2} \frac{\text{mm}}{\text{GeV}} \cdot (m_t - 175 \text{ GeV}) \\ &+ (6.40 \pm 0.03) \,\text{mm}\,, \end{aligned} \tag{5.11}$$

while the combined signal and $W$+jets background yields:

$$\begin{aligned} \langle L_{xy}^{\text{reco}} \rangle (m_t) &= (2.33 \pm 0.27) \cdot 10^{-2} \frac{\text{mm}}{\text{GeV}} \cdot (m_t - 175 \text{ GeV}) \\ &+ (6.32 \pm 0.03) \,\text{mm} \end{aligned} \tag{5.12}$$

The mass estimator is found to have a lower slope due to the admixture of $W$+jets events. The constant is also reduced slightly which is due to the change of the absolute scale of the mean transverse decay lengths. The fact that the slope is slightly lower than for the pure signal is due to the nature of the $W$+jets contributions to $\langle L_{xy}^{\text{reco}} \rangle$. While the mean decay lengths from the $t\bar{t}$ signal increase with the top quark mass the contribution of the $W$-boson background remains constant, hence creating a higher impact on decay lengths from increasing top quark masses. Although the overall effect is found to be small within the statistical uncertainties, the trend is clearly visible and has to be taken into account.

**Influence of the overall background on $\langle L_{xy}^{\text{reco}} \rangle$**

The distribution of the overall signal and background combinations is shown in Figure 5.11. For the $t\bar{t}$ signal the usual central mass $m_t = 175$ GeV has been chosen as it is compatible with the single top quark and $t\bar{t}$ fully hadronic sample. The results for the mean transverse decay lengths obtained from the signal and background distributions are compared in Table 5.10

**Table 5.10:** Comparision of the mean transverse decay lengths for the $t\bar{t}$ signal sample (semi- and dilepton channel) combined with the complete background and fully hadronic channel. The background is composed of the single top quark events and the combined $W$+jets, $Wcc$ and $Wbb$ samples. The uncertainties are listet for both unscaled population and for the estimate of the integrated luminosity of 100 pb$^{-1}$.

| Combination of physics samples | $\langle L_{xy}^{\text{reco}} \rangle$ [mm] | $\sigma_{\langle L_{xy}^{\text{reco}} \rangle}$ [mm] unscaled | $\sigma_{\langle L_{xy}^{\text{reco}} \rangle}$ [mm] scaled |
|---|---|---|---|
| $t\bar{t}$ signal | 6.376 | 0.057 | 0.072 |
| background only | 5.52 | 0.13 | 0.18 |
| combined signal and background | 6.267 | 0.053 | 0.067 |

As expected the overall influence of the background follows the same tendency as the sole single top quark and $W$+jets contributions. Taking into account that the contribution from the $W$-boson background is dominating the overall effect on the mass estimator can be assumed to be the same for all top quark masses.

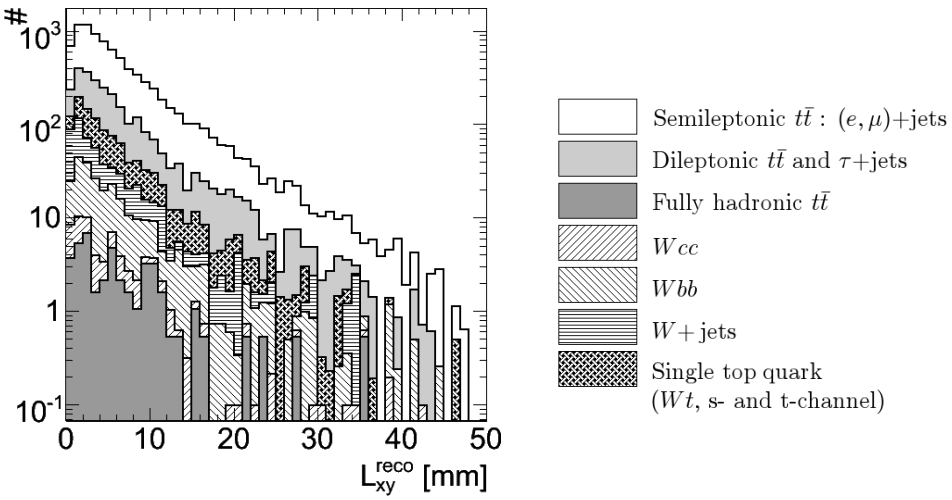


**Figure 5.11:** The distribution of the reconstructed decay lengths for the complete $t\bar{t}$ signal including all three decay channels combined with the single top quark and $W$+jets background. The top quark mass in all samples except $W$+jets is $m_t = 175$ GeV. All distributions are scaled to represent an integrated luminosity of 100 pb$^{-1}$.

Assuming that the effect is comparable to that of the $W$+jets samples the mass estimator is expected to behave the same way, i.e. the slope as well as the absolute scale of $\langle L_{xy}^{\text{reco}} \rangle$ is lowered. To quantify this effect the results from the complete signal and background contributions at the central top quark mass presented in Table 5.10 are rescaled using the mass estimator from the combined signal and $W$+jets samples presented in Table 5.9. The scaling factor is

$$L_i^{\text{S+B}} = \frac{L_{175}^{\text{S+B}}}{L_{175}^{\text{S+W}}} \cdot L_i^{\text{S+W}} \,, \tag{5.13}$$

where $L_i$ represents the mean transverse decay lengths for the top quark mass of index $i = \{160, 190\}$ for either signal+background (S+B) or signal+($W$+jets) only (S+W). The uncertainties $\sigma_{L_i^{\text{S+B}}}$ are obtained from the quadratic addition of the unscaled relative errors of the respective parameters. Table 5.11 presents the results and Figure 5.12 shows the respective mass estimator compared to the signal-only mass estimator.

**Table 5.11:** The estimated mean transverse decay lengths for $m_t = 160$ GeV and $m_t = 190$ GeV. The results are obtained using eq. (5.13). The uncertainties are obtained from the quadratic addition of the unscaled relative errors of the participating parameters.

| $m_t$ [GeV] | $L_i^{\text{S+B}}$ | $L_i^{\text{S+W}}$ | $L_{175}^{\text{S+B}}$ | $L_{175}^{\text{S+W}}$ |
|---|---|---|---|---|
| 160 | 5.954 ± 0.092 | 5.980 ± 0.056 | 6.267 ± 0.053 | 6.294 ± 0.056 |
| 190 | 6.65 ± 0.10 | 6.678 ± 0.058 | ” | ” |

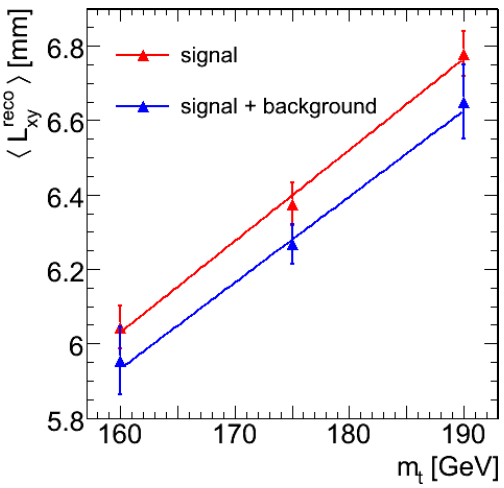


**Figure 5.12:** The mass estimators for the semi- and dilpetonic $t\bar{t}$ decay channel only (red) and for the same sample combined with the total expected background from $W$-boson+jets, single top quarks and the fully hadronic channel. The error bars represent the unscaled statistical uncertainties.

The mass estimator for the complete signal- and background contributions obtained by this estimate is parametrized by a linear fit with the result

$$\begin{aligned} \langle L_{xy}^{\mathrm{reco}} \rangle (m_t) &= (2.31 \pm 0.45) \cdot 10^{-2} \frac{\mathrm{mm}}{\mathrm{GeV}} \cdot (m_t - 175\ \mathrm{GeV}) \\ &+ (6.28 \pm 0.04)\,\mathrm{mm}\,. \end{aligned} \tag{5.14}$$

This mass estimator represents the best possible estimate for the expected function $\langle L_{xy}^{\mathrm{reco}} \rangle (m_t)$ at ATLAS. The systematic uncertainties on this result which are based on the reonstruction algoritms, the background and further physics related effects are discussed in the next section.

## 5.3 Systematic effects and uncertainties

Due to the large statistics of $t\bar{t}$ pairs that will be produced and measured in the long term of the LHC, statistical uncertainties will be small against systematic effects that will affect the top quark mass measurement at ATLAS. For the decay length method a first estimate on the most important systematic uncertainties will be discussed in this section. These uncertainties can be summarized as follows:

- Method and reconstruction inherent effects.
  These systematics stem from the properties of the reconstruction algorithm and the analysis itself and are not directly based on physics effects. However, these effects can be clearly identified through comparison to MCTruth information and do not lead to a numerical uncertainty on the reconstructed top quark mass since the reconstruction is used as is.

- The jet energy scale.
  An estimation of the uncertainty due to the jet energy scale is important with regard to other methods, it this uncertainty is expected to be negligible in the decay length method.

- The jet selection and $b$-tagging.
  Since the decay lengths are obtained from $b$-tagged particle jets both the jet selection as well as the $b$-tagging procedure are expected to reflect on the measured top quark mass.

- The properties of $B$-hadrons.
  The lifetime, mass and fragmentation properties of the $B$-hadrons from top quark decays influence the respective hadrons decay length directly. Therefore, the precision to which these attributes are known reflects on the mass of the parent top quark.

- Initial and final state radiation.
  Gluon radiation from initial and final state partons in proton-proton collisions changes the kinematics of the process as well as the event topology which both has an influence on the measurements of $t\bar{t}$ pairs.

### 5.3.1 Method inherent effects

To study the general analysis inherent effects on the method a comparison with the MCTruth mass estimator for the combined semileptonic and dileptonic $t\bar{t}$ signal sample is performed. Two types of true decay length distributions can be considered, these are the distribution of the complete set of true decay lengths in a sample and the subsample of true decay lengths associated (i.e. matched) to the reconstructed decay lengths. The distinction of these types of decay lengths will provide information on several systematic effects from the reconstruction which affect the method. Precisely the following systematic influences are expected:

- a shift in $\langle L_{xy} \rangle$ due to the drop in the distribution of reconstructed decay lengths in the region $L_{xy} < 3$ mm as seen in Figure 5.4 (a).
  As the distribution of the complete set of true decay lengths is basically given by a (modified) exponential function, the drop in the reconstructed distribution strongly decreases the statistics in the low $L_{xy}$-region with respect to the MCTruth distribution. The mean values obtained from the reconstruction are therefore expected to be higher than those from MCTruth. The slope of the mass estimator should however be comparable as the effect of the reconstruction is the same for all assumed top quark masses.

- an overestimation of $\langle L_{xy} \rangle$ due to the inclusive $b/c$-vertex reconstruction in the BTagVrtSec algorithm as described in section 4.3.2.
  As was shown in Figure 4.6 the distance of the secondary and primary vertices is overestimated due to the inclusive vertex fit. The distribution of reconstructed vertices is therefore expected to be shifted to higher decay lengths with respect to MCTruth. This can be tested by a comparision of the complete set of reconstructed decay lengths and the respective decay lengths from a MCTruth-matched subsample.

- a tilt in the slope of the mass estimator due to the impurity of the $L_{xy}$ population.
  As discussed in section 4.4.5 the impurity on the signal sample, i.e. the number of $b$-tagged jets that do not stem from $B$-hadrons from the top quark decay, is found to be 13.5 %. The impure contributions are expected to have an influence similar to the contributions from the $W$+jets samples as they are inherent background that is not correlated to the top quark mass. This can be tested also by a comparison of the complete signal and the matched subsample.

The distributions of transverse decay lengths for the MCTruth $b$- and $\bar{b}$-quarks from the semileptonic $(e, \mu)$+jets $t\bar{t}$ decay channel as well as the associated mass estimator are shown in Figure 5.13. The respective results are listed in Table 5.12. Note that the statistical uncertainty is lower for this sample as exactly two values of decay lengths are available in the MCTruth information, which provides a higher statistics than the average 1.4 decay lengths on the reconstruction side.

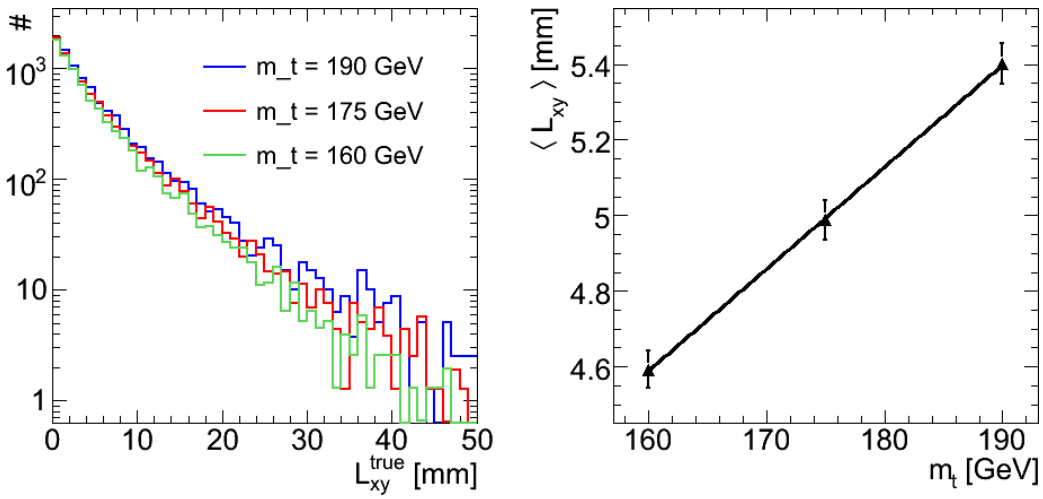


**Figure 5.13:** MCTruth decay length distribution and mass estimator for the semileptonic $(e, \mu)$+jets $t\bar{t}$ decay channel.

**Table 5.12:** MCTruth mean transverse decay lengths for the semileptonic $(e, \mu)$+jets sample. For comparison, the results obtained from the reconstruction of the same sample are also shown. All uncertainties represent the unscaled statistical uncertainties.

| $m_t$ [GeV ] | $\langle L_{xy}^{\text{true}} \rangle$ [mm] | $\langle L_{xy}^{\text{reco}} \rangle$ [mm] |
|---|---|---|
| 160 | $4.593 \pm 0.050$ | $6.080 \pm 0.065$ |
| 175 | $4.988 \pm 0.052$ | $6.408 \pm 0.065$ |
| 190 | $5.402 \pm 0.054$ | $6.770 \pm 0.068$ |

Likewise to the reconstruction the MCTruth decay length distributions are clearly distinguishable for the different top quark masses. As expected the absolute scale of decay lengths is lower due to the absence of the drop in the low $L_{xy}$ region. A detailed representation of this region showing both the MCTruth and reconstructed decay length distributions is given by Figure 5.14. A linear fit to the MCTruth mass estimator yields

$$\begin{aligned} \langle L_{xy}^{\text{true}} \rangle (m_t) &= (2.70 \pm 0.25) \cdot 10^{-2} \frac{\text{mm}}{\text{GeV}} \cdot (m_t - 175 \text{ GeV}) \\ &+ (4.99 \pm 0.03) \,\text{mm} \,. \end{aligned} \tag{5.15}$$

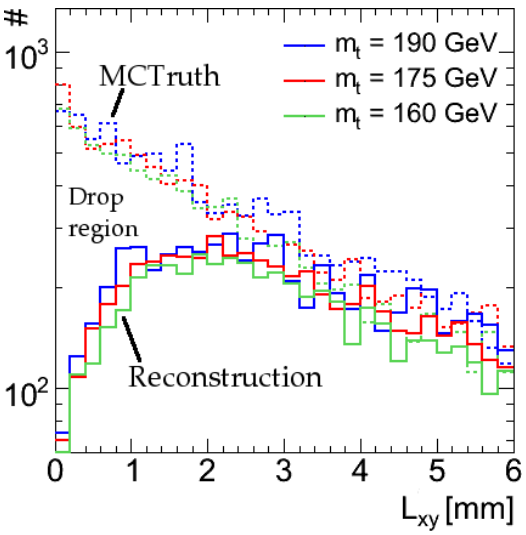


**Figure 5.14:** Detailed view of the region of low decay lengths showing the MCTruth decay lengths (dashed) and reconstructed decay lengths (solid) in comparision. The drop of the reconstruction with respect to MCTruth which causes the shift in the mean between the distributions is clearly visible.

For comparison the parametrization obtained for the reconstruction taken from Table 5.4 is as follows

$$\begin{aligned} \langle L_{xy}^{\text{reco}} \rangle (m_t) &= (2.30 \pm 0.31) \cdot 10^{-2} \frac{\text{mm}}{\text{GeV}} \cdot (m_t - 175 \text{ GeV}) \\ &+ (6.42 \pm 0.03) \,\text{mm} \,. \end{aligned} \tag{5.16}$$

The slope of the MCTruth mass estimator is found to be higher than that of the reconstruction, which is due to the contribution of decay lengths from impure jets on the reconstruction side. This can be demonstrated by compairing the reconstructed decay lengths which are known to stem from true $B$-hadrons from top quark decays to their respective MCTruths decay lengths. These are identified by a $\Delta R$ match where the respective reconstructed jet and the true $b$- or $\bar{b}$-quark have a distance in $R$ which is $\Delta R < 0.2$. This cut is chosen such that either exactly one match or no match at all is found. 54.6 % of all true $b$-jets can be identified in the reconstruction using this matching scheme. Figure 5.15 shows the distributions of reconstructed and respective MCTruth decay lengths as well as the comparison of their mass estimators. The parametrization of the mass estimators yield:

$$\begin{aligned} \langle L_{xy}^{\text{truth match}} \rangle (m_t) &= (2.78 \pm 0.32) \cdot 10^{-2} \frac{\text{mm}}{\text{GeV}} \cdot (m_t - 175 \text{ GeV}) \\ &+ (6.127 \pm 0.039) \,\text{mm} \,. \end{aligned} \tag{5.17}$$

and

$$\begin{aligned} \langle L_{xy}^{\text{reco match}} \rangle (m_t) &= (2.78 \pm 0.34) \cdot 10^{-2} \frac{\text{mm}}{\text{GeV}} \cdot (m_t - 175 \text{ GeV}) \\ &+ (6.691 \pm 0.041) \,\text{mm} \,. \end{aligned} \tag{5.18}$$

The dependance of $\langle L_{xy} \rangle$ on $m_t$ is found to be the same for both $b$-jets from MCTruth as well as for the reconstruction of the true $b$-jets. It is also in agreement with the slope of the mass estimator of the full truth set of decay lengths. This brings up the conclusion that the tilt in the mass estimator of the complete reconstruction is indeed due to the impurities of the investigated set of reconstructed decay lengths. The effect from this admixture is therefore of the same nature as that of the $W$+jets background.

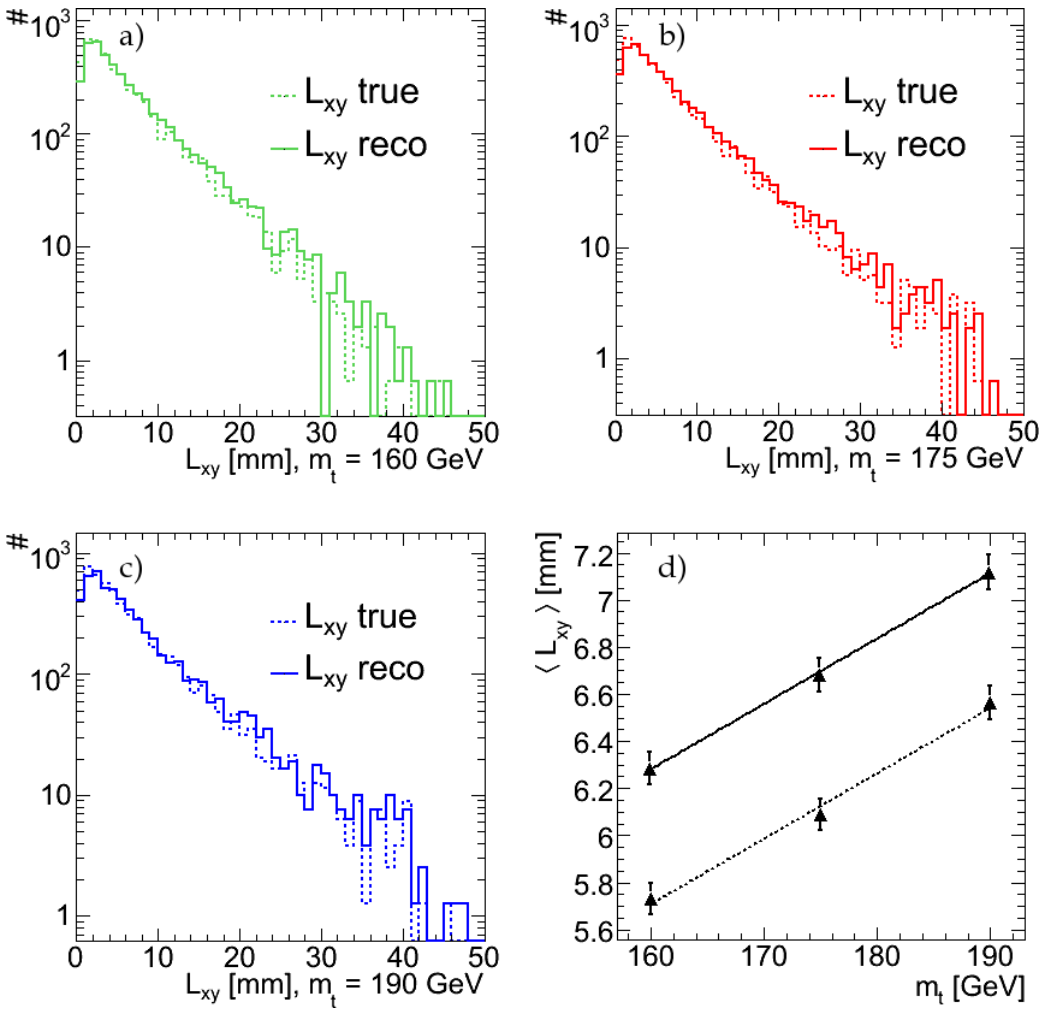


**Figure 5.15:** Comparison of reconstructed and matched MCTruth decay length distributions: a) $m_t = 160$ GeV, b) $m_t = 175$ GeV, c) $m_t = 190$ GeV. c) shows the respective mass estimators obtained from these distributions (solid: reconstruction and dashed: MCTruth).

The overall scale of the mean transverse decay lengths provided by the constant of the mass estimator is found to be different for the set of matched MCTruth decay lengths and for the set of the full MCTruth decay lengths. This is due to the missing drop at low decay length values in the full MCTruth distributions, since the mean is shifted to lower values here. The scale difference in the comparison of the matched reconstruction and MCTruth mass estimators demonstrates that the reconstructed mean transverse decay length is overestimated. This is an effect of the secondary vertex reconstruction which fits an inclusive $b$-/$c$-jet secondary vertex as described in section 4.3.2. Figure 5.16 shows the signed distance $\Delta L = L_{xy}^{\text{reco}} - L_{xy}^{\text{true}}$ for the matched pairs of decay lengths as well as the correlation between them which clarifies this effect.

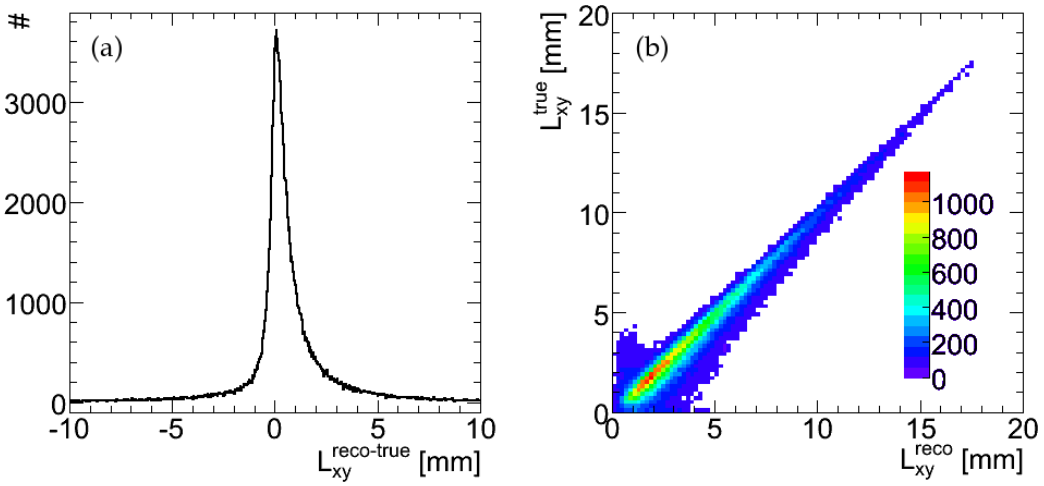


**Figure 5.16:** Distance between reconstructed and MCTruth secondary vertices (a) and the correlation between them (b) for the set of matched MCTruth and reconstructed secondary vertices. It is apparent that the true vertices are overestimated by the reconstruction.

### 5.3.2 The jet energy scale

The jet energy scale plays an important role in most techniques for top quark mass measurement as they mostly rely on calorimetric jet reconstruction. Therefore, an estimate of the uncertainty on $m_t$ due to the jet energy scale is important in these measurements. As already mentioned the decay length method is expected to have complementary uncertainties as it basically relies on tracking. However, the calorimetric jet measurement plays a role in the event selection and therefore has an influence on the method, which can be tested by varying the jet energy scale before the event selection.

Assuming an inital uncertainty of the jet energy scale of 5% [56], the transverse momenta of the jets are changed before the application of the event selection according to

$$p_\perp^{\text{jet}} := p_\perp^{\text{jet}} \cdot \frac{\Delta p_\perp^{\text{jet}}}{p_\perp^{\text{jet}}} \equiv p_\perp^{\text{jet}} \pm 5\% \,. \tag{5.19}$$

Using the modified event selection the mass estimator is rebuilt on the semileptonic $(e, \mu)$+jets $t\bar{t}$ signal samples. The results are listed in Table 5.13.

**Table 5.13:** Parameters of mass estimators obtained from event selections using modified jet energy scales (JES).

| jet energy scale | slope $10^{-2} \cdot \left[\frac{\text{mm}}{\text{GeV}}\right]$ | constant [mm] |
|---|---|---|
| JES−5% | 2.29 ± 0.31 | 6.416 ± 0.038 |
| default JES | 2.30 ± 0.31 | 6.420 ± 0.038 |
| JES+5% | 2.30 ± 0.31 | 6.419 ± 0.038 |

Both slopes and constants of the mass estimators are clearly compatible for all modifications of the jet energy scale. This demonstrates the power of the decay length method with respect to other techniques as the jet energy scale does clearly not influence the measurement of transverse decay lengths. The influence of the jet energy scale is thus assumed negligible within the current estimate of the jet energy scale uncertainty and available statistics. However, future studies on higher statistics and better understanding of the jet energy scale should be considered to identify possible effects.

### 5.3.3 The jet selection

As the transverse decay length is obtained as an attribute of a particle jet, the selection of jets has a great influence on the determination of the mean of these decay lengths. Several effects have to be taken into account which are discussed in the following.

The transverse momentum of a jet $p_\perp^{\text{jet}}$, which is an essential parameter in the event selection, is evidently related to the jet's transverse decay length. In general, an increasing cut on $p_\perp^{\text{jet}}$ is expected to result in a higher mean transverse decay length, as only events with high-$p_\perp$ jets contribute to the decay length distribution. Additionally, an increase of the statistical uncertainty of the mean is expected to the lower statistics at higher cuts.

In the special case of transverse decay lengths obtained from samples with different assumed top quark masses one also has to keep in mind that the $p_\perp^{\text{jet}}$ distribution itself is depending on the underlying top quark mass. This is obvious since a larger kinematic range is available to the daughter particles of the top quark at higher masses $m_t$, which is also the basic argument for the functional capability of the decay length method. The effect of the combined dependancies of $m_t$ and the $p_\perp^{\text{jet}}$ cut on $\langle L_{xy} \rangle$ lead to a significant bias on the mass estimator if the $p_\perp^{\text{jet}}$ cut is not chosen carefully.

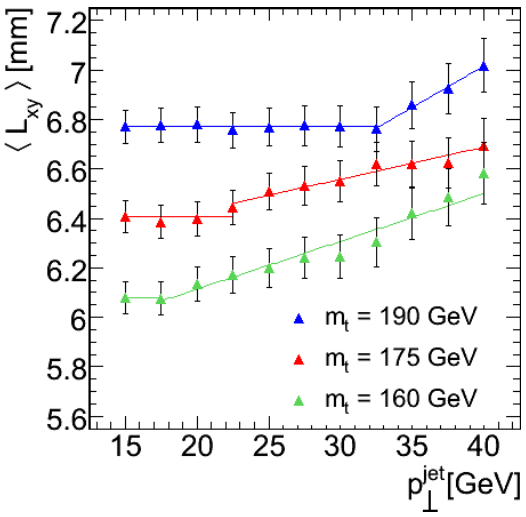


**Figure 5.17:** The mass estimator obtained as a function of the jet $p_\perp^{\text{jet}}$ cut. The regions with negligible dependance of $\langle L_{xy} \rangle$ on ($p_\perp^{\text{jet}}$) are estimated by fitting a constant function to the data.

To demonstrate these effects the mass estimator is investigated as a function of the cut $p_\perp^{\text{jet}}$ which is shown in Figure 5.17. The respective cut for each mass estimator has been applied to the four leading jets during the event selection procedure as described in section 4.4.4. The range of the cut variation is chosen to run from 15 GeV to 40 GeV, which means that the lower bound reflects the jet selection used in this thesis (four jets with $p_\perp^{\text{jet}} > 15$ GeV each) and the upper bound

reflects the default definition from the CSC studies (four jets with $p_\perp^{\text{jet}} > 40$ GeV each). The step width has been chosen to be 2.5 GeV so that on each step the jet requirement was to have four jets with $p_\perp^{\text{jet}} > (15\text{ GeV} + i \cdot 2.5\text{ GeV})$, with $i$ running from 0 to 10. The $b$-tagging cut has been kept constant in each step at $c_b = 6.496$ as defined in eq. (4.12) to be consistent with the analyses presented in this chapter.

Figure 5.17 demonstrates that the dependance of $\langle L_{xy} \rangle$ on the $p_\perp^{\text{jet}}$ cut is lessend for increasing top quark masses. The general trend of this dependance is indicated in the figure by constant and linear fits to the data points of $\langle L_{xy} \rangle (p_\perp^{\text{jet}})$ for each top quark mass. The $p_\perp^{\text{jet}}$-region where the constant can be applied is assumed to exert a minimal influence on the result of $\langle L_{xy} \rangle$. Since this holds only for small cuts on $p_\perp^{\text{jet}}$ which is especially true for the sample with $m_t = 160$ GeV, the cut value used in this thesis has been chosen to be $p_\perp^{\text{jet}} > 15$ GeV to obtain a stable mass estimator. The disadvantage of this cut however is the higher contribution of background events to the decay length distributions which was discussed earlier in this chapter. A possible improvement in future MonteCarlo studies could be obtained by generating $t\bar{t}$ signal samples with a smaller window in $m_t$ around a central mass point $m_t^{\text{current}}$ (173.1 ± 1.3) GeV to increase the region where $\langle L_{xy} \rangle (p_\perp^{\text{jet}})$ is constant. Another possible improvement could be the usage of individual cut values for each jet, which however is not investigated within this thesis.

### 5.3.4 $b$-tagging

The tagging of $b$-jets is another important technique in the application of the decay length method as it selects the jets for the measurement of the transverse decay length. As already mentioned the cut $c_b$ on the jet weight is chosen such that a $b$-tagging efficiency of $\varepsilon_b = 60\%$ is obtained. In section 4.4.5 the $b$-tagging cut for this requirement was determined to be $c_b = 6.496 \pm 0.021$.

To estimate the reflection of this cut on the top quark mass, $c_b$ is modified such that the efficiency is either lowered or increased by an absolute value of $\Delta\varepsilon_b = 3\%$ and the mass estimator is rebuilt using this modified selection criterion. This procedure is standard within the CSC studies and has been widely used to estimate the systematic uncertainty that is due to the usage of $b$-tagging [49]. To avoid further dependancies on the jet selection other than the $b$-tagging, the cut on $p_\perp^{\text{jet}}$ has been kept at the default of this thesis (four jets with $p_\perp^{\text{jet}} > 15$ GeV each) for the reasons discussed in the previous section. The results for the parameters of each mass estimator and the respective $b$-tagging cut are listed in Table 5.14. The mass estimators of the semileptonic $(e, \mu)$+jets $t\bar{t}$ signal samples for both modified and default $b$-tagging cuts are shown in Figure 5.18.

**Table 5.14:** Parameters of mass estimators obtained from event selections using a modified $b$-tagging cut.

| $\varepsilon_b$ [%] | $b$-tagging cut | slope $10^{-2} \cdot \left[\frac{\text{mm}}{\text{GeV}}\right]$ | constant [mm] |
|---|---|---|---|
| 57 | 7.239 | 2.40 ± 0.31 | 6.395 ± 0.038 |
| 60 | 6.496 | 2.30 ± 0.31 | 6.419 ± 0.038 |
| 63 | 5.754 | 2.14 ± 0.31 | 6.470 ± 0.038 |

Comparing the mass estimators it becomes evident that the variation of $\langle L_{xy} \rangle$ as a function of $c_b$ is getting smaller for increasing top quark masses. This variation is used to estimate the uncertainty on the measured $m_t$ by applying these values to the mass estimator function for each top quark mass. The mass estimator is given by eq. (5.10) which fits the investigated $t\bar{t}$ decay mode. The results are summarized in Table 5.15.

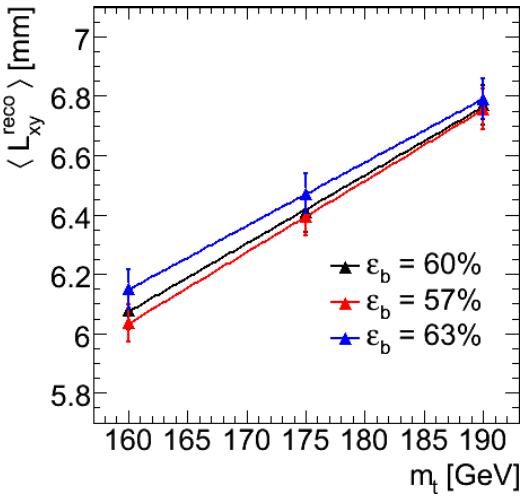


**Figure 5.18:** The mass estimators for the semileptonic $t\bar{t}$ decay channel for $b$-tagging cuts representing the $b$-tagging efficiencies $\varepsilon_b = 60\%$ (black), $\varepsilon_b = 57\%$ (red) and $\varepsilon_b = 63\%$ (blue). The error bars represent the unscaled statistical uncertainties.

**Table 5.15:** Uncertainties $\Delta m_t$ on the top quark mass obtained from a variation of the $b$-tagging.

| simulated $m_t$ [GeV] | $m_t$ according to mass estimator [GeV] $\varepsilon_b = 57\%$ | $\varepsilon_b = 60\%$ | $\varepsilon_b = 63\%$ | $\Delta m_t$ [GeV] |
|---|---|---|---|---|
| 160 | 164.79 | 160.26 | 154.66 | $+4.49/-5.59$ |
| 175 | 178.15 | 174.52 | 171.50 | $+3.62/-3.02$ |
| 190 | 191.50 | 190.24 | 188.33 | $+1.26/-1.92$ |

The relative uncertainty obtained by this method ranges from 3.5% ($m_t$ = 160 GeV) to 0.7% ($m_t$ = 190 GeV), which makes the relative uncertainty on $m_t$ depending on the top quark mass itself. An alternative ansatz is to correct for this effect by extracting the dependance on $m_t$ which can be done by normalizing $\langle L_{xy} \rangle$ to the mass estimator function:

$$\langle L_{xy} \rangle (m_t, c_b) = (\text{slope} \cdot (m_t - 175 \text{ GeV}) + \text{constant}) \cdot f(c_b) \quad (5.20)$$

$$\Leftrightarrow f(c_b) = \frac{\langle L_{xy} \rangle (m_t, c_b)}{\text{slope} \cdot (m_t - 175 \text{ GeV}) + \text{constant}} \quad , \quad (5.21)$$

where $f(c_b)$ is a function which solely depends on the $b$-tagging cut. To study $f(c_b)$ the cut $c_b$ is varied from $c_b = 5.0$ to $c_b = 8.0$ in steps of 0.5 and $f(c_b)$ is obtained from the semileptonic $t\bar{t}$ signal sample using eq. (5.20). The resulting functions $f(c_b)$ for the three top quark masses are shown in Figure 5.19.

As expected $f(c_b)$ shows a similar behavior for each investigated top quark mass. The samples with $m_t = 175$ GeV and $m_t = 190$ GeV are clearly compatible and show an approximately linear dependance of $c_b$. However, the sample with the

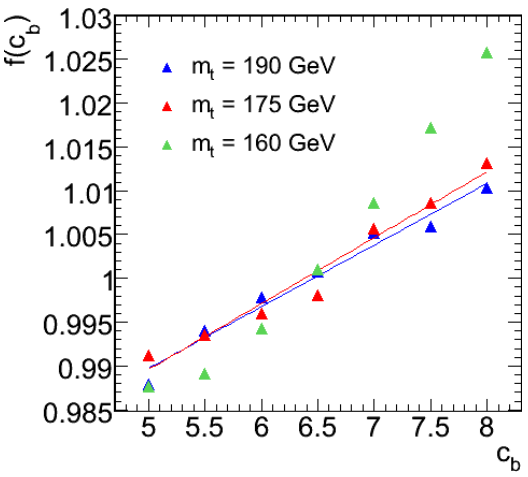


**Figure 5.19:** The function $f(c_b)$ as defined by eq. (5.20) obtained for the $(e,\mu)$+jets $t\bar{t}$ signal samples. For $m_t = 175$ GeV and $m_t = 190$ GeV the function is parametrized using a linear fit.

lowest top quark mass $m_t = 160$ GeV shows a discrepancy to this trend. While still fitting barely to the other samples in the region of low $b$-tagging cuts ($c_b < 6.5$) a strong divergence can be observed in the region of $c_b > 6.5$. Although this effect is not fully understood, it can be assumed that it is correlated to the effect seen in the dependance of the $p_\perp^{\text{jet}}$ cut. On the basis of the good compatibility of $m_t = 175$ GeV and $m_t = 190$ GeV this sample is therefore neglected in the further discussion, however it should be noted that the conclusion may be influenced by methological weaknesses which cannot be studied due to the lack of samples with further top quark masses.

To estimate the uncertainty on the reconstructed top quark mass due to the $b$-tagging the standard CSC procedure is used on the function $f(c_b)$ which now describes the dependance of $\langle L_{xy}\rangle$ on $c_b$ and is independent of the top quark mass. The linear behavior of $f(c_b)$ can be described by a linear fit centered around the value $c_b(\varepsilon_b = 60\%) = 6.496$ :

$$f(c_b) \quad = \quad \text{slope} \cdot (c_b - 6.496) + \text{constant}\,. \tag{5.22}$$

The results of the fits to the data points in the samples with $m_t = 175$ GeV and $m_t = 190$ GeV are summarized in Table 5.16 and their graphical representations are shown in Figure 5.19. The relative degree of dependance

$$R_f = \frac{\Delta f(c_b)}{f(c_b(\varepsilon_b = 60\%))} \quad = \quad \frac{1}{2} \cdot \frac{f(c_b^{\text{high}}) - f(c_b^{\text{low}})}{f(c_b(\varepsilon_b = 60\%))} \tag{5.23}$$

measured at the cut points $c_b^{\text{high}}(\varepsilon_b = 57\%) = 7.239$ and $c_b^{\text{low}}(\varepsilon_b = 63\%) = 5.754$ is used to obtain an estimate on the expected uncertainty on $m_t$. As both dependancies $\langle L_{xy}\rangle(m_t)$ and $f(c_b) \equiv \langle L_{xy}\rangle(c_b)$ are assumed linear in this study, the uncertainty on $m_t$ can be directly derived from the relative uncertainty $R_f$ of $f(c_b)$. The relative uncertainty on the top quark mass due to $b$-tagging obtained by this alternative method is found to be in the order of 0.5 % in the full range of top quark masses. Although it is a great improvement with respect to the previous method, this analysis suffers from the divergence observed on the low $m_t$ sample for which the results should not be regarded as satisfactory. As with the selection of jets by their transverse momenta, future MonteCarlo studies might improve this analysis on the base of a higher variety of available simulated top quark masses.

**Table 5.16:** Parameters of the linear functions $f(c_b)$ for two top quark masses. The respective fits are represented in Figure 5.19.

| $m_t$ [GeV] | slope $10^{-3}$ | constant | $R_f = (\Delta m_t/m_t)$ [%] |
|---|---|---|---|
| 175 | 7.53 ± 0.57 | 1.000 ± 0.001 | 0.54 ± 0.04 |
| 190 | 7.03 ± 0.70 | 1.000 ± 0.001 | 0.52 ± 0.05 |

### 5.3.5 The properties of $B$-hadrons

The intrinsic properties of an individual $B$-hadron have a strong influence on the respective hadron's decay length. In eq. (5.3) the decay length of $B$-hadrons was written as

$$L^B_{xyz} = \gamma_B \beta_B c \tau_B = \tau_B \frac{p_B}{m_B} \quad . \tag{5.24}$$

The properties of $B$-hadrons are thus a potential source of uncertainty to the top quark mass measured in the decay length method. Both lifetimes $\tau_B$ and masses $m_b$ of individual $B$-hadrons bear uncertainties which directly reflect on the hadron's decay length. The momentum $p_b$ is additionally affected by the hadronization process, where the $b$-quark combines with several lighter quarks whereupon their momenta are dispersed among the newly created hadrons. This process is described by the fragmentation function $D(x_b)$ which bears uncertainties to the decay length similar to the other $B$-hadron properties. Using results from investigations on these properties the uncertainty on the top quark mass can be estimated which is discussed in the following.

The masses and lifetimes of all known $B$-hadron species have been measured by several experiments at both LEP and Tevatron colliders. The results of measurements of basic $B$-hadron properties are summarized by the Particle Data Group (PDG) [11] as well as the Heavy Flavor Averaging Group (HFAG) [85]. Table 5.17 provides an overview of the masses and mean lifetimes of the most common $B$-hadrons as obtained by these groups.

**Table 5.17:** Summary of basic properties of common $B$-hadrons. The masses are obtained from the Particle Data Group listings [11] while the lifetimes are obtained from the HFAG [85].

| $B$-hadron type | mass $m_B$ [GeV ] | Mean life $\tau_B$ [ps] |
|---|---|---|
| $B^+/B^-$ | 5279.15 ± 0.31 | 1.639 ± 0.009 |
| $B^0/\overline{B}^0$ | 5279.53 ± 0.33 | 1.530 ± 0.008 |
| $B^0_s$ | 5366.3 ± 0.6 | 1.456 ± 0.030 |
| $\Lambda^0_b$ | 5620.2 ± 1.6 | 1.379 ± 0.051 |

The uncertainty on $m_t$ due to these properties can be estimated from the uncertainties of the dominating $B$-hadrons which are expected for the $t\bar{t}$ decay. An overview of these can be obtained using MonteCarlo simulations. Table 5.18 shows the list of final state $B$-hadrons from the $t\bar{t}$ decay as of the signal sample 5200. The list clearly demonstrates that the hadron families of $B^+/B^-$ and $B^0/\overline{B}^0$ represent the dominating $B$-hadrons, each with a relative occurence of about 40%. The contributions of the more unfrequent $B$-hadron types are neglected in the further discussion due to their rare occurrence.

**Table 5.18:** List of final state $B$-hadrons from $t\bar{t}$ decays a found in the Monte Carlo signal sample 5200. Mesons and baryons are listet separately, each sortet by their relativ occurrence.

| $B$-hadrons from $b$-quarks from top quark decays | | | | $B$-hadrons from $\bar{b}$-quarks from antitop quark decays | | | |
|---|---|---|---|---|---|---|---|
| Hadron type | Quark content | PDG ID | Fraction | Hadron type | Quark content | PDG ID | Fraction |
| $B^-$ | $\bar{u}b$ | -521 | 39,42 % | $B^+$ | $u\bar{b}$ | 521 | 39,78 % |
| $\overline{B}^0$ | $\bar{d}b$ | -511 | 32,86 % | $B^0$ | $d\bar{b}$ | 511 | 33,17 % |
| $B^0$ | $d\bar{b}$ | 511 | 6,59 % | $\overline{B}^0$ | $\bar{d}b$ | -511 | 6,75 % |
| $\overline{B}_s^0$ | $sb$ | -531 | 4,99 % | $B_s^0$ | $\bar{s}\bar{b}$ | 531 | 5,12 % |
| $B_s^0$ | $s\bar{b}$ | 531 | 4,94 % | $\overline{B}_s^0$ | $\bar{s}b$ | -531 | 4,94 % |
| $B^+$ | $u\bar{b}$ | 521 | 0,32 % | $B^-$ | $\bar{u}b$ | -521 | 0,34 % |
| $B_c^-$ | $\bar{c}b$ | -541 | 0,002 % | $B_c^+$ | $c\bar{b}$ | 541 | 0,005 % |
| $\Lambda_b^0$ | $udb$ | 5122 | 6,65 % | $\overline{\Lambda}_b^0$ | $\bar{u}\bar{d}\bar{b}$ | -5122 | 6,04 % |
| $\Sigma_b^+$ | $uub$ | 5222 | 1,2 % | $\overline{\Sigma}_b^+$ | $\bar{u}\bar{u}\bar{b}$ | -5222 | 1,15 % |
| $\Sigma_b^-$ | $ddb$ | 5112 | 0,96 % | $\overline{\Sigma}_b^-$ | $\bar{d}\bar{d}\bar{b}$ | -5112 | 0,94 % |
| $\Xi_b^-$ | $dsb$ | 5132 | 0,83 % | $\overline{\Xi}_b^-$ | $\bar{d}\bar{s}\bar{b}$ | -5132 | 0,75 % |
| $\Xi_b^0$ | $usb$ | 5232 | 0,83 % | $\overline{\Xi}_b^0$ | $\bar{u}\bar{s}\bar{b}$ | -5232 | 0,7 % |
| $\Omega_b^-$ | $bbb$ | 5332 | 0,38 % | $\overline{\Omega}_b^-$ | $\bar{b}\bar{b}\bar{b}$ | -5332 | 0,32 % |

The uncertainty on $m_t$ due to the $B$-hadron lifetimes and masses can thus be estimated from the relative uncertainties of these properties, taking into account only the $B^+/B^-$ and $B^0/\overline{B}^0$ hadron types. While the relative uncertainty on the $B$-hadron mass is in the order of $\sigma_{m_B}/m_B = 0.006\%$ for both $B$-hadron types and can therefore be neglected, the relative uncertainty on the $B$-hadron lifetime provides a significant contribution to the uncertainty of the top quark mass. The relative uncertainties on the lifetimes

$$\sigma_{\tau_B}^{\mathrm{rel}}(B^{\pm}) = \sigma_{\tau_{B^{\pm}}}/\tau_{B^{\pm}} = 0.55\% \quad \text{and} \tag{5.25}$$

$$\sigma_{\tau_B}^{\mathrm{rel}}(B^0) = \sigma_{\tau_{B^0}}/\tau_{B^0} = 0.52\% \tag{5.26}$$

can directly be applied to the top quark mass and translate to an uncertainty which is in the order of in the order of $\Delta m_t \approx 1$ GeV on the scale of $m_t = 175$ GeV.

As the values of $\sigma_{\tau_B}^{\text{rel}}$ are compatible and both hadron types have equal contributions, a worst case estimate can be given by using the lifetime value of the $B^{\pm}$ hadron type since its uncertainty is slightly higher. The precise values for the uncertainties of each of the investigated top quark masses using this estimate are listet in Table 5.19.

**Table 5.19:** Uncertainty estimates $\Delta m_t$ due to the uncertainty of the $B$-hadron lifetime for the three investigated top quark masses.

| $m_t$ [GeV] | $\sigma_{\tau_B}^{\text{rel}}$ [%] | $\Delta m_t$ [GeV ] |
|---|---|---|
| 160 | ” | $\pm$ 0.88 |
| 175 | 0.55 | $\pm$ 0.96 |
| 190 | ” | $\pm$ 1.05 |

Another systematic impact on the top quark mass comes from the hadronization process of the $b$-quark which affects the momentum of the $B$-hadron. The resulting $B$-hadron carries only a fraction $x_b$ of the momentum of the initial quark, which is described by the so-called fragmentation function $D(x_b)$. The distribution of $x_b$ and therefore the fragmentation function has been measured extensively at electron-positron collisions at LEP [86] and parametrizations of $D(x_b)$ have been obtained by several groups [87–90]. For ATLAS simulations the parametrization of Peterson [90] has been used; the distribution of $x_b$ as realized in the $t\bar{t}$ signal sample 5200 is shown in Figure 5.20.

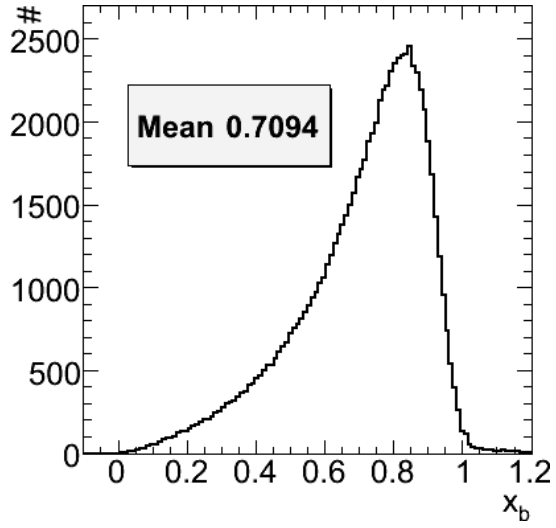


**Figure 5.20:** The distribution of fragmentations $x_b = p_B/p_b$ for the $b$- and $\bar{b}$-quarks from the $t\bar{t}$ decay in the signal sample 5200.

The distribution of fragmentation values $x_b$ is characterized by its mean value $\langle x_b \rangle$. Uncertainties in $x_b$ can therefore be used to estimate uncertainties of $m_t$ in the decay length method. The most precise single measurement of $\langle x_b \rangle$ comes from the OPAL experiment [91]. They present:

$$\langle x_b \rangle = 0.7193 \pm 0.0016\,(\text{stat.})\,^{+0.0038}_{-0.0033}\,(\text{syst.})\,. \tag{5.27}$$

As with the $B$-hadron lifetime, the relative uncertainty on $\langle x_b \rangle$ directly translates to an uncertainty of $m_t$. Adding the statistical and systematic uncertainties in quadrature one obtains

$$\langle x_b \rangle = 0.7193^{+0.0041}_{-0.0036}\,, \tag{5.28}$$

which translates in a maximum relative uncertainty of $\sigma^{\text{rel}}_{\langle x_b \rangle} = 0.57\%$. For an assumed top quark mass in the order of 175 GeV this results in a systematic uncertainty of $\Delta m_t \approx 1$ GeV. The detailed values for the three investigated top quark masses are summarized to Table 5.20.

**Table 5.20:** Estimates on the uncertainty $\Delta m_t$ due to the fragmentation of $b$-quarks for the three investigated top quark masses.

| $m_t$ [GeV] | $\sigma^{\text{rel}}_{\langle x_b \rangle}$ [%] | $\Delta m_t$ [GeV ] |
|---|---|---|
| 160 | ” | $+0.91/-0.80$ |
| 175 | $+0.57/-0.50$ | $+1.00/-0.88$ |
| 190 | ” | $+1.08/-0.95$ |

### 5.3.6 Initial and final state radiation

The radiation of gluons from initial and final state particles, also called initial and final state radiation (ISR/FSR), changes the kinematics of the top quark decay and of their subsequent $B$-hadrons. Figure 5.21 shows examples of possible configurations of initial and final state radiation in the production and decay of top quarks.

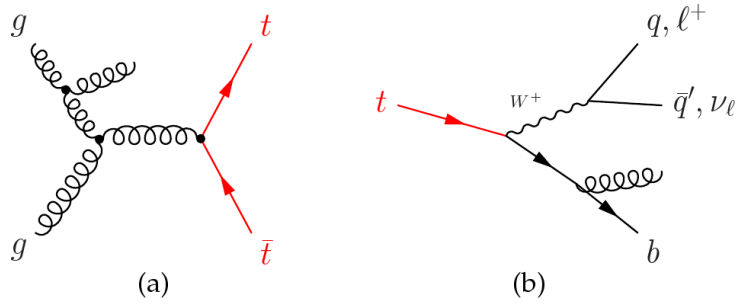


**Figure 5.21:** Examples of the occurence of initial and final state radiation in top quark events. Figure (a) shows intial state radiation in the production of a $t\bar{t}$ pair, Figure (b) shows the emmission of a gluon from the final state $b$-quark in the top quark decay.

The presence of ISR and FSR therefore influences the mean transverse decay length that is obtained from these $B$-hadrons. The uncertainty on $\langle L_{xy} \rangle$ due to initial and final state radiation is estimated using the $t\bar{t}$ signal samples with modified $\Lambda_{\text{QCD}}$.

Figure 5.22 shows the distributions of transverse decay lengths for the three $t\bar{t}$ signal samples with modified values of $\Lambda_{\mathrm{QCD}}$ as defined in section 4.1.5. The results obtained for $\langle L_{xy} \rangle$ are summarized in Table 5.21.

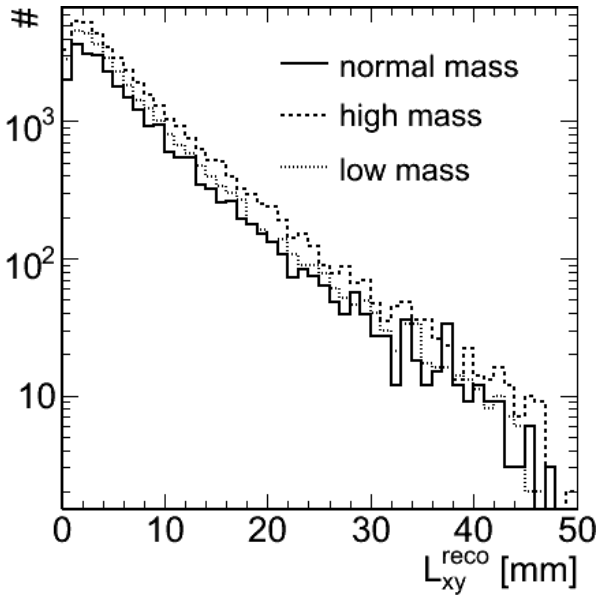


**Figure 5.22:** Distributions of transverse decay lengths obtained from the $t\bar{t}$ signal samples with modified $\Lambda_{\mathrm{QCD}}$. All distributions are scaled to represent an integrated luminosity of 100 $\mathrm{pb}^{-1}$ pb. Note that the combined semi- and dilepton channel is shown.

**Table 5.21:** Mean transverse decay length results for the combined semi- and dilepton $t\bar{t}$ signal samples with modified $\Lambda_{\mathrm{QCD}}$. For reference, the result for the default $t\bar{t}$ signal sample 5200 (MC@NLO, $m_t = 175$ GeV) is also shown. The uncertainties represent the unscaled statistical uncertainties on the results.

| Sample | $\langle L_{xy} \rangle$ [mm] |
|---|---|
| 'low mass' (6251) | 5.968 ± 0.033 |
| 'normal mass' (5205) | 6.179 ± 0.038 |
| 'high mass' (6250) | 6.317 ± 0.031 |
| default $t\bar{t}$ signal (5200, MC@NLO) | 6.376 ± 0.057 |

The general trend as observed within the CSC studies using $\chi^2$ fit method [49] regarding the bias of the results to higher and lower top quark masses is confirmed by this method. An overall conclusion is however considered difficult for both the $\chi^2$ method as well as the decay length method for several reasons that are mainly related to the investigated samples:

- The default samples for $t\bar{t}$ analyses and the samples for studies on initial and final state radiation have been created using different MonteCarlo generators. This reflects especially in the total scale of $\langle L_{xy} \rangle$ which is found to be approximately 2 mm lower than in the signal sample 5200 which was produced with MC@NLO.

- For technical reasons the events in the ISR/FSR samples can not be distinguished with respect to their $t\bar{t}$ decay channel. Although this effect should be covered by the event selection, one must keep this in mind when using these samples as an estimate for uncertainties on the pure semileptonic channel.

- The choise of the production parameters, i.e. the modification of the $\Lambda_{\mathrm{QCD}}$ values, is rather arbitrary. Although it has been tried to minimize the radiation effects on either the ISR or FSR side while maximizing it on the other, it is not possible to study the effects separately, i.e. with an unmodified $\Lambda_{\mathrm{QCD}}$ value on either side. Additionally, further samples with different variations of $\Lambda_{\mathrm{QCD}}$ might also improve the estimate of systematics.

The study of initial and final state radiation effects on $m_t$ must therefore be regarded preliminary. To estimate the uncertainty on $m_t$ a common strategy has thus been defined for the CSC studies [49]. To quantify this estimate the relative difference of the high and low mass results is used in relation to the reference sample. For the decay length method this is given by

$$\frac{\Delta m_t}{m_t} = 0.5 \cdot \frac{L_{xy}^{\mathrm{high}} - L_{xy}^{\mathrm{low}}}{L_{xy}^{\mathrm{normal}}} \quad = \quad 0.5 \cdot \frac{0.349 \text{ mm}}{6.179 \text{ mm}} \equiv 2.82\% \quad . \tag{5.29}$$

This translates into an absolute uncertainty on an assumed top quark mass $m_t = 175$ GeV of about $\Delta m_t \approx 5$ GeV; the detailed results for the three investigated top quark masses are listed in Table 5.22. The influence of initial and final state radiation therefore yields the strongest uncertainty on the top quark mass with respect to all previous discussed effects.

**Table 5.22:** Estimates on the uncertainty $\Delta m_t$ due to the fragmentation of $b$-quarks for the three investigated top quark masses.

| $m_t$ [GeV] | $\sigma_{\mathrm{ISR/FSR}}^{\mathrm{rel}}$ [%] | $\Delta m_t^{\mathrm{abs}}$ [GeV ] |
|---|---|---|
| 160 | ” | $\pm$ 4.51 |
| 175 | 2.82 | $\pm$ 4.94 |
| 190 | ” | $\pm$ 5.36 |

Improvements on the estimate of initial and final state radiation uncertainties will be achieved in future MonteCarlo studies that provide more sets of parameters to effectively investigate the uncertainty on top quark mass measurements. This has been demonstrated in LHC estimates done by the CDF group which showed that the systematic uncertainty of ISR and FSR on the decay length method can easily be reduced to the order of $\Delta m_t = 1.3$ GeV and lower [83]. Here, the level of ISR and FSR is estimated from the observed jet multiplicity which, in case of the Tevatron results, can be compared to that of real data.

Another possibility to investigate especially the effects of initial state radiation is to study the momenta of lepton pairs produced in Drell-Yan processes as shown in Figure 5.23.

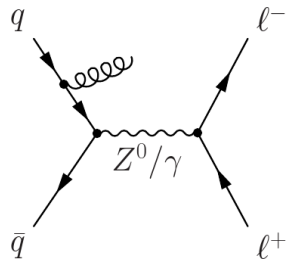


**Figure 5.23:** Example of a Feynman diagram for the lepton pair production in a Drell-Yan process involving initial state gluon radiation. The level of ISR activity can be determined through the measurement of the lepton kinematics.

These momenta are sensitive to the amount of initial state radiation as is obvious from the figure, with the additional advantage that no final state radiation is present. This ansatz has been studied in the context of the template method for top quark mass measurement at CDF [50]. They found that the level of ISR shows a logarithmic dependence on the Drell-Yan mass squared as shown in Figure 5.24. By extrapolation to the scale of the top quark mass the level of ISR at this scale can be obtained. This information can be used as an input for further MonteCarlo studies on the respective mass measurement. Using this method CDF obtains a systematic uncertainty for the template method of $\Delta m_t = +0.4/-0.6$ GeV which is an acceptable scale. However, estimates for ATLAS using these analyses are still pending.

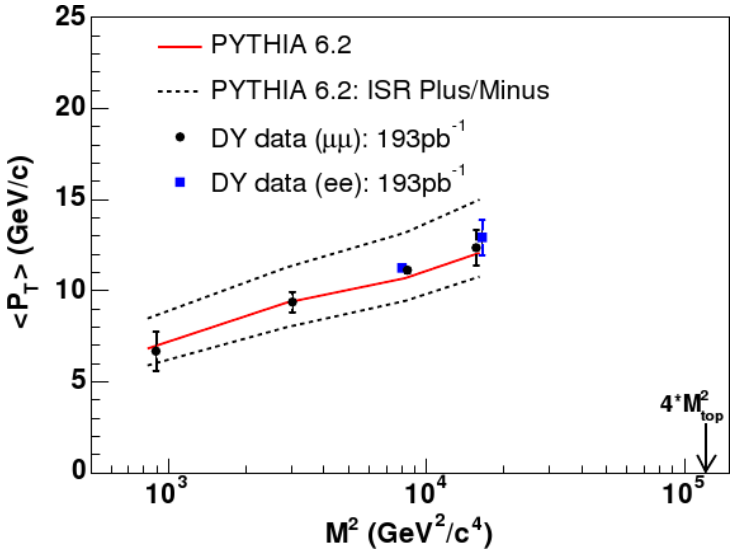


**Figure 5.24:** MonteCarlo simulations of the average transverse momentum of lepton pairs from Drell-Yan productions which corresponds to the level of ISR activity. A logarithmic dependance on the dilepton invariant mass squared $M^2_{\ell\ell}$ is observed. The initial state radiation level was varied in the $\pm 1\sigma_{\mathrm{ISR}}$ level [50].

### 5.3.7 Further uncertainties

The uncertainties that have been discussed in the past sections represent the most influencial effects on the measurement of $m_t$. Other uncertainties that have not been fully investigated in this thesis come from PDF uncertainties and QCD multijet background.

The uncertainties of the parton distribution functions impact the production of the $t\bar{t}$ pair in different ways. A precise knowledge of the fraction of partons that participate in the $t\bar{t}$ production is required to accurately model the hard process in a MonteCarlo event generation. While on the one hand this implies uncertainties on the measurement of the $t\bar{t}$ production cross section, the kinematic influence on the process is assumed small, especially in comparison to the effect from initial and final state radiation [49]. To study the influence of PDF uncertainties the PDF reweighting technique can be used [92]. This technique makes use of the fact that a change in the kinematics as well as in the contribution to the cross section can be described by assigning each event a weight which is calculated from the uncertainty of the PDF that was used for the generation of that event. This weight is defined such that the contribution of the event is evaluated for the case that a modified PDF would have been used, where the modification is described by a error set $PDF'$ to the given parton distribution function $PDF$. An analytical expression for the new weight $w_{\text{reweight}}$ is given by:

$$w_{\text{reweight}} = \frac{PDF(f_1, x_1, Q) \times PDF(f_2, x_2, Q)}{PDF'(f_1, x_1, Q) \times PDF'(f_2, x_2, Q)} \,. \tag{5.30}$$

Here, $f_1$ and $f_2$ are the partons contributing to the respective hard process with momentum fractions $x_1$ and $x_2$. The calculation of the momentum transfer $Q$ is depending on the chosen generator and physics process; for $t\bar{t}$ events generated with MC@NLO it is given by [93]:

$$Q^2 = m_t^2 + \frac{1}{2}\left(p_\perp^2(\text{top 1}) + p_\perp^2(\text{top 2})\right) \,. \tag{5.31}$$

For the measurement of the top quark mass this technique is going to be applied on future MonteCarlo studies. Up to this point, the PDF uncertainty is assumed negligible for all top quark mass measurements, especially concerning the dominating influence from initial and final state radiation.

Another uncertainty comes in due to the presence of QCD events, which can be subdivided in QCD charm production ($\sigma_c^{\text{tot}} \approx 7.8$ mb) [94], QCD bottom production ($\sigma_b^{\text{tot}} \approx 0.5$ mb) [94] and light-quark multijet QCD events ($\sigma_{\text{multi}}^{\text{tot}} \approx 1$ mb) [65]. While the latter events are easily suppressed by the usage of $b$-tagging, the heavy quark events are likely to contribute to the background. In such events the possibility to create a fake lepton from what was originally a hadronic jet can create a signature which is similar to that of semileptonic $t\bar{t}$ events. While events with real leptons that imitate the $t\bar{t}$ signature ($W$+jets) have been investigated in this thesis, events with fake leptons were not discussed as it is difficult to accurately simulate such events, which is due to their widely varying event topologies as well as the enormously high statistics needed for their investigations. In general, such events are not expected to provide a large impact on the $t\bar{t}$ selection due to the complex event selection criteria that are applied to the data. These criteria involve strict rules for high-$p_\perp$ leptons which are isolated, combined with strong additional cuts on $\not\!\!E_\perp$ and the jet momenta. Additionally, the fake rate for leptons in the

beginning phase of ATLAS is estimated to be in the order of 0.1 % [80,81], making such contributions less probable. The exact level of these events however needs still to be estimated, first attempts to this using a data driven way have been performed recently [93].

## 5.4 Conclusion on the decay length method

The studies on simulated ATLAS top quark events demonstrate that the decay length method for top quark mass measurement is applicable to ATLAS. With an overall scale of about 6.5 mm the mean transverse decay length has proven to be a suitable obserable. Since the decay length is measured from the distance between primary and secondary vertices, the large order of magnitude of $\langle L_{xy} \rangle$ ensures a good separability of these vertices which should hold even in a high-densitiy track environment like the ATLAS experiment. The statistical uncertainty on $\langle L_{xy} \rangle$ in a scenario with a collected integrated luminosity of 100 pb$^{-1}$ is estimated to be in the order of 1.3 %. In the long term of the LHC data taking this uncertainty will be reduced further so that the decay length method is clearly dominated by systematic uncertainties.

### 5.4.1 Summary and discussion of systematic uncertainties

The determination of the top quark mass from the measurement of the mean transverse decay length of $B$-hadrons in $t\bar{t}$ events is prone to several systematic uncertainties of which the most important have been estimated in the MonteCarlo studies presented in this chapter.

Apart from general reconstruction and object selection effects which do not directly reflect on the measured top quark mass, the most important influences on $m_t$ come in due to $b$-tagging, the properties of $B$-hadrons and initial and final state gluon radiation.

Other systematic influences that have been studied include background, the jet energy scale and the jet selection. In particular the uncertainty on the jet energy scale is worth mentioning since in contrast to other top quark mass measurements the influence on the measured $m_t$ is found to be negligible.

The influence due to the jet selection has been minimized by the usage of a soft cut on the jet transverse momentum. This was done to eliminate a bias on the measured mean transverse decay length which was found to be an effect of both the cut itself and the investigated parent top quark mass. Due to the low cut on the jet momentum a significant amount of background was also found to participate to the investigated decay length distributions. However, the presence of this background does not affect the overall functionality of the decay length method and can be included directly in the estimate for the expected mean transverse decay lengths at ATLAS.

A summary of the first estimates of systematic uncertainties is for the inital usage of the decay length method found in Table 5.23.The estimates are presented for the three assumed top quark masses that have been investigated in this thesis; however note that the central value of $m_t = 175$ GeV bears the significant uncertainties with respect to its proximity to the actual top quark mass. The total sum of the uncertainty of each top quark mass at the end of the table is calculated by adding the individual uncertainties in quadrature.

**Table 5.23:** Summary of the first estimates of systematic uncertainties on the top quark mass measured with the decay length method.

| systematic uncertainty | $\Delta m_t$ [GeV] $m_t = 160$ GeV | $m_t = 175$ GeV | $m_t = 190$ GeV |
|---|---|---|---|
| $b$-tagging | $+4.49/-5.59$ | $+3.62/-3.02$ | $+1.26/-1.92$ |
| jet energy scale | negligible | negligible | negligible |
| $B$-hadron lifetime | $\pm 0.88$ | $\pm 0.96$ | $\pm 1.05$ |
| $b$-fragmentation | $+0.91/-0.80$ | $+1.00/-0.88$ | $+1.26/-0.95$ |
| ISR/FSR | $\pm 4.51$ | $\pm 4.94$ | $\pm 5.36$ |
| **total** | $+6.49/-7.28$ | $+6.27/-5.93$ | $+5.74/-5.87$ |

It is obvious that the uncertainty is dominated by the estimates for $b$-tagging and initial and final state radiation. While the $b$-tagging estimate might be improved in future studies to a relative uncertainty of about 0.5% on $m_t$ by separating the top quark mass dependance (section 5.3.4), the initial and final state radiation uncertainty remains problematic and needs further investigation with possible alternative studies. Apart from these strong influences the $B$-hadron properties contribute with an uncertainty of $\Delta m_t \approx 1$ GeV, which is an acceptable level for a first estimate.

The power of the decay length method is its complementarity to other methods with respect to the systematic uncertainties. The estimates for the studies on the $\chi^2$ minimization, which provides the basics for other methods and has been extensively studied in the CSC context, are shown for comparison in Table 5.24. Both studies are comparable with respect to the investigated samples and have a mostly identical event selection, note however that no $b$-tagging was performed in the application of the $\chi^2$ method for which they do not quote uncertainties on this technique.

**Table 5.24:** Comparison of the systematic uncertainty estimates for the $\chi^2$ minimization and the decay length method.

| systematic uncertainty | $\Delta m_t$ [GeV] @ $m_t = 175$ GeV $\langle L_{xy} \rangle$ | $\chi^2$ minimization |
|---|---|---|
| $b$-tagging | $+3.62/-3.02$ | n.a. |
| jet energy scale | negligible | 3.5 |
| $B$-hadron lifetime | $\pm 0.96$ | n.a. |
| $b$-fragmentation | $+1.00/-0.88$ | 0.1 |
| ISR/FSR | $\pm 4.94$ | 0.3 |
| **total** | $+6.27/-5.93$ | 3.5 |

It is clear that the overall scale of the $\chi^2$ minimization method presents a more acceptable scale of uncertainty since the decay length method is still in a stage of infancy. Yet, it is obvious that the ucertainties are complementary in the direct comparison. Especially the strong impact of the jet energy scale in the $\chi^2$ method is striking to note. Additionally it has to be mentioned that the $\chi^2$ method might suffer from additional uncertainties which have enot been fully evaluated during the CSC studies; these uncertainties include $b$-tagging which can also be applied to the $\chi^2$ method as well as combinatorial background. A general remark is that apart from the initial and final state radiation most uncertainties on the decay length method are acceptable for a first estimate as it is presented here. This includes also the $b$-tagging for which an estimation technique has been proposed that might reduce the uncertainty quoted in Table 5.24 down to a relative uncertainty of 0.5% on $m_t$.

### 5.4.2 Future improvements of the method

Possible improvements on the estimates of systematic uncertainties have been proposed in the discussions of the respective uncertainties and shall be briefly summarized here.

The most important uncertainty is due to initial and final state radiation which can be further investigated by studying Drell-Yan processes, since the respective lepton momentum is depending on the level of initial state radiation. This study is strongly suggested since other methods will also benefit from the results. An alternative improvement can be achieved by simulating $t\bar{t}$ events with further parameter variations on ISR and FSR. These new samples allow complementary estimates by using for example the jet multiplicity to estimate the ISR and FSR level from real data.

Another impact comes from the usage of $b$-tagging and the selection of jets. Here, the simulation of additional assumed top quark masses at higher statistics will provide a major improvement through the investigation of the dependance of $\langle L_{xy} \rangle$ on both the $p_{\perp}^{\text{jet}}$ cut and the $b$-tagging cut. An important step will be the study of the mass estimator on top quark masses which are distributed in a narrower region around the central value of $m_t$, which should be close to the current value of the top quark mass $m_t = (173.1 \pm 1.3)$ GeV. The advantage here is that, in contrast to the mass points discussed in this thesis, a better estimate on the expectation of $m_t$ can be given due to the availability of more mass points around the true value of the top quark mass. This also affects the study of the $p_{\perp}^{\text{jet}}$ cut and the $b$-tagging uncertainty since their dependancies can be investigated in detail around the true top quark mass value. Furthermore, the contribution of background can be suppressed by applying a more restrictive $p_{\perp}^{\text{jet}}$ cut in the jet selection, which has been kept low for this thesis to prevent a bias on the sample with the very low top quark mass of $m_t = 160$ GeV.

In general, technical aspects on the decay length method can also be improved in future studies. By fitting the decay length distribution rather than simply using its mean, the method is open to follow further approaches like the usage of templates similar to that of the template method. This ansatz provides the possibility to inclusively fit the fragmentation function, mean $B$-hadron mass and lifetime along with the top quark mass, which additionally helps in the suppresion of uncertainties from the $B$-hadron properties.

# Chapter 6

# Summary and Outlook

The top quark is the heaviest known fundamental particle up to date. Its mass $m_t$ plays an essential role in modern particle physics as a high precision knowledge on $m_t$ allows to perform consistency tests of the standard model and provides a constrain on the mass of the yet undiscovered Higgs boson. Since the discovery of the top quark in in 1995 at the Tevatron collider experiments CDF and DØ , a main focus was therefore to determine $m_t$ to a high precission. The current world avarage as of March 2009 presented by the Tevatron experiments is $m_t$ = (173.1 ± 1.3) GeV.

With the next generation proton-proton collider LHC a new era of particle physics will be reached. The LHC will be a top quark facility producing about eight million top quark pairs per year, thus making measurements of the top quark mass clearly dominated by systematic uncertainties. The ATLAS experiment is one of the major LHC experiments that will measure the top quark mass at high precision. The main systematic impact on $m_t$ at ATLAS will be due to the measurement of the energy of particle jets which plays an important role in most techniques for the determination of the top quark mass.

In this thesis the ATLAS application of an alternative method for the measurement of $m_t$ with complementary systematic uncertainties was discussed. This so-called decay length method infers the measured mean transverse decay length of $B$-hadrons $\langle L_{xy} \rangle$ in $t\bar{t}$ decays to the mass of their parent top quarks. Since the decay lengths are measured from the distances of primary and secondary vertices the method almost exclusively relies on tracking and is therefore independent from the measurement of jet energies.

This thesis discussed the inital application of the decay length method to ATLAS by investigating MonteCarlo simulations of a full ATLAS scenario. The general applicability of the method was demonstrated and an estimator for the dependance of $\langle L_{xy} \rangle$ on $m_t$ was found. For the combined $t\bar{t}$ signal plus background scenario this estimator is given by

$$\begin{aligned} \langle L_{xy}^{\text{reco}} \rangle (m_t) &= (2.31 \pm 0.45) \cdot 10^{-2} \frac{\text{mm}}{\text{GeV}} \cdot (m_t - 175 \text{ GeV}) \\ &+ (6.28 \pm 0.04)\,\text{mm}\,. \end{aligned} \tag{6.1}$$

The overall scale for the expected mean reconstructed transverse decay length is thus in the order of 6.3 mm, and the expected dependance on the top quark mass is about $2.31 \cdot 10^{-2}$ mm/GeV. This proves the mean transverse decay length to be a suitable observable, which is clearly resolvable even in a high track density environment like the ATLAS experiment.

The main systematic uncertainties of the decay length method were also estimated in this thesis. It has been found that the largest influence is due to the presence of initial and final state gluon radiation which changes the kinematics of the $t\bar{t}$ process and therefore the reconstructed decay length. The precision of the top quark mass due to this effect has been estimated to be about $\pm 5$ GeV on a top quark mass scale of $m_t = 175$ GeV. The investigation of initial and final state radiation is however still preliminary. Further improvements on the absolute radiation level may be investigated in future studies, where e.g. events from Drell-Yan process can be investigated since the momentum of Drell-Yan leptons is correlated to the level of initial state radiation.

The event selection has also been found to have a strong influence on the decay length method. Especially the $p_\perp$ selection of particle jets and the identification of $b$-jets play an important role since the kinematic of particle jets is directly related to both the tagging process as well as the reconstructed decay length associated to that jet. A first investigation on the complex relation between the jet $p_\perp$ cut, the $b$-tagging cut and $\langle L_{xy} \rangle$ has thus been performed to eliminate most effects. However, future MonteCarlo simulations with higher statistics and a larger variety of simulated top quark masses will greatly improve these results.

The influence of the jet energy measurement has been proven to be indeed negligible for the decay length method. This is an important result since the uncertainty estimates for other methods predict a precision of $\pm 3.5$ GeV on the top quark mass, making the decay length method complementary in its uncertainties.

Further uncertainty estimates include the properties of the investigated $B$-hadrons, such as the avarage $B$-hadron masses and lifetimes as well as the hadronization process which all affect the respective hadrons decay length; the uncertainties estimated here range in the region of $\pm 1$ GeV on the top quark mass. Further improvements on these uncertainties can be also obtained in future studies by inclusively fitting these parameters along with the top quark mass on the decay length distributions instead of using the mean. Investigations on this technique are ongoing and up to now yield promising results.

Based on the results obtained in this thesis it can be concluded that the decay length method is a promising alternative method to determine the top quark mass. The method has just started to grow out of its infancy with many investigations ongoing that aim on further methodical improvements as well as better estimates for ATLAS. The already started next generation MonteCarlo studies will provide the possibility to refine the uncertainty estimates on this method and help it contribute to high precision measurement of the top quark mass at the ATLAS experiment.

# Appendix A

# Technical appendix

The decay length method for top quark mass measurement is a relatively new method that has not been considered at ATLAS before. The observables needed for this method are basically the coordinates of the secondary vertices from particle jets which in general are accessible in ATLAS measurement data via tracking. Further variables include MonteCarlo truth information from the simulated ATLAS data that is used in the studies presented in this thesis. Examples of such variables are the true secondary vertices from jets that are asscociated to the reconstructed ones as well as the kinematic properties of the $b$-quarks and consecutive $B$-hadrons from the top quark decays and of the top quarks themselves.

To be able to investigate the decay length method these variables had to be integrated into the data files provided by the TopView framework that are used by ATLAS physics working groups for all top quark related analysis. An additional development was done on the level of the ROOT analysis framework the calculation of arithmetic mean values which is used widely in this thesis to calculate the mean transverse decay lengths that are the objects of this study.

The following sections provide technical information on the implementation of the respective software and the description of the corresponding algorithms that had been developed in the course of this thesis. A copy of the respective source codes is included separately on a CD that is attached to the print version of this thesis.

## A.1 Implementation of primary and secondary vertex information in TopView

The coordinates of primary and secondary vertices are essential parameters in the decay length method. To ensure the applicability of the method over the full term of the ATLAS experiment a persistent availability of these variables is required. Hence, the vertex variables were included as a default DPD content that is created by the official TopView framework. This section comments on technical details about how the vertex information is obtained from ATLAS AODs and how the persistency of this implementation is ensured.

### A.1.1 Structure and content of the AOD

As described in section 4.2.1 the AOD is the last data format in the chain of data processing at ATLAS that is common to all physics groups before the data is processed by physics specific tools (TopView in this case) that create DPD files

for the final physics analysis. Therefore, the AOD file contains the basic physics oberservables that are used by all physics groups as output by the detector. These oberservables are stored in the form of object classes which are called "containers". Each container represents an abstract physics object like eg. particle jets, electrons, muons or MCTruth information. The containers holds information on these objects, which can be simple common parameters like four-momentum vectors of particles and jets or more abstract object-specific information like e.g. tagging information of jets.

As several dedicated algorithms might exist to reconstruct a particular physics object, the container of such an object is capable to store the outputs of several algorithms in parallel, identically formatted branches. Each branch is simply identified by a key which allows to select the desired algorithm, thereby keeping the format of the output the same for each branch. The advantage of this approach is that the results of different alorithms which are applied to the same data can be analyzed at any time, allowing for comparison of reconstruction algorithms as well as for high flexibility in the access of the data. Examples of such objects are the secondary vertices of jets which can be reconstructed using either the BTagVrtSec algorithm or the JetFinder algorithm as described in section 4.3.2.

The overall concept of this structure bares several advantages. The reconstruction of raw data, i.e. calibration, tracking, jet finding etc. has been done on the ESD level and the AOD represents a choise of several different reconstruction outputs of the same data. In principle, the AOD resembles a repertory of the basic reconstruction results which can be applied modularily by the user who does not need to redo any reconstruction (although this is in principle possible). This ensures time saving processing since the user only needs to select the desired objects from the (pre-)reconstrcuted AOD, as well as a low proneness to errors since the reconstruction must not be redone.

### A.1.2 Implementation of vertex information

The TopView framework provides the possibility of a fully customized DPD creation. The customization capability also includes possible additions of new algorithms which can be seamlessly integrated into the framework by using C++ source codes that contain the algorithms combined with PYTHON scripts that are used to "steer" the framework and provide the interconnection of the algorithm source codes. The advantage of the usage of PYTHON is the possibility to define variables in the steering scripts which are commonly called "JobOptions" that can pass the variables to the C++ algorithms during runtime. Using this technique both container and container-key can be given to the algorithms via global variables, which makes the C++ coding tolerant to changes of the JobOptions scripts and, in the long term, to changes of the reconstruction since this simply reflects in a change of the container.

Both primary and secondary vertices can therefore be implemented by simple means. The primary vertices are stored in a separate container which can be accessed by a dedicated container-name and -key that is controlled by the JobOption file. The secondary vertices are part of the container that holds particle jets and are stored along with the tagging information of the jet. Again, these containers are accessed via keys defined in the JobOption file.

In the course of this thesis algorithms for both types of vertices have been implemented in the structure of the TopView framework. The secondary vertex information represents the most stable implementation as it is directly connected to the tagging information. It has successfully been implemented as standard in TopView and is therefore available in the official top quark working group's DPD files. The development of the primary vertex tool is completed to work on currently available ATLAS MonteCarlo data. However the robustness to the presence of multiple vertices was not tested since pile-up simulation is not included in top quark MonteCarlo data. The primary vertex tool is therefore not intended for a persistent integration in TopView at this point; however it has been used in the private production of DPDs as discussed in section 4.2.2.

## A.2 An event description for generated $t\bar{t}$ events

During the process of MonteCarlo event generation and detector simulation a lot of additional information regarding this process is stored alongside the mere output of simulated detector signals. This additional information contains a description of the generation and simulation of each each event in the sense of the true calculations and modellings that were performed. A usual reference to this data is therefore the term "truth" or "MCTruth" as it has been used widely in this thesis. In contrast, the pure simulation output which describes the physics process as seen by the detector is referred to as "reconstruction".

In particle physics collision experiments the aim of the reconstruction is to identify the hard collision process as good as possible. The full description of the hard process is therefore a crucial part of the truth information to provide a comparison with the reconstruction. In the context of $t\bar{t}$ physics this is of particular importance when identifying the top quark decay products to e.g. make correct assignments of reconstructed and MCTruth objects (so-called "reco-truth matching") or to determine the decay channel of the $t\bar{t}$ pair.

Concerning the decay length method the determination of MCTruth decay vertices of $B$-hadrons stemming from top quark decays is of great interest as they are used to obtain MCTruth decay lengths. In the course of this thesis a dedicated algorithm answering this purpose has been developed which is described in this section. The algorithm is designed to provide a full event description of generated $t\bar{t}$ events on the level of the hard process, with the main attention on the determination of the true secondary vertices and other parameters relevant for studies of the decay length method.

### A.2.1 The HepMC event record

HepMC is a C++ class for high energy physics event records [95]. It provides object oriented representations of particle physics objects using common notations like 'particle' and 'vertex', as well as methods to access these objects properties. Within the ATLAS AOD datafiles, the HepMC block is part of the so-called `McEventCollection` container which contains the Truth information as described previously. The applicability of HepMC covers a wide range of subprocesses within the generation, like hard collisions, parton showers, fragmentation and decays, of which each can be treated modularly. The structure of HepMC can be visualized by a graph representation similar to a physicists visualization of a collison event as shown in Figure A.1.

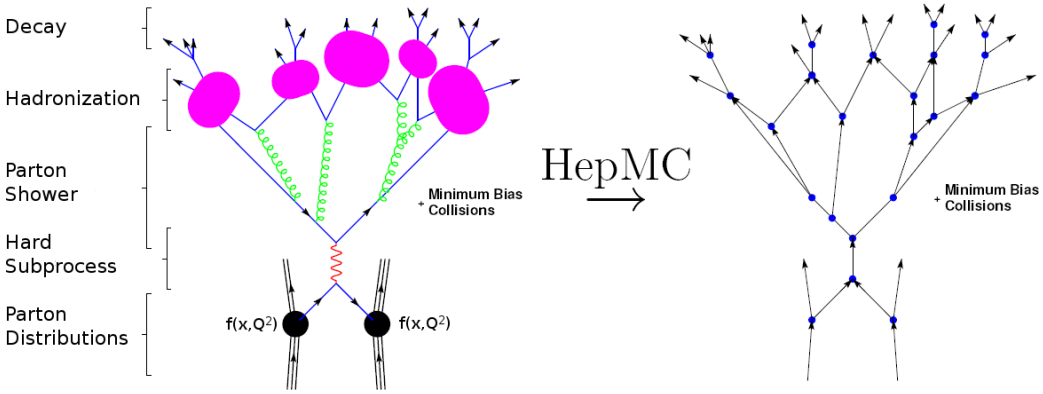


**Figure A.1:** Structure of the HepMC event record. The complexity of a particle collision event (left) is described by a simple graph structure similar to that of a Feynman diagram (right).

The basic building blocks of the event record are the three classes `HepMC::GenEvent` ("event"), `HepMC::GenVertex` ("vertex") and `HepMC::GenParticle` ("particle"). The `HepMC::GenEvent` class contains a basic event description consisting of pointers to all vertices and particles in the event, as well as additional information like event weights, process and event identification numbers and a documentation of all random states used during the generation. Within each event, the vertices and particles create the graph structure shown in Figure A.1, where the nodes represent the vertices and the lines represent the particles. From the physics point of view each vertex represents a change of physical states (i.e. particles) in the sense of fragmentation or decay, so that for a given particle or vertex at any point in the graph the full physical history and further development can be followed. For this purpose, both the event and vertex classes have iterators defined which allow fast access and the usage of loops at any point of the graph.

The vertex and particle classes themselves contain common particle physics properties. Like the event class both particles and vertices can be identified by an individual identification number (so-called "barcode") so that each instance of these objects within the event can be accessed directly. While the vertex properties are fully summarized as the space-time coordinates of the respective vertex, the properties of particles are more comprehensive. These properties the particles four-momentum, polarization, charge and several momentum related values like the particle mass and the angular directions $\eta$ and $\phi$. Furthermore, the particle type is well-defined by their identification number PDG_ID, which encodes information about the particle's spin, flavor content, and internal quantum numbers. The PDG_ID is officially assigned to a particle by the particle data group [96]; a list with the most important particles and numbers with respect to the decay length method is summarized in Table A.1.

**Table A.1:** An overview of relevant particle identification numbers (PDG_IDs) [96]. The respective antiparticles are noted as the negative value. Mesons and baryons are classified by their basic quark content using PDG_ID·100 (mesons) and PDG_ID·1000 (baryons), followed by a further identification number. The table shows the example of the $B$-hadron classification. The hadronization state "91" is an intermediate state that is used by HepMC to represent the transition of quarks into hadrons.

| Particle | PDG_ID | Particle | PDG_ID | Particle | PDG_ID |
|---|---|---|---|---|---|
| quarks | | leptons | | others | |
| $d$ | 1 | $e$ | 11 | $g$ | 21 |
| $u$ | 2 | $\nu_e$ | 12 | $\gamma$ | 22 |
| $s$ | 3 | $\mu$ | 13 | $W^+$ boson | 24 |
| $c$ | 4 | $\nu_\mu$ | 14 | $B$ mesons | 5xx |
| $b$ | 5 | $e$ | 15 | $B$ baryons | 5xxx |
| $t$ | 6 | $\nu_\tau$ | 16 | hadronization | 91 |

The most important feature of both particle and vertex objects is that both classes contain methods to navigate from vertices to particles and vice versa. For each individual instance of a vertex the barcodes of incommings and outgoing particles are stored, while for each instance of a particle the start- and ending vertex are known as shown in Figure A.2. This allows to navigate along a chain of particles and vertices within an event and thus providing the user with the possibility to obtain a full description of the event. An application of this feature is described in the following where the event description algorithm for generated ATLAS $t\bar{t}$ events is explained.


**Figure A.2:** Graphical representation of particles and vertices in the HepMC event record. Both object classes are interconnected through methods as indicated in the Figure, allowing for an easy navigation along particle lines via vertices.

### A.2.2 A HepMC based algorithm for the description of generated $t\bar{t}$ events

The algorithm for the description of $t\bar{t}$ events is devided in a main loop and two subroutines. The main loop is a nested loop running over three levels as seen in the algorithms flow chart shown in Figure A.3. The first level loop iterates the events found in the AOD files which is a trivial necessity in the treatment of event-by-event based datasets. For each event, the algorithm then starts searching the vertex of the hard collision where the $t\bar{t}$ pair is produced. This is done by an

iteration over all vertices found in the event, which in turn are checked for their outgoing particle lines whether they are identified as top quarks by their PDG_IDs. In case the outgoing particles are $t$ and $\bar{t}$ the respective vertex is marked as the $t\bar{t}$ production vertex. The iteration of vertices then continues until the last vertex is processed.

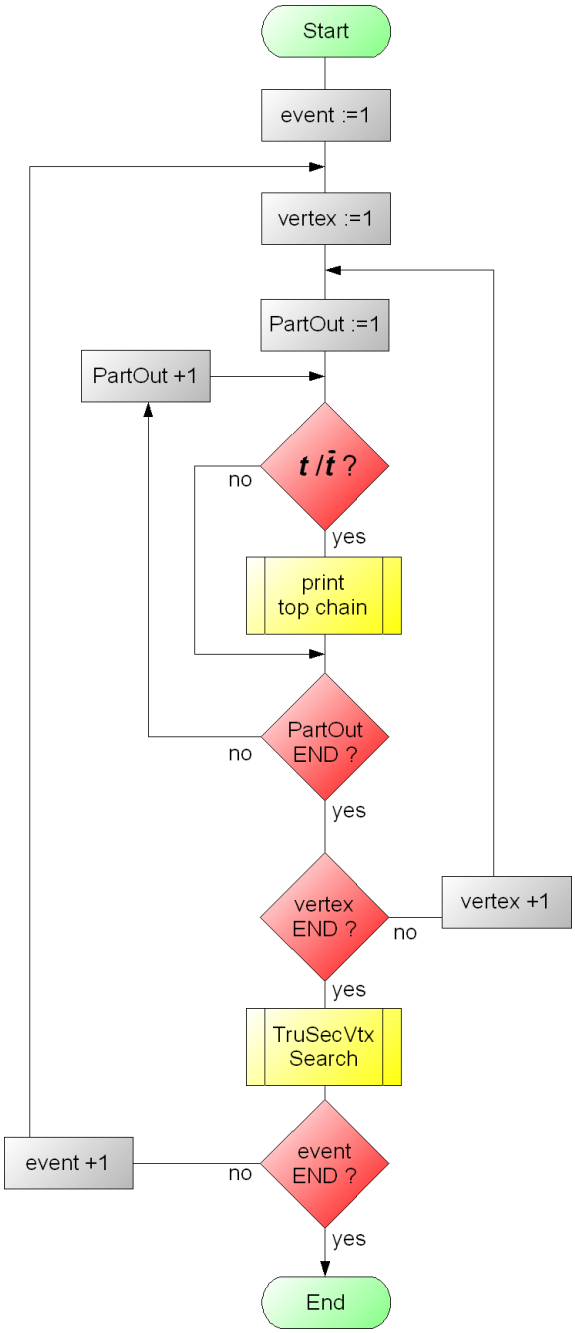


**Figure A.3:** Flow chart of the HepMC based algorithm to describe MonteCarlo generated $t\bar{t}$ events and obtain the respective MCTruth information. The flow charts of the two subroutines print_top_chain and TruSecVtx_Search are shown separately in Figures A.5 and A.6.

Directly after the $t\bar{t}$ decay vertex is found the `print_top_chain` subroutine is called which identifies the decay products of the respective top or antitop quark. This is simply done by checking the PDG_IDs of the particle lines that go out of the top or antitop quarks decay vertex, i.e. the `end_vertex` of the top quark line. This technique of "brachiating" along particles is then used further to identify the decay channel of the $W$-boson and the decay vertex of the $b$-quark from the respective top quark decay.

```
================================================================
# Starting event description                                   #
================================================================

 Iterating over Vertices
 =========================

-------------------------------------------------------------------------
  Vertex no. 1
  Coordinates: ( 26365.1816406250 , 33975.9414062500 , 4.837761e+07 ) nm
  BARCODE: -1
  Time: 0 Sec.


 Particle going into this vertex: PDG_ID: 21, Particle : gluon
  Particle going out of this vertex: PDG_ID: 21, Particle : gluon
  Particle going out of this vertex: PDG_ID: 21, Particle : gluon
  Particle going out of this vertex: PDG_ID: 0, Particle : unknown
  Particle going out of this vertex: PDG_ID: 6, Particle : top

    Found a top at vertex -1
    |
    +--> the top decays at vertex: -161
    |
    +--+-> the top decays into: PDG_ID: 24, Particle : W+
    |  +--+-> the W+ decays at vertex: -164
    |     +-> the W+ decays into: nu_e, PDG_ID: 12
    |     +-> the W+ decays into: e+, PDG_ID: -11
    |     +-> the W+ decays into: gamma, PDG_ID: 22
    |
    +--+-> the top decays into: PDG_ID: 5, Particle : bottom
       +--+-> hadronization of the bottom at vertex: -276
              position: ( 26365.18 , 33975.94 , 4.83e+07 ) nm,
              time: 5.50636e-23 sec,

  Particle going out of this vertex: PDG_ID: -6, Particle : ~top

   Found an anti_top at vertex -1
    |
    +--> the anti_top decays at vertex: -169
    |
    +--+-> the anti_top decays into: , PDG_ID: -24, Particle : W-
    |  +--+-> the W- decays at vertex: -172
    |     +-> the W- decays into: ~nu_tau, PDG_ID: -16
    |     +-> the W- decays into: tau-, PDG_ID: 15
    |
    +--+-> the anti_top decays into: , PDG_ID: -5, Particle : ~bottom
       +--+-> hadronization of the anti_bottom at vertex: -278
                 position: ( 26365.18 , 33975.94 , 4.83e+07 ) nm,
                 time: 1.5173e-21 sec,


 Particle going into this vertex: PDG_ID: 21, Particle : gluon

 (*)

================================================================
# Event description finished                                  #
================================================================
```

**Figure A.4:** Showcase output of the print_top_chain subroutine that identifies the decay products of top and antitop quark. The text output is used as a check during the processing of the AOD and provides an overview of the nature of the respective event. The flow chart of this subroutine is shown in Figure A.5.

For all particles participating in this decay chain the kinematic parameters are marked for storage in the final DPD, which is executed at the finalization of the event. The decay channel of the $W$-boson is identified by the PDG_IDs of the outgoing particles and is also stored in the DPD to be able to determine the decay channel of the $t\bar{t}$ decay as a whole. The decay vertex of the $b$-quark is stored transiently for later input into the `TruSecVtx_Search` subroutine which searches the true secondary vertex of the $B$-hadron stemming from this $b$-quark. A flow chart of the `print_top_chain` subroutine is shown in Figure A.5, and a showcase output of the first event of the $t\bar{t}$ signal sample 5200 is shown in Figure A.4 on page 120.

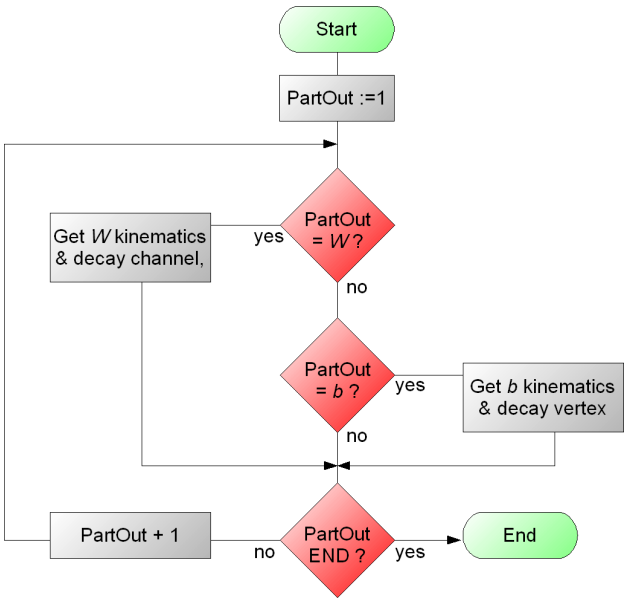


**Figure A.5:** The print_top_chain subroutine to obtain the daughter particles of the top or antitop quark. The routine is run twice per event and starts at each turn from the decay vertex of the respective top or antitop quark. The kinematic parameters of the $W$-boson and the $b$-quark are stored in the DPD. Additionally, the decay channel of the $W$-boson as well as the ending vertex of the $b$-quark are determined.

The `TruSecVtx_Search` is the second subroutine of the algorithm. It is called directly after the iteration of vertices ends and before the respective event is finalized and the next event starts. The subroutine is called twice to obtain the MCTruth secondary vertices of both the $b$- and $\bar{b}$-quark which are stored in the DPD along with the kinematics and PDG_IDs of the $b$-quarks and $B$-hadrons. The flow chart of the `TruSecVtx_Search` subroutine is shown in Figure A.6, and a showcase output demonstrating its functionality is shown in Figure A.7.

In each case the subroutine starts from the decay vertex of the $b$-quark ($\bar{b}$-quark) that has been stored during the run of the `print_top_chain` subroutine. From here on the previously described technique of brachiating along particle lines is used to determine the hadronic final state of the $b$-quark and its decay vertex. The brachiating is done such that each particle that is "$b$-type", i.e. either $b$-quark or $B$-hadron identified by their PDG_ID according to Table A.1, is followed to its decay vertex where the next $b$-type particle is identified by again checking the PDG_ID of the outgoing lines. This process is repeated until no more outgoing $b$-type particle is found; the respective decay vertex is then returned as the MCTruth secondary vertex.

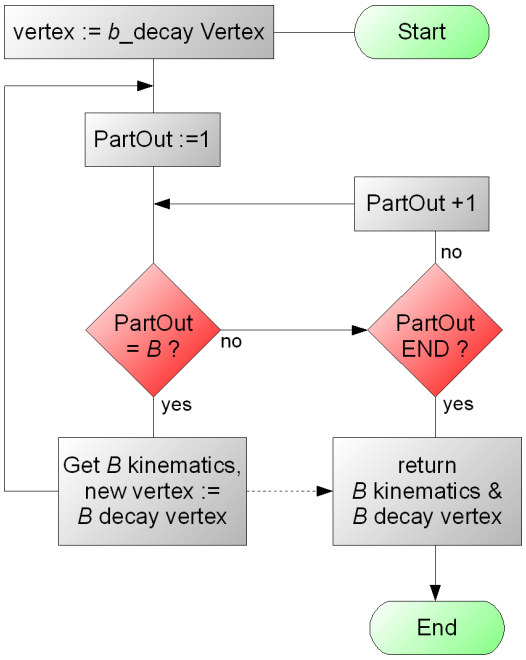


**Figure A.6:** The TruSecVtx_Search subroutine. This flow chart demonstrates the idea of iterative brachiating along the particle chain. For each particle the respective "child" particles are checked whether they are of the nature of $b$-quark or $B$-hadron (briefly called "$B$" in the flow chart). This particle is then followed until the final decay vertex is found, which is then returned to the main loop where it is stored in the DPD along with the parameters of the respective $B$-hadron.

Along the chain of $b$-type particles several special cases must be taken into account, like the presence of radiation or the intermediate state with PDG_ID "91" that occurs in HepMC at the level of hadronization. One has to keep in mind here that the graph structure of HepMC does not necessarily behave according to Feynman rules but instead represents a documentation of the physical process, which explaines some of the effects one might find in such a decay chain.

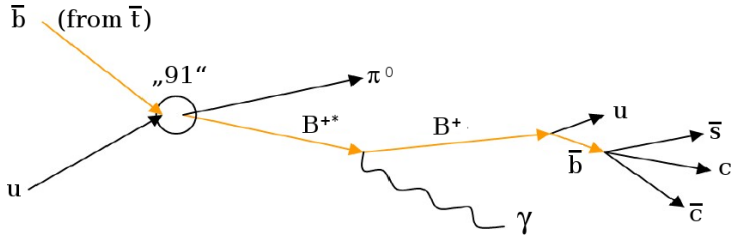


**Figure A.7:** Showcase output of the TruSecVtx_Search subroutine that finds the true secondary vertices of $B$-hadrons from top quark decays. This example shows the development of a $\bar{b}$-quark from the decay of the $\bar{t}$-quark and demonstrates many special cases that the subroutine has to take care of, like the intermediate hadronization state (PDG_ID = 91), electromagnetic radiation from the excited $B^{+*}$ and the way hadronic decays are treated by HepMC. The subroutines flow chart is shown in Figure A.6.

### A.2.3 Usecase and limitations of the algorithm

The previously described algorithm is designed to run exclusively on generated MonteCarlo data containing $t\bar{t}$ events. The investigation of single top quark samples is not supported up to this point and was also not intended in the origanl design of the algorithm. However, the algorithm has a strong power in the description of pure $t\bar{t}$ events and provides many MCTruth information of which especially the MCTruth secondary vertices and the flags describing the $t\bar{t}$ decay channel have been widely used within this thesis. Additional information like the kinematics of the $t/\bar{t}$- and $b/\bar{b}$-quarks and the $B$-hadrons was also used to obtain a generic overview of the events as well as for reco-truth matching.

A limitation of this algorithm is that the general modularity of the HepMC block generated data is handled differently by different generators. While the algorithm has been successfully applied to the MC@NLO $t\bar{t}$ signal samples, other generators have been found to treat the hard process, parton shower and hadronization steps independently and do not provide information about the connection of these steps. This makes it impossible to follow the particle lines though all stages as e.g. the documentary information about hadronization (i.e. the line with PDG_ID "91") is not available in the data. For now, the algorithm is therefore indicated only for private processing on MC@NLO data. However, the algorithm is easily extendable due to the simple structure of HepMC and future developments can improve the usability of this tool on other generators.

# Bibliography


[1] Joao Pequenao; Computer generated image of the whole ATLAS detector; Cern Document Server, CERN-GE-0803012, Keyword: ATLAS; Mar 2008.

[2] CERN. Geneva. LHC Experiments Committee ; LHCC; ATLAS: letter of intent for a general-purpose pp experiment at the large hadron collider at CERN; (CERN; Geneva; 1992); http://cdsweb.cern.ch/record/291061.

[3] The ATLAS Collaboration and G Aad et al; The ATLAS Experiment at the CERN Large Hadron Collider; Journal of Instrumentation **3** (2008) S08003; http://stacks.iop.org/1748-0221/3/S08003.

[4] CERN. Geneva. LHC Experiments Committee ; LHCC; ATLAS inner detector: Technical Design Report, 1; (CERN; Geneva; 1997); http://cdsweb.cern.ch/record/331063.

[5] Haywood, S and Rossi, L and Nickerson, R and Romaniouk, A; ATLAS inner detector: Technical Design Report, 2; (CERN; Geneva; 1997); http://cdsweb.cern.ch/record/331064.

[6] CERN. Geneva. LHC Experiments Committee ; LHCC; ATLAS tile calorimeter: Technical Design Report; (CERN; Geneva; 1996); http://cdsweb.cern.ch/record/331062.

[7] CERN. Geneva. LHC Experiments Committee ; LHCC; ATLAS liquid-argon calorimeter: Technical Design Report; (CERN; Geneva; 1996); http://cdsweb.cern.ch/record/331061.

[8] CERN. Geneva. LHC Experiments Committee ; LHCC; ATLAS level-1 trigger: Technical Design Report; (CERN; Geneva; 1998); http://cdsweb.cern.ch/record/381429.

[9] Jenni, Peter and Nessi, Marzio and Nordberg, Markus and Smith, Kenway; ATLAS high-level trigger, data-acquisition and controls: Technical Design Report; (CERN; Geneva; 2003); http://cdsweb.cern.ch/record/616089.

[10] Tevatron Electroweak Working Group and for the CDF Collaboration and The D0 Collaboration; Combination of CDF and D0 Results on the Mass of the Top Quark; 2009; arXiv.org:0903.2503.

[11] C. Amsler et al.; The Review of Particle Physics; Physics Letters **B667** (2008); http://pdg.lbl.gov/.

[12] V. E. Barnes et al.; Observation of a Hyperon with Strangeness Minus Three; Phys. Rev. Lett. **12** (1964) 204–207; http://dx.doi.org/10.1103/PhysRevLett.12.204.

[13] F. Halzen, A. D. Martin; QUARKS AND LEPTONS: An Introductory Course in Modern Particle Physics; (John Wiley & Sons, Inc.; 1984).

[14] J. W. Rohlf; MODERN PHYSICS from $\alpha$ to $Z^0$; (John Wiley & Sons, Inc.; 1994).

[15] G. Gabrielse et al.; New Determination of the Fine Structure Constant from the Electron $g$ Value and QED; Phys. Rev. Lett. **97** (2006) 030802.

[16] G. Gabrielse et al.; Erratum: New Determination of the Fine Structure Constant from the Electron $g$ Value and QED; Phys. Rev. Lett. **99** (2007) 039902.

[17] A. Sommerfeld; Atombau und Spektrallinien; (Friedr. Vieweg & Sohn Braunschweig Bd. I; $8^{\text{th}}$ edition; 1960).

[18] T. D. Lee, C. N. Yang; Question of Parity Conservation in Weak Interactions; Phys. Rev. **104** (1956) 254–258; http://dx.doi.org/10.1103/PhysRev.104.254.

[19] C. S. Wu et al.; Experimental Test of Parity Conservation in Beta Decay; Phys. Rev. **105** (1957) 1413 – 1415; http://dx.doi.org/10.1103/PhysRev.105.1413.

[20] Goldhaber, M. and Grodzins, L. and Sunyar, A. W.; Helicity of Neutrinos; Phys. Rev. **109** (1958) 1015–1017; http://dx.doi.org/10.1103/PhysRev.109.1015.

[21] Glashow, S. L. and Iliopoulos, J. and Maiani, L.; Weak Interactions with Lepton-Hadron Symmetry; Phys. Rev. **D2** (1970) 1285–1292; http://dx.doi.org/10.1103/PhysRevD.2.1285.

[22] Donald H. Perkins; Introduction to High Energy Physics; (Addison-Wesley Publishing Company, Inc.; third edition; 1987).

[23] Abe, F. et al.; Observation of Top Quark Production in $p\bar{p}$ Collisions with the Collider Detector at Fermilab; Phys. Rev. Lett. **74** (1995) 2626–2631; http://dx.doi.org/10.1103/PhysRevLett.74.2626.

[24] Abachi et al.; Observation of the Top Quark; Phys. Rev. Lett. **74** (1995) 2632–2637; http://dx.doi.org/10.1103/PhysRevLett.74.2632.

[25] Herb et al.; Observation of a Dimuon Resonance at 9.5 GeV in 400-GeV Proton-Nucleus Collisions; Phys. Rev. Lett. **39** (1977) 252–255; http://dx.doi.org/10.1103/PhysRevLett.39.252.

[26] Cooper-Sarkar, Amanda M. and Devenish, R. C. E. and De Roeck, A.; Structure functions of the nucleon and their interpretation; Int. J. Mod. Phys. **A13** (1998) 3385–3586; http://dx.doi.org/10.1142/S0217751X98001670.

[27] Pumplin, J. et al.; New generation of parton distributions with uncertainties from global QCD analysis; JHEP **07** (2002) 012; arXiv.org:hep-ph/0201195.

[28] Whalley, M. R. and Bourilkov, D. and Group, R. C.; The Les Houches Accord PDFs (LHAPDF) and Lhaglue; 2005; arXiv.org:hep-ph/0508110,http://projects.hepforge.org/lhapdf/.

[29] J. Pumplin et al.; New Generation of Parton Distributions with Uncertainties from Global QCD Analysis; JHEP0207 **012** (2002); arXiv.org:hep-ph/0201195.

[30] Quadt, Arnulf; Top quark physics at hadron colliders; Eur. Phys. J. **C48** (2006) 835–1000; http://dx.doi.org/10.1140/epjc/s2006-02631-6.

[31] Cacciari, M. and Frixione, S. and Mangano, M. L. and Nason, P. and Ridolfi, G.; The t anti-t cross-section at 1.8-TeV and 1.96-TeV: A study of the systematics due to parton densities and scale dependence; JHEP **04** (2004) 068; arXiv.org:hep-ph/0303085.

[32] Bonciani, Roberto and Catani, Stefano and Mangano, Michelangelo L. and Nason, Paolo; NLL resummation of the heavy-quark hadroproduction cross-section; Nucl. Phys. **B529** (1998) 424–450; http://dx.doi.org/10.1016/S0550-3213(98)00335-6.

[33] J. Haestier and S. Heinemeyer and D. Stockinger and G. Weiglein; Electroweak Precision Observables: Two-Loop Yukawa Corrections of Supersymmetric Particles; JHEP **0512** (2005) 027; arXiv.org:hep-ph/0508139.

[34] P. V. Landshoff; The total cross section at the LHC; ACTA PHYS.POLON.B **39** (2008) 2063; arXiv.org:0709.0395.

[35] The D0 Collaboration: V. M. Abazov; Observation of Single Top Quark Production; 2009; arXiv.org:0903.0850.

[36] The CDF Collaboration: T. Aaltonen; First Observation of Electroweak Single Top Quark Production; 2009; arXiv.org:0903.0885.

[37] John Campbell and Francesco Tramontano; Next-to-leading order corrections to Wt production and decay; Nuclear Physics B **726** (2005) 109; http://dx.doi.org/10.1016/j.nuclphysb.2005.08.015.

[38] Zack Sullivan; Understanding single-top-quark production and jets at hadron colliders; Physical Review D **70** (2004) 114012; arXiv.org:hep-ph/0408049.

[39] CDF Collaboration: T. Aaltonen; First Direct Bound on the Total Width of the Top Quark in ppbar Collisions at sqrt(s) = 1.96 TeV; Physical Review Letters **102** (2009) 042001; http://dx.doi.org/10.1103/PhysRevLett.102.042001.

[40] Chris Quigg; Top-ology; 1997; arXiv.org:hep-ph/9704332.

[41] F. Abe; Evidence for Top Quark Production in $\bar{p}p$ Collisions at $\sqrt{s} = 1.8$ TeV; Physical Review Letters **73** (1994) 225; 10.1103/PhysRevLett.73.225.

[42] S. Abachi; Search for High Mass Top Quark Production in p anti-p Collisions at S**(1/2) = 1.8 TeV; Physical Review Letters **74** (1995) 2422; 10.1103/PhysRevLett.74.2422.

[43] Sirlin, A.; Radiative corrections in the $SU(2)L \times U(1)$ theory: A simple renormalization framework; Phys. Rev. D **22** (1980) 971–981; http://dx.doi.org/10.1103/PhysRevD.22.971.

[44] The CERN, FERMILAB and SLAC collaborations; Precision Electroweak Measurements and Constraints on the Standard Model; 2008; Prepared from Contributions to the 2008 Summer Conferences.; arXiv.org:0811.4682.

[45] G. Abbiendi; Search for the Standard Model Higgs Boson at LEP; Physics Letters B **565** (2003) 61; http://dx.doi.org/10.1016/S0370-2693(03)00614-2.

[46] Tevatron New Phenomena and Higgs Working group and for the CDF Collaboration and DZero Collaboration; Combined CDF and DZero Upper Limits on Standard Model Higgs-Boson Production with up to 4.2 fb-1 of Data; 2009; arXiv.org:0903.4001.

[47] S. Heinemeyer and W. Hollik and D. Stockinger and A. M. Weber and G. Weiglein; Precise Prediction for M_W in the MSSM; JHEP **0608** (2006) 052; arXiv.org:hep-ph/0604147.

[48] S. Heinemeyer and W. Hollik and G. Weiglein; Electroweak Precision Observables in the Minimal Supersymmetric Standard Model; Physics Reports **425** (2006) 265; arXiv.org:hep-ph/0412214.

[49] ATLAS Collaboration; Expected Performance of the ATLAS Experiment: Detector, Trigger and Physics – Top Quark – Top quark mass measurement with ATLAS; (CERN; Geneva; 2008); http://cdsweb.cern.ch/record/1159602.

[50] CDF Collaboration; Top Quark Mass Measurement Using the Template Method in the Lepton + Jets Channel at CDF II; Physical Review D **73** (2006) 032003; http://dx.doi.org/10.1103/PhysRevD.73.032003.

[51] D0 Collaboration; A Precision Measurement of the Mass of the Top Quark; Nature **429** (2004) 638; http://dx.doi.org/10.1038/nature02589.

[52] CDF Collaboration; Measurement of the Top Quark Mass with the Dynamical Likelihood Method using Lepton plus Jets Events with b-tags in ppbar Collisions at s**(1/2) = 1.96 TeV; Physical Review D **73** (2006) 092002; http://dx.doi.org/10.1103/PhysRevD.73.092002.

[53] D0 Collaboration and V. Abazov; Experimental discrimination between charge 2e/3 top quark and charge 4e/3 exotic quark production scenarios; Physical Review Letters **98** (2007) 041801; http://dx.doi.org/10.1103/PhysRevLett.98.041801.

[54] W. Bernreuther and A. Brandenburg and Z. G. Si and P. Uwer; Top quark pair production and decay at hadron colliders; Nuclear Physics B **690** (2004) 81; http://dx.doi.org/10.1016/j.nuclphysb.2004.04.019.

[55] ATLAS Collaboration; Expected Performance of the ATLAS Experiment: Detector, Trigger and Physics – Top Quark – Top quark properties; (CERN; Geneva; 2008); http://cdsweb.cern.ch/record/1159602.

[56] ATLAS Collaboration; Expected Performance of the ATLAS Experiment: Detector, Trigger and Physics – Introduction; (CERN; Geneva; 2008); http://cdsweb.cern.ch/record/1159564.

[57] ATLAS Collaboration; Expected Performance of the ATLAS Experiment: Detector, Trigger and Physics; (CERN; Geneva; 2008); http://cdsweb.cern.ch/record/1125884.

[58] S. Frixione and B. R. Webber; Matching NLO QCD computations and parton shower simulations; JHEP **0206** (2002) 029; arXiv.org:hep-ph/0204244.

[59] S. Frixione and P. Nason and B. R. Webber; Matching NLO QCD and parton showers in heavy flavour production; JHEP **0308** (2003) 007; arXiv.org:hep-ph/0305252.

[60] Stefano Frixione and Bryan R. Webber; The MC@NLO 3.1 Event Generator; 2005; arXiv.org:hep-ph/0506182.

[61] G. Corcella and I. G. Knowles and G. Marchesini and S. Moretti and K. Odagiri and P. Richardson and M. H. Seymour and B. R. Webber; HERWIG 6.5: an event generator for Hadron Emission Reactions With Interfering Gluons (including supersymmetric processes); JHEP0101 **010** (2001); arXiv.org:hep-ph/0011363.

[62] G. Corcella and IG Knowles and G. Marchesini and S. Moretti and K. Odagiri and P. Richardson and MH Seymour and BR Webber; HERWIG 6.5 Release Note; 2002; arXiv.org:hep-ph/0210213.

[63] J. M. Butterworth and J. R. Forshaw and M. H. Seymour; Multiparton Interactions in Photoproduction at HERA; Zeitschrift für Physik C **72** (1996) 637; http://dx.doi.org/10.1007/s002880050286.

[64] Borut Paul Kersevan and Elzbieta Richter-Was; The Monte Carlo Event Generator AcerMC 2.0 with Interfaces to PYTHIA 6.2 and HERWIG 6.5; 2004; arXiv.org:hep-ph/0405247.

[65] Torbjorn Sjostrand and Stephen Mrenna and Peter Skands; PYTHIA 6.4 Physics and Manual; JHEP0605 **026** (2006); arXiv.org:hep-ph/0603175.

[66] Torbjorn Sjostrand and Stephen Mrenna and Peter Skands; A Brief Introduction to PYTHIA 8.1; 2007; http://dx.doi.org/10.1016/j.cpc.2008.01.036.

[67] B. P. Kersevan I. Hinchliffe; A Consistent Prescription for the Production Involving Massive Quarks in Hadron Collisions; JHEP0609 **033** (2006); arXiv.org:hep-ph/0603068.

[68] M. L. Mangano and M. Moretti and F. Piccinini and R. Pittau and A. D. Polosa; ALPGEN, a generator for hard multiparton processes in hadronic collisions; JHEP **0307** (2003) 001; arXiv.org:hep-ph/0206293.

[69] J. Alwall and S. Hoeche and F. Krauss and N. Lavesson and L. Lonnblad and F. Maltoni and M. L. Mangano and M. Moretti and C. G. Papadopoulos and F. Piccinini and S. Schumann and M. Treccani and J. Winter and M. Worek; Comparative study of various algorithms for the merging of parton showers

and matrix elements in hadronic collisions; European Physical Journal C **53** (2008) 473; http://dx.doi.org/10.1140/epjc/s10052-007-0490-5.

[70] CERN. Geneva. LHC Experiments Committee ; LHCC; ATLAS computing: Technical Design Report; (CERN; Geneva; 2005); http://cdsweb.cern.ch/record/837738.

[71] Shibata, A; TopView - ATLAS top physics analysis package; Internal Report ATL-SOFT-PUB-2007-002. ATL-COM-SOFT-2007-006. CERN-ATL-COM-SOFT-2007-006; CERN; Geneva; May 2007.

[72] Gerald C. Blazey et al.; Run II Jet Physics: Proceedings of the Run II QCD and Weak Boson Physics Workshop; 2000; arXiv.org:hep-ex/0005012.

[73] Bouhova-Thacker et al.; Vertex Reconstruction in the ATLAS Experiment at the LHC; Internal Report ATL-INDET-PUB-2009-001. ATL-COM-INDET-2009-011; CERN; Geneva; May 2009; Note was a proceeding for IEEE/NSS Dresden 2008 and is now intended for possible publication in TNS..

[74] Rochester, G. D. and Butler, C. C.; Evidence for the existence of new unstable elementary particles; Nature **160** (1947) 855–857; http://dx.doi.org/10.1038/160855a0.

[75] Fowler, W. B. and Shutt, R. P. and Thorndike, A. M. and Whittemore, W. L.; Observation of $V$ Particles Produced at the Cosmotron; Phys. Rev. **90** (1953) 1126–1127; http://dx.doi.org/10.1103/PhysRev.90.1126.

[76] Hopper, V. D. and Biswas, S.; Evidence Concerning the Existence of the New Unstable Elementary Neutral Particle; Phys. Rev. **80** (1950) 1099–1100; http://dx.doi.org/10.1103/PhysRev.80.1099.

[77] G. Piacquadio and K. Prokofiev and A. Wildauer; Primary vertex reconstruction in the ATLAS experiment at LHC; Journal of Physics: Conference Series **119** (2008) 032033 (8pp); http://dx.doi.org/10.1088/1742-6596/119/3/032033.

[78] P. Billoir and S. Qian; Simultaneous pattern recognition and track fitting by the Kalman filtering method; Nuclear Instruments and Methods in Physics Research Section A: Accelerators, Spectrometers, Detectors and Associated Equipment **294** (1990) 219 – 228; http://dx.doi.org/10.1016/0168-9002(90)91835-Y.

[79] ATLAS Collaboration; Expected Performance of the ATLAS Experiment: Detector, Trigger and Physics – $b$-Tagging – Vertex reconstruction for $b$-Tagging; (CERN; Geneva; 2008); http://cdsweb.cern.ch/record/1159581.

[80] ATLAS Collaboration; Expected Performance of the ATLAS Experiment: Detector, Trigger and Physics – Electrons and Photons – Reconstruction and Identification of Electrons; (CERN; Geneva; 2008); http://cdsweb.cern.ch/record/1159567.

[81] ATLAS Collaboration; Expected Performance of the ATLAS Experiment: Detector, Trigger and Physics – Muons – Muon Reconstruction and Identification: Studies with Simulated Monte Carlo Samples; (CERN; Geneva; 2008); http://cdsweb.cern.ch/record/1159572.

[82] ATLAS Collaboration; Expected Performance of the ATLAS Experiment: Detector, Trigger and Physics – $b$-Tagging – Performance of the $b$-tagging algorithms; (CERN; Geneva; 2008); http://cdsweb.cern.ch/record/1159581.

[83] Hill, C. S. and Incandela, J. R. and Lamb, J. M.; Method for measurement of the top quark mass using the mean decay length of $b$ hadrons in $t\bar{t}$ events; Phys. Rev. D **71** (2005) 054029; http://dx.doi.org/10.1103/PhysRevD.71.054029.

[84] Christian Jung; Entwicklung und Validierung einer Parametrisierung der Zerfallslaengenverteilungen von $B$-Hadronen aus top-Quark Zerfaellen – to be published; 2010.

[85] E. Barberio et al.; Averages of b-hadron and c-hadron Properties at the End of 2007; 2008; arXiv.org:0808.1297.

[86] ALEPH, CDF, DELPHI, L3, OPAL, SLD collaborations; Combined results on b-hadron production rates and decay properties; 2001; arXiv.org:hep-ex/0112028v1.

[87] V. G. Kartvelishvili and A. K. Likhoded and V. A. Petrov; On the fragmentation functions of heavy quarks into hadrons; Physics Letters B **78** (1978) 615 – 617; http://dx.doi.org/10.1016/0370-2693(78)90653-6.

[88] M. G. Bowler and P. N. Burrows and D. H. Saxon; Baryon fragmentation functions and diquark structure; Physics Letters B **221** (1989) 415 – 421; http://dx.doi.org/10.1016/0370-2693(89)91736-X.

[89] Bo Andersson; The Lund model; Nuclear Physics A **461** (1987) 513 – 520; http://dx.doi.org/10.1016/0375-9474(87)90510-0.

[90] Peterson, C. and Schlatter, D. and Schmitt, I. and Zerwas, P. M.; Scaling violations in inclusive $e + e-$ annihilation spectra; Phys. Rev. D **27** (1983) 105–111; http://dx.doi.org/10.1103/PhysRevD.27.105.

[91] The OPAL collaboration; Inclusive Analysis of the b Quark Fragmentation Function in Z Decays at LEP; European Physical Journal C **29** (2003) 463; http://dx.doi.org/10.1140/epjc/s2003-01229-x.

[92] Stefan Gieseke; Uncertainties of Sudakov form factors; JHEP0501 **058** (2005); arXiv.org:hep-ph/0412342.

[93] Cristinziani, M and Loginov, A and Adelman, J and Allwood-Spiers, S and Auerbach, B and Cranmer, K and Gellerstedt, K and Guo, B and Kaplan, B and Lockwitz, S and Poghosyan, T and Porter, R and Ragajopalan, S and Searcy, J and Sinervo, P and SjÃ¶lin, J and Shibata, A and Ta, D B and Taffard, A and Tipton, P and Vlasov, N and Whiteson, D and Wraight, K; Sensitivity of the top dilepton cross-section measurement at sqrts = 10 TeV; 2009; http://cdsweb.cern.ch/record/1189930.

[94] CERN. Geneva. LHC Experiments Committee ; LHCC; ATLAS detector and physics performance: Technical Design Report, 2; (CERN; Geneva; 1999); http://cdsweb.cern.ch/record/391177.

[95] Dobbs, M and Hansen, J B; The HepMC C++ Monte Carlo Event Record for High Energy Physics; 2000; http://cdsweb.cern.ch/record/684090.

[96] The particle data group PDG (C. Amsler et al.); Monte Carlo particle numbering scheme; Physical Review D **66** (2002) 010001+; http://pdg.lbl.gov/mc_particle_id_contents.html.

# Acknowledgements

During the past years working on this thesis I received great support of many people I would like to express my gratitude to. The support ranged from small but effective hints up to long and fruitful discussions and applied to all circumstances, mentioning physics questions as well as private affairs.

At first I would like to thank my supervisor Dr. Reiner Klingenberg and the head of the department of experimental physics IV at the TU Dortmund, Prof. Dr. Claus Gössling, for their supervising and general supporting role and for the opportunity to work at the ATLAS experiment. I enjoyed working on both the pixel detector and top quark physics which gave me the opportunity to gain a deeper understanding of the hardware, software and physics matters of the ATLAS experiment as well as a lot concerns along the way. Especially I would like to thank Reiner Klingenberg for the academic supervision of this thesis and the frequent discussions on the topic.

Next I would like to thank the top quark physics working groups both as part of the ATLAS community as well as the local group at the department of experimental physics IV in Dortmund.

Within the ATLAS group I would like to thank Anne-Isabelle Etienvre and Dominique Pallin for their leading role in the top quark mass working group, where I received a lot of support. A very special thanks goes to Akira Shibata for the support with TopView and related concerns. Further I would like to thank Markus Cristinziani for the collaboration in both pixel detector and top quark physics related concerns, Birte Domnik for discussions on the decay length method and Richard Hawkings for helpful comments.

From the local group in Dortmund I would like to thank Ingo Reisinger, Moritz Bunse and Georg Troska for physical and technical comments on the decay length method during the long period of Athena developments, code-hacking and CSC discussions. This applies also to Florian Hirsch who was mostly remote. In the beginning phase there was also support from Daniel Dobos who did Athena tutorials and provided us with the `JointDortmundTTbarAnalysis` framework, which was a good place to start from. At last I want to thank our newest colleagues Alexandra Dorschu, Christian Jung and Hendrik Esch for teaming up with us. Especially I would like to thank Christian Jung who will keep the decay length method alive.

Furthermore I would like to thank the people from the department EIV for the good working atmosphere. A special thanks goes to Oliver Schulz and Markus Alex for technical support regarding computational stuff and Theo Villet, Daniel Münstermann and Silke Rajek for their personal support.

My gratitudes go to my family for personal relations. I would like to mention my mother Gabriele Walbersloh, my father Burkhard Walbersloh, my sister Kerstin Walbersloh and her son, Niklas Niedenführ. There are too many thinks to list here that I have to be grateful for, so thank you all. In addendum, I would like to thank Maximilian for sharing good times. Goodbye!

Very personal gratitudes go to several people that I would like to mention now. At first, I would like to thank Helmut Linder, Ellen Lindner née Nadler and Steffen Rupp for being good friends. Especially I would like to thank Helmut Lindner for lots of heated but fruitful discussions and for his trust. Many thanks for the opportunity to be a witness to your marriage.

A very special thanks also goes to Jörg Köntopp, Simone Leineweber, Andreas Rheindorf, Michael Köntopp, Saskia Müller, Thorsten Baaske and again my sister Kerstin Walbersloh for reuniting. You are the best!

From the dancing community I would like to thank Valentina Breitfelder, Valerie Schkolver, Rubina Kazi and Thomas Held for their good company and support during lessons and tournaments. A special thanks goes to Olga Chekenda and Christina Hopfgarten for their role as the female part in the AHS lessons where we dealt with numerous students and twice as much left foots.

Further I would like to thank the Lietz, Schmitt, Gotal and Kämmerling families, Daniel Münstermann and Silke Rajek for their company and support.

My last words go to my partner Daniela Lietz, who is a great companion and my ease of mind, who brings me to rest. Thank you for your patience, your love and your smile, and for sticking though some really hard times with me. I love you!